Non-collinear magnetic ground states observed in iron nanostructures on iridium surfaces

Dissertation
zur Erlangung das Doktorgrades
am Departement Physik
der Universität Hamburg

vorgelegt von
Dipl.-Phys. Matthias Menzel
aus Berlin

Hamburg 2011

Universität Hamburg
DER FORSCHUNG | DER LEHRE | DER BILDUNG

Gutachter der Dissertation:
Prof. Dr. R. Wiesendanger
Prof. Dr. S. Heinze
Prof. Dr. M. Affronte

Gutachter der Disputation:
Prof. Dr. R. Wiesendanger
Prof. Dr. K. Nielsch

Datum der Disputation:
26.09.2011

Vorsitzender des Prüfungsausschusses:
Prof. Dr. M. A. Rübhausen

Vorsitzender des Promotionsausschusses:
Prof. Dr. P. Hauschildt

Dekan der MIN-Fakultät:
Prof. Dr. H. Graener

Abstract

In this thesis, investigations of iron (Fe) nanostructures on the reconstructed (001) and on the (111) surface of an iridium (Ir) single crystal are presented. Both sample systems exhibit complex, non-collinear magnetic ground states which are studied by means of spin-polarized scanning tunneling microscopy (SP-STM).

Fe atoms deposited on the (5×1)-reconstructed Ir(001) surface grow in the trenches of the reconstruction, thereby forming chains with a width of only two atoms. High-resolution scanning tunneling microscopy (STM) measurements allow the determination of the favorable adsorption sites of the Fe atoms, and the electronic properties of the Fe chains are investigated using scanning tunneling spectroscopy (STS). SP-STM measurements in an external magnetic field reveal a modulation with a periodicity of three atomic distances along the chain axes. This modulation is visible in constant current images as well as in maps of the differential conductance and can be attributed to a spin spiral ground state. Without an external magnetic field, the spin spiral fluctuates as a macrospin at the measurement temperature ($T = 8\,\mathrm{K}$) due to thermal excitations, which leads to a vanishing contrast in SP-STM measurements. Density functional theory (DFT) calculations reveal a combination of extremely weak Heisenberg exchange and the antisymmetric Dzyaloshinskii-Moriya (DM) interaction as the microscopic origin of this non-collinear ground state.

The first atomic layer of Fe on the Ir(111) surface predominately continues the face-centered cubic (fcc) structure of the Ir single crystal which leads to a hexagonal arrangement of the Fe atoms. In SP-STM measurements, the Fe layer exhibits an almost square magnetic superstructure with a unit cell consisting of approx. 15 atoms. Measurements of four different magnetization components are superimposed and reveal a lattice of skyrmions as the ground state of this sample system. The magnetic structure can be detected in spin-averaged STM measurements due to its non-collinearity, which gives rise to the tunneling anisotropic magnetoresistance (TAMR). Atomically resolved STM images with simultaneously acquired TAMR-contrast show that the skyrmion lattice is incommensurate to the atomic lattice. DFT calculations reveal that the Heisenberg exchange in this sample system is extremely weak, similar to the Fe chains on the Ir(001) surface. Therefore, the DM interaction and the often neglected four-spin interaction play crucial roles, and drive the Fe layer into the skyrmion lattice ground state.

Inhaltsangabe

In der vorliegenden Arbeit werden Untersuchungen an Eisen (Fe) Nanostrukturen auf zwei unterschiedlichen Iridium (Ir) Oberflächen vorgestellt. Über Messungen mittels der spin-polarisierten Rastertunnelmikroskopie (SP-STM) wurde in beiden Probensystemen ein komplexer, nicht-kollinearer magnetischer Grundzustand gefunden.

Fe-Atome, die bei Raumtemperatur auf die (5×1)-rekonstruierte Ir(001) Oberfläche aufgebracht werden, ordnen sich in den Gräben der Rekonstruktion zu Ketten mit einer Breite von lediglich zwei Atomen an. Die Adsorptionsplätze der Fe-Atome können durch die hohe Ortsauflösung der Rastertunnelmikroskopie (STM) bestimmt werden, und die elektronischen Eigenschaften werden mittels Rastertunnelspektroskopie (STS) untersucht. In SP-STM Messungen in einem externen Magnetfeld wurden auf allen Ketten eine Modulation mit einer Periodizität von drei atomaren Abständen entlang der Kettenachse festgestellt. Diese Modulation ist sowohl in Konstantstrom-Bildern als auch in Karten der differentiellen Leitfähigkeit zu sehen, und wird durch eine Spinspirale hervorgerufen. Bei der Messtemperatur ($T = 8\,\mathrm{K}$) kann ohne ein externes Magnetfeld kein magnetisches Signal gemessen werden, da die Spinspirale wie ein Makrospin thermisch fluktuiert. Rechnungen mittels Dichtefunktionaltheorie (DFT) zeigen, dass dieser nicht-kollineare Grundzustand durch das Zusammenspiel der antisymmetrischen Dzyaloshinskii-Moriya (DM) Wechselwirkung und einer extrem schwachen Heisenberg-Austauschwechselwirkung hervorgerufen wird.

Die erste atomare Lage Fe auf der Ir(111) Oberfläche wächst pseudomorph und setzt die fcc Kristallstruktur fort, was zu einer hexagonalen Anordnung der Fe-Atome führt. In SP-STM Messungen zeigt diese Fe-Lage eine fast quadratische magnetische Überstruktur, deren Einheitszelle aus ungefähr 15 Atomen besteht. Messungen von vier verschiedenen Komponenten der Probenmagnetisierung können zu der kompletten Magnetisierungsdichte überlagert werden, welche durch ein Gitter von magnetischen Skyrmionen hervorgerufen wird. Diese magnetische Struktur kann auch in spingemittelten STM-Messungen gemessen werden, da ihre Nichtkollinearität den anisotropen magnetischen Tunnelwiderstand (TAMR) bedingt. STM-Bilder mit sowohl atomarer Auflösung als auch TAMR-Kontrast zeigen, dass das Skyrmionengitter inkomensurabel zu dem atomaren Gitter ist. DFT-Rechnungen ergeben auch für dieses Probensystem, ähnlich wie bei den Fe Ketten auf der Ir(001) Oberfläche, eine sehr schwache Heisenberg-Austauschwechselwirkung. Das führt dazu, dass die DM-Wechselwirkung und die oft vernachlässigte Vierspin-Wechselwirkung tragende Rollen spielen und für das Skyrmionengitter als den magnetischen Grundzustand verantwortlich sind.

Contents

1. Introduction **1**

2. Magnetic interactions **3**
2.1. Heisenberg exchange interaction . . . 3
2.2. Spin-orbit interaction . . . 6
2.2.1. Magnetic anisotropy energy . . . 6
2.2.2. Dzyaloshinskii-Moriya interaction . . . 8
2.3. Higher order exchange interactions . . . 9

3. Scanning tunneling microscopy **11**
3.1. The tunnel effect in one dimension . . . 11
3.2. Experimental realization . . . 12
3.3. Topography . . . 15
3.3.1. Time-dependent perturbation theory . . . 15
3.3.2. Tersoff-Hamann model . . . 16
3.3.3. Chen's expansion of the Tersoff-Hamann model . . . 18
3.3.4. Effects of the electronic structure of the sample . . . 18
3.4. Scanning Tunneling Spectroscopy . . . 21
3.5. Spin-polarized scanning tunneling microscopy . . . 22

4. Instrumental setup and preparation **25**
4.1. UHV system . . . 25
4.2. Scanning tunneling microscopes . . . 26
4.2.1. Room temperature scanning tunneling microscope . . . 26
4.2.2. Low temperature scanning tunneling microscope . . . 27
4.3. Preparation of tips for SP-STM measurements . . . 28
4.4. Sample preparation . . . 29
4.4.1. Preparation of Fe chains on (5×1)-reconstructed Ir(001) . . . 29
4.4.2. Ir(001) surface and its reconstruction . . . 31
4.4.3. Growth of Fe on reconstructed Ir(001) . . . 33
4.4.4. Electronic properties of the Fe chains . . . 35
4.4.5. Sample quality and effects of contaminations . . . 37

5. Magnetism of iron chains on iridium(001) 43
5.1. Magnetism in atomic chains . . . 43
5.1.1. What is special about one-dimensional magnetism? . . . 43
5.1.2. Magnetic chains on surfaces . . . 44
5.2. SP-STM measurements on Fe chains on (5×1)-reconstructed Ir(001) . . . 45
5.3. Physical origin of the spin spiral in the Fe chains . . . 51
5.3.1. DFT calculations . . . 51
5.3.2. MC simulations . . . 53
5.4. Simulations of magnetization dynamics in the Fe chains . . . 56
5.4.1. The OOMMF simulation program and its extensions . . . 56
5.4.2. Comparison between MC and OOMMF simulations . . . 58
5.4.3. Thermal fluctuations . . . 60
5.4.4. Temperature dependence of the order parameter . . . 63
5.4.5. Outlook I: Chains of different lengths . . . 64
5.4.6. Outlook II: Information transport through the chains . . . 66
5.5. Summary . . . 67

6. Magnetism of the iron monolayer on iridium(111) 69
6.1. Skyrmions . . . 69
6.1.1. What is a skyrmion? . . . 69
6.1.2. Skyrmions in magnetism . . . 70
6.2. Skyrmion lattice in the Fe ML on Ir(111) . . . 72
6.2.1. Previous investigations of Fe/Ir(111) . . . 72
6.2.2. Reexamination of the Fe ML on Ir(111) using SP-STM . . . 75
6.2.3. Proof of incommensurability employing TAMR . . . 84
6.2.4. Physical origin of the skyrmion lattice . . . 88
6.3. Summary . . . 93

7. Summary and outlook 95

Bibliography 97

Publications 111

A. Source code for interactions in OOMMF 115

B. Ground state energies for different chain lengths 149

Abbreviations

AFM	antiferromagnetic
bcc	body-centered cubic
DFT	density functional theory
DM	Dzyaloshinskii-Moriya
fcc	face-centered cubic
FM	ferromagnetic
hcp	hexagonal closed-packed
LDOS	local density of states
MAE	magnetic anisotropy energy
MC	Monte-Carlo
ML	monolayer
OOMMF	object oriented micromagnetic framework
RT	room temperature
SOI	spin-orbit interaction
SP-STM	spin-polarized scanning tunneling microscopy
STM	scanning tunneling microscopy, scanning tunneling microscope
STS	scanning tunneling spectroscopy
TAMR	tunneling anisotropic magnetoresistance
UHV	ultra-high vacuum

Constants

elementary charge	$\mathrm{e} = 1.602 \cdot 10^{-19}\,\mathrm{C}$	
reduced Planck constant	$\hbar = 1.054 \cdot 10^{-34}\,\mathrm{J \cdot s}$	$= 6.582 \cdot 10^{-16}\,\mathrm{eV \cdot s}$
Bohr magneton	$\mu_\mathrm{B} = 9.274 \cdot 10^{-24}\,\mathrm{J \cdot T^{-1}}$	$= 5.788 \cdot 10^{-5}\,\mathrm{eV \cdot T^{-1}}$
speed of light	$c = 299792458\,\mathrm{m \cdot s^{-1}}$	
electron mass	$m_\mathrm{e} = 9.109 \cdot 10^{-31}\,\mathrm{kg}$	

1. Introduction

Magnetism and related phenomena have been known about for more than 2500 years and were first mentioned around the same time by the Greeks and the Chinese. The origin of the word "magnetism" is debated, with some sources stating that it comes from the region Magnesia in Greece, where magnetite, a magnetic iron ore, was mined. Other sources claim that *magnetism* is named after its discoverer the Greek shepherd Magnes, who found that the nails of his shoes were attracted by a stone. After its discovery, it took around 1500 years until the first documented application of magnetic material: A compass with a needle made of lodestone which was used by the Chinese for navigation in the 11th century.

The investigation of magnetic phenomena did not begin until the 16th century with the "father of magnetism" William Gilbert, who discovered that the Earth itself behaves like a huge magnet. In the following centuries, the investigation and theoretical description of macroscopic magnetic phenomena made fast advances. In the 1780s, Charles Augustin de Coulomb formulated his inverse-square law, which describes the distance dependence of a magnetic field. In 1802, Gian Domenico Romagnosi found the connection between electricity and magnetism[1], and in 1861/1862 James Clerk Maxwell published his famous equations, which describe electric charges and currents as the sources for electric and magnetic fields. Despite these advances in the description of magnetic fields, only two magnetic states were known, either a material was magnetic or it was non-magnetic, and the microscopic origin of magnetic materials remained unknown.

There have been two milestones for the understanding of magnetic order: The discovery of the *electron* in the 1890s and the discovery of its intrinsic angular momentum, the *spin*, in the 1920s. The spin causes a magnetic moment and in most materials, the electrons and their spins arrange in a way that all magnetic moments cancel. However, in some materials it is energetically favorable for the electrons to align their spins in a specific way, leading to magnetic order in such systems. Iron (Fe), which is the most abundant element in the Earth, exhibits a spontaneous net magnetization in its natural body-centered cubic (bcc) crystal structure, which is due to a parallel alignment of the unpaired electron spins and is called *ferromagnetism* (from the Latin

[1] Romagnosi found how an electric charge can deflect a magnetic needle, but his results were not paid attention to. In 1820, Christian Oersted published his findings of how an electric current influences a magnetic needle, and is usually mentioned as the discoverer of electromagnetism [1].

word *ferrum*). However, the magnetic order of Fe structures depends sensitively on the arrangement of the Fe atoms and their environment. For example, γ-Fe crystallizes in the face-centered cubic (fcc) structure and exhibits an antiparallel alignment between neighboring spins which leads to a vanishing net magnetization and is called *antiferromagnetic* (AFM) order [2, 3]. Since the magnetic state of Fe is already very susceptible to the symmetry and the interatomic distance in the bulk structure, Fe nanostructures seem to be promising candidates for exotic magnetic ground states.

Numerous techniques with increasing spatial resolution have been developed in order to study magnetic nanostructures. These techniques range from the use of visible light (magneto-optical Kerr microscope) and X-ray absorption (e.g. Scanning X-ray magnetic circular dichroism), to the use of electron beams (e.g. Scanning electron microscope with spin analysis). At the ultimate limit, the spin-sensitive investigation of nanostructures with atomic resolution is realized by spin-polarized scanning tunneling microscopy (SP-STM) [4]. For more than 10 years SP-STM has been a well established technique, which allows the direct correlation of the magnetic structure with the topography and the electronic properties of the sample. In particular, Fe nanostructures have revealed interesting magnetic ground states when investigated with SP-STM. Fe deposited on the (110) surface of a tungsten (W) crystal exhibits FM order in the first atomic layer, while the magnetic ground state of the second atomic layer is a very inhomogeneous spin spiral [5]. By choosing the (001) surface of the W crystal as the substrate for Fe films, the magnetic ground state changes significantly. The first atomic layer shows an AFM ordering [6] which is not detectable by spatially averaging methods [7] demonstrating the advantage of the combination of spin-sensitivity and atomic resolution in SP-STM. A much more complex magnetic ground state has been reported for the first atomic layer of Fe on the Ir(111) surface, which has a quadratic magnetic unit cell even though the atomic lattice is hexagonal [8, 9].

In this thesis, I present SP-STM investigations of Fe nanostructures on two different Ir surfaces exhibiting complex non-collinear magnetic ground states. After a short introduction to the magnetic interactions which play a crucial role in the formation of their ground states (Ch. 2), I give a presentation of the concept of (SP-)STM (Ch. 3) and of the instrumentation and sample preparation steps (Ch. 4). In Ch. 5 I present a spin spiral ground state of Fe chains which self-organize on the reconstructed Ir(001) surface. The SP-STM measurements can be understood on the basis of *ab initio* calculations, and Monte-Carlo as well as Object Oriented MicroMagnetic Framework (OOMMF) simulations give insight into temperature and finite size effects. Chapter 6 deals with the discovery of a skyrmion lattice in the first atomic layer of Fe on Ir(111). The experimental results are in excellent agreement with *ab initio* calculations and simulations with an extended Heisenberg model.

2. Magnetic interactions

As mentioned in the previous chapter, magnetic phenomena on a macroscopic scale are known for quite a long time, but the microscopic origin could not be explained until the early 20th century. Only with the discovery of the electron and its inherent spin it became possible to describe fundamental interactions which give rise to macroscopic magnetic properties like ferromagnetism.

In this section I will give an overview of the magnetic interactions which play important roles for the investigated sample systems presented in Ch. 5 and Ch. 6.

2.1. Heisenberg exchange interaction

The Heisenberg exchange was first described independently by W. Heisenberg and P. Dirac in the year 1926 [10, 11]. It is an electron-electron interaction which is of purely quantum mechanical nature and in order to understand this interaction, a quantum mechanical description of the electron itself is needed[1].

Particles on the (sub-)atomic level cannot be described by the laws of classical mechanics. For instance, the description of an atom in terms of electrons orbiting the atomic nucleus using classical mechanics leads to a collision of the electrons with the nucleus, and therefore prohibits stable atoms. Another example where classical mechanics fails, is the interference pattern which occurs when a beam of particles hits a double slit (Young's experiment) [13]. Therefore, the behavior of sub-atomic particles, like the electron, can only be properly described using quantum mechanics.

In quantum mechanics the state of an electron is given by its wave function ψ and all observables, e.g. the location, the momentum or the angular momentum, are given by operators. In this case, the term *observable* means, that the variable is in principle observable, rather than the measurement result as in classical mechanics. The possible measurement results of the observables are the eigenvalues of the operator with their respective eigenstates. In addition to the above mentioned observables the electron possesses an intrinsic angular momentum with a magnetic moment, the so-called *spin*. The wave function ψ of the electron can be written as a product of its spatial wave function ϕ and its spin function χ

$$\psi = \phi\chi. \tag{2.1}$$

[1] A very good introduction into the Heisenberg exchange can be found in Blundell's textbook [12].

The spin can be characterized by the spin quantum number S, which has a value of $S = 1/2$ in the case of an electron, with the corresponding spin component along an arbitrary quantization axis z being $m_z = \pm 1/2$ (*up* and *down*). The behavior of the electron spin S is described by the spin angular momentum operator

$$\mathbf{S} = \frac{\hbar}{2}\sigma \tag{2.2}$$

where $\hbar$ is the reduced Planck constant and $\sigma = (\sigma_x, \sigma_y, \sigma_z)$ is a vector of the Pauli matrices [14]. The corresponding intrinsic magnetic moment $\mathbf{m}$ of the electron is

$$\mathbf{m} = -g\mu_\mathrm{B}\mathbf{S}/\hbar, \tag{2.3}$$

with the electron g-factor g and the Bohr magneton μ_B.

Two electron spins can couple via a scalar interaction C, which gives rise to the Hamiltonian

$$H = C \cdot \mathbf{S}_a \cdot \mathbf{S}_b, \tag{2.4}$$

where $\mathbf{S}_i$ are the spin operators for the two particles. The total spin of this coupled system $\mathbf{S}_{tot} = \mathbf{S}_a + \mathbf{S}_b$ can have the eigenvalues 0 or 1 and the energy eigenvalues of the Hamlitonian are

$$E = \begin{cases} C/4 & \text{for} \quad S = 1 \\ -3C/4 & \text{for} \quad S = 0. \end{cases} \tag{2.5}$$

The state with $S = 1$ is the *triplet* state due to its threefold degeneracy (m_z can have the values $-1, 0, 1$) and the state with $S = 0$ is the *singlet* state (m_z=0). By inserting Eq. 2.5 in the Hamiltonian in Eq. 2.4 the constant C can be expressed in dependence of the triplet energy E_T and singlet energy E_S leading to

$$H = -(E_S - E_T)\mathbf{S}_a \cdot \mathbf{S}_b. \tag{2.6}$$

Due to the fermionic nature of the electron, the overall wave function of the two electron system ψ_{tot} has to be antisymmetric with respect to exchange of particles. Since the overall wave function is a product of the spatial and the spin function

$$\psi_{tot} = \phi_{tot}\chi_{tot}, \tag{2.7}$$

either the spatial function is symmetric and the spin function has to be antisymmetric or vice versa. While the spin function for the triplet state χ_T is symmetric with respect to the exchange of particles, the singlet spin function χ_S is antisymmetric. Accordingly, the spatial functions have to be antisymmetric for the triplet state (ψ_T) and symmetric for the singlet state (ψ_S) leading to the overall wave functions

$$\psi_S = \frac{1}{\sqrt{2}}[\phi_a(\mathbf{r}_1)\phi_b(\mathbf{r}_2) + \phi_a(\mathbf{r}_2)\phi_b(\mathbf{r}_1)]\chi_S \tag{2.8}$$

$$\psi_T = \frac{1}{\sqrt{2}}[\phi_a(\mathbf{r}_1)\phi_b(\mathbf{r}_2) - \phi_a(\mathbf{r}_2)\phi_b(\mathbf{r}_1)]\chi_T \tag{2.9}$$

for the two electrons at the positions $\mathbf{r}_1$ and $\mathbf{r}_2$, respectively. The energies for these two states are $E_S = \int \psi_S^* H \psi_S \mathrm{d}\mathbf{r}_1 \mathrm{d}\mathbf{r}_2$ and $E_T = \int \psi_T^* H \psi_T \mathrm{d}\mathbf{r}_1 \mathrm{d}\mathbf{r}_2$, while their difference is given by

$$E_S - E_T = 2 \int \phi_a^*(\mathbf{r}_1)\phi_b^*(\mathbf{r}_2) H \phi_a(\mathbf{r}_2)\phi_b(\mathbf{r}_1) \mathrm{d}\mathbf{r}_1 \mathrm{d}\mathbf{r}_2. \tag{2.10}$$

By defining the *exchange integral* J as

$$J = \frac{E_S - E_T}{2} = \int \phi_a^*(\mathbf{r}_1)\phi_b^*(\mathbf{r}_2) H \phi_a(\mathbf{r}_2)\phi_b(\mathbf{r}_1) \mathrm{d}\mathbf{r}_1 \mathrm{d}\mathbf{r}_2, \tag{2.11}$$

the effective Hamiltonian in Eq. 2.6 can be written as

$$H = -2J \ \mathbf{S}_a \cdot \mathbf{S}_b. \tag{2.12}$$

For $J > 0$, meaning that the triplet state is lower in energy compared to the singlet state, the spin wave function is symmetric, hence the spins are aligned parallel or ferromagnetic (FM). In the case of $J < 0$ the singlet state is energetically favored and the spin wave function is antisymmetric leading to an antiparallel or antiferromagnetic (AFM) alignment of the two spins. Equation 2.12 can be generalized for interactions between more than two spins, leading to the *Heisenberg model*

$$H_{\mathbf{exch}} = -\sum_{ij} J_{ij} \mathbf{S}_i \cdot \mathbf{S}_j. \tag{2.13}$$

While up to here the description of the exchange interaction was quantum mechanical, it is common to use a classical Heisenberg model in solid state physics. In the classical approach the spin operator $\mathbf{S}$, its eigenvalue S and the direction m_z are replaced by a vector with a certain length which can point in any direction.

For many magnetic systems the exchange constant J_{ij} can be approximated by a single constant J for nearest neighbor spins which leads to the aforementioned (collinear) FM or AFM ordering. However, the general solution of the classical Heisenberg model is a (non-collinear) flat *spin spiral* in which the spin $\mathbf{S}_i$ at the position $\mathbf{r}_i$ is given by

$$\mathbf{S}_i = S \cdot \begin{pmatrix} 0 \\ \sin(\mathbf{q} \cdot \mathbf{r}_i) \\ \cos(\mathbf{q} \cdot \mathbf{r}_i) \end{pmatrix}, \tag{2.14}$$

with the spin spiral vector $\mathbf{q}$. The spin spiral state occurs when also beyond-nearest neighbor exchange is considered and it is due to frustration effects between the competing interactions. For a one-dimensional crystal along the z-axis with the lattice constant a, a cycloidal spiral given by Eq. 2.14 is characterized by $\mathbf{q} = (0, 0, q)$. Any q between $q = 0$, which is the FM solution, and $q = 0.5\frac{2\pi}{a}$, which describes the AFM state, results in a non-collinear ground state, with the characteristic spin spiral angle

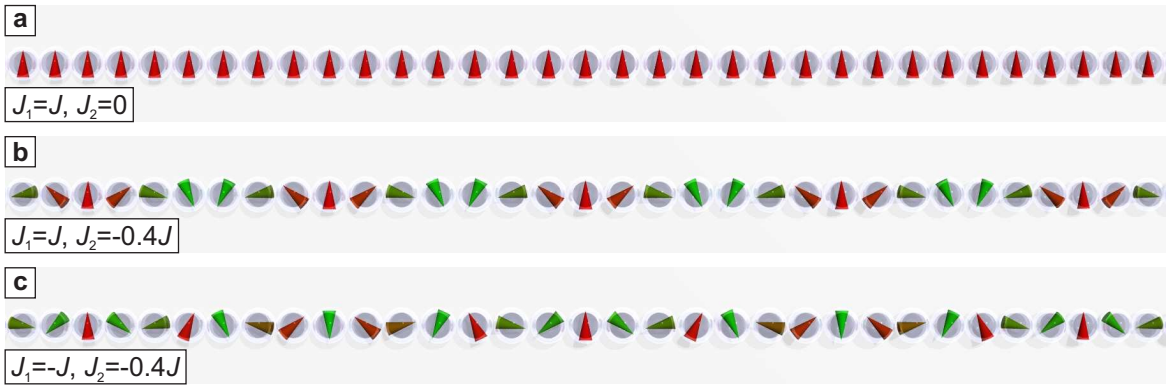

Figure 2.1: Solutions of the Heisenberg model with nearest and next-nearest neighbor exchange. **a**, FM order for $J_1 > 0$ and $J_2 = 0$. **b**, Spin spiral ground state for $J_1 > 0$ and $J_2 = -0.4J_1$ with the spin spiral angle $\theta \approx 51°$. **c**, For $J_1 < 0$ and $J_2 = 0.4J_1$ the angle results to $\theta \approx 129°$.

$\theta = 2\pi q$. This is illustrated in Fig. 2.1 which exemplarily shows the magnetic ground state of the one-dimensional Heisenberg model for nearest neighbor exchange (J_1) and next-nearest neighbor interactions (J_2). The constant J is assumed to be positive and Figure 2.1 a shows the trivial solution for $J_1 = J$ and $J_2 = 0$ which gives the FM ground state. For $J_1 = J$ and $J_2 = -0.4J$ the resulting magnetic state is a rather slow rotating spin spiral with $\theta < 90°$, see Fig. 2.1 b. When both coupling constants are negative, $J_1 = -J$ and $J_2 = -0.4J$ the spiral rotates faster with $\theta > 90°$, see Fig. 2.1 c.

2.2. Spin-orbit interaction

The *spin-orbit interaction* (SOI) describes any interaction of the electron's spin with its motion around the atom's nucleus and is responsible for the *magnetic anisotropy energy* and the *Dzyaloshinskii-Moriya interaction*.

2.2.1. Magnetic anisotropy energy

In the previous section the spin of the electron was regarded to be independent of and therefore separated from the orbital momentum of the electron's motion. In reality the two angular momentums experience a weak coupling which lifts the degeneracy of the electron's energy levels with respect to the spin state and thereby gives rise to a fine structure in the energy. This is due to a magnetic field $\mathbf{B}$ the electron experiences

in its rest frame during its motion through the electric field $\mathbf{E}$ of the nucleus

$$\mathbf{B} = -\frac{\mathbf{v} \times \mathbf{E}}{c^2}, \tag{2.15}$$

with the electron's velocity $\mathbf{v}$ and the speed of light c. The magnetic moment of the electron couples to the magnetic field which leads to a lower energy for one spin direction compared to the other spin direction. Since the velocity $\mathbf{v}$ is directly proportional to the electron's momentum $\mathbf{p}$ and the electric field is the gradient of the electric potential V, eq. 2.15 can be written as

$$\mathbf{B} \propto \frac{1}{r}\frac{\partial V(r)}{\partial r}\mathbf{r} \times \mathbf{p} = \frac{1}{r}\frac{\partial V(r)}{\partial r}\mathbf{L} \tag{2.16}$$

in the approximation of a spherically symmetric potential; $\mathbf{L}$ is the orbital angular momentum. The strength of the magnetic field is directly proportional to the gradient of the electric potential, hence the SOI has significant contributions to the energy in heavy atoms (Ir, Pt, W, ...) while it is almost negligible in atoms with an atomic number $Z < 30$. The energy contribution of the SOI to the electron state is the influence of $\mathbf{B}$ on the magnetic moment of the electron $\mathbf{m}$

$$H_{\mathrm{SOI}} = \mathbf{m} \cdot \mathbf{B} \propto \frac{1}{r}\frac{\partial V(r)}{\partial r}\mathbf{L} \cdot \mathbf{S}. \tag{2.17}$$

In magnetic solid state systems the potential is determined by the crystal structure and its symmetry. Depending on the crystallographic direction the potential varies its shape leading to different gradients and ultimately different energies for the electron's spin state, the magnetic anisotropy energy (MAE). Usually the energetically most favorable direction is called *easy axis* or *plane* and the energetically unfavored direction is either the *hard axis* or *plane*. In the simplest case the system has a *uniaxial magnetic anisotropy*, e.g. FM cobalt (Co) in its hexagonal close-packed (hcp) crystal structure exhibits an easy axis of magnetization along the c-axis of the crystal. The spontaneous magnetization aligns along the c-axis and upon a rotation away from the easy axis the MAE increases with a maximum for a magnetization perpendicular to the easy axis. This dependence of the energy on the angle φ between the easy axis and the magnetization direction is usually expressed by an expansion in powers of $\sin^2 \varphi$

$$E_{\mathrm{ani}} = K_1 \sin^2 \varphi + K_2 \sin^4 \varphi + K_3 \sin^6 \varphi + \ldots. \tag{2.18}$$

By considering a discrete lattice of spin $\mathbf{S}_i$ and only taking the first term of the expansion into account, Eq. 2.18 becomes

$$E_{\mathrm{ani}} = \sum_i K \sin^2 \varphi_i, \tag{2.19}$$

with the angle φ_i between $\mathbf{S}_i$ at the lattice position i and the anisotropy axis. For $K < 0$ the lowest energy for the spins is in a plane perpendicular to the anisotropy axis, while for $K > 0$ the system exhibits an easy axis. Both sample systems presented in Ch. 6 and Ch. 5 of this thesis bare an anisotropy with an out-of-plane easy axis. The so-called *Ising model* is the limit of $K \gg 0$ in which the spins are forbidden to point in directions different from the easy axis.

2.2.2. Dzyaloshinskii-Moriya interaction

In recent years the Dzyaloshinskii-Moriya (DM) interaction gained more and more attention since it can play a crucial role in the formation of complex, non-collinear magnetic structures on surfaces [15] as well as in bulk systems [16]. The DM interaction is an antisymmetric exchange interaction and, as the MAE, a consequence of the spin-orbit interaction. I. Dzyaloshinskii was the first to describe this interaction in 1958 [17] and based on symmetry arguments he could explain the weak spontaneous magnetization observed in antiferromagnetic crystals. α-Fe_2O_3, also known as hematite, is a mineral which crystallizes in a rhombohedral structure and exhibits two possible magnetic configurations. In both magnetic structures the magnetic moments of the Fe atoms form an antiferromagnetic $\uparrow\downarrow\downarrow\uparrow$-state in which the moments are either aligned along the [111]-direction or slightly canted with respect to the [111]-direction. The *magnetic symmetry* of these states is given by the symmetries of the crystal with an additional symmetry element R, which describes the change of the spin sign $S(x, y, z) \rightarrow -S(x, y, z)$. Dzyaloshinskii showed that a spontaneous magnetic moment may exist only when it is invariant under the action of all symmetry transformations.

By expanding the thermodynamical potential he revealed that it consists of terms representing the Heisenberg exchange, terms which are the magnetic anisotropy and an additional term E_{DM} which is proportional to the cross product of neighboring spins

$$E_{\mathrm{DM}} = -\mathbf{D} \cdot (\mathbf{S}_i \times \mathbf{S}_j), \tag{2.20}$$

where $\mathbf{D}$ is the Dzyaloshinskii-Moriya vector. Due to the cross product between the neighboring spins S_i and S_j this term is minimized for a perpendicular alignment of the spins. Two years later, T. Moriya developed a theoretical model for this interaction based on anisotropic superexchange including spin-orbit interaction [18]. He generalized the work of Dzyaloshinskii for any crystal structure and showed qualitatively that E_{DM} becomes largest when the crystal symmetry is sufficiently low and vanishes for highly symmetric crystals. Furthermore, he could deduce from his model the following rules [18]:

> "The two ions 1 and 2 are located at the points A and B, respectively, and the point bisecting the straight line AB is denoted by C.

1. When a center of inversion is located at C, $\mathbf{D} = 0$.
2. When a mirror plane perpendicular to AB passes through C, $\mathbf{D} \parallel$ mirror plane or $\mathbf{D} \perp AB$.
3. When there is a mirror plane including A and B, $\mathbf{D} \perp$ mirror plane.
4. When a two-fold rotation axis perpendicular to AB passes through C, $\mathbf{D} \perp$ two-fold axis.
5. When there is an n-fold axis ($n \geq 2$) along AB, $\mathbf{D} \parallel AB$."

The third case applies for nanostructures on surfaces with a rectangular atomic arrangement as the (001) surface of a bcc crystal, leading to a DM vector in the surface plane [19]. For the bcc(110) surface or the fcc(111) surface the direction of the DM vector can only be restricted to a plane perpendicular to the bond [20]. However, additional symmetry considerations and comparison to experimental data show that also for these surfaces the DM vector usually lies in the surface plane or has at least an in-plane component [21, 15, 22].

2.3. Higher order exchange interactions

Beyond the Heisenberg model, higher order exchange interactions exist which can be derived by fourth order perturbation expansion of the Hubbard model [23], namely the *four-spin interaction* and *biquadratic interaction*. Although these two interactions are usually very small compared to the Heisenberg exchange and therefore often neglected, they provide a rich phase space of magnetic structures.

The energy contribution due to the four-spin interaction is given by

$$E_{\text{4spin}} = -\sum_{ijkl} K_{4,ijkl}[(\mathbf{S}_i\mathbf{S}_j)(\mathbf{S}_k\mathbf{S}_l) + (\mathbf{S}_i\mathbf{S}_l)(\mathbf{S}_j\mathbf{S}_k) - (\mathbf{S}_i\mathbf{S}_k)(\mathbf{S}_j\mathbf{S}_l)], \tag{2.21}$$

which occurs due to electron hopping between the four lattice sites $(ijkl)$. Its coupling constants $K_{4,ijkl}$ define the strength of the interaction and by considering only nearest-neighbor interaction $K_{4,ijkl}$ reduces to one constant K_4 with $(ijkl)$ lying on adjacent lattice sites.

In the case of a two-dimensional triangular lattice the lattice sites form the smallest possible diamond. Depending on the sign of K_4 the four-spin interaction favors different spin configurations. For $K_4 > 0$ the FM order and a row-wise AFM order are energetically the most favorable structures and for $K_4 < 0$ a structure with one spin pointing in the opposite direction of the other three spins is favored, resulting in alternating FM and AFM rows [24].

The biquadratic interaction is given by

$$E_{\mathrm{bi}} = -\sum_{ij} B_{ij}(\mathbf{S}_i \cdot \mathbf{S}_j)^2, \tag{2.22}$$

where B_{ij} couples the spins at the lattice sites i and j. Restricted to nearest neighbor interaction, similar to the four-spin interaction, B_{ij} reduces to one coupling constant B. For $B > 0$ the biquadratic interaction favors an (anti-)parallel alignment of the neighboring spins, either FM or AFM, while for $B < 0$ the spins prefer to align perpendicular to each other, which leads to a non-collinear ground state [24].

Typically these interactions are rather small, but they can have a strong influence on the magnetic ground state of a system when the Heisenberg exchange is small. In Ch. 6, I show that the four-spin interaction plays a crucial role in the formation of the magnetic ground state of the Fe ML on the Ir(111) surface.

3. Scanning tunneling microscopy

3.1. The tunnel effect in one dimension

The working principle of the *Scanning Tunneling Microscope* (STM) is based on the tunnel effect – a quantum-mechanical phenomenon – which can be explained by the wave-particle duality. Consideration of a one-dimensional potential barrier helps in order to understand this effect. In classical mechanics an electron with the energy E cannot overcome a potential barrier V_0 if $E < V_0$, it will be reflected as shown in Fig. 3.1 a. In quantum mechanics the electron has to be treated not only as a particle but also as a wave function Ψ and thus has a finite probability to "tunnel" through the potential barrier even if $E < V_0$, as is shown in Fig. 3.1 b. The wave function Ψ of the electron has to satisfy the time-independent Schrödinger equation

$$-\frac{\hbar^2}{2m_e} \cdot \Delta\Psi + V \cdot \Psi = E \cdot \Psi, \tag{3.1}$$

where m_e is the electron mass and $\hbar$ is the reduced Planck constant. In the case of the one dimensional rectangular barrier sketched in Fig. 3.1 b and with an Ansatz of

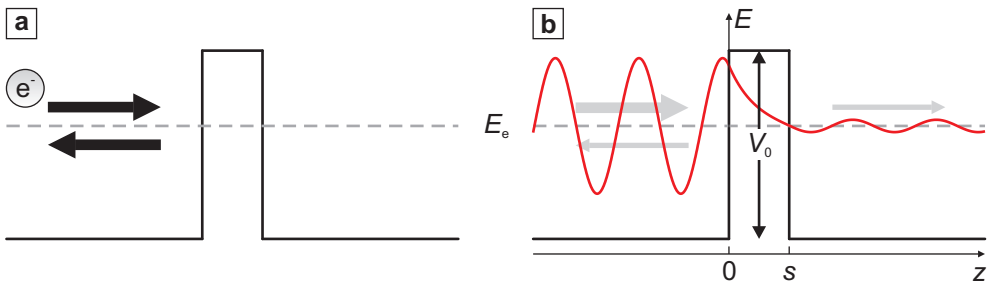

Figure 3.1: Tunnel effect in one dimension. **a**, In classical physics, an electron which is moving in a potential will be reflected at a potential barrier if the energy of the barrier is higher than the energy of the electron. **b**, In quantum mechanics the electron has a non-zero probability to traverse any potential barrier with a finite height and width, since the electron has to be described by a wave function Ψ which has to satisfy the time-independent Schrödinger equation.

plane waves the wave function Ψ of the electron will be

$$\Psi(z) = \begin{cases} \exp(\mathrm{i}kz) + A\exp(-\mathrm{i}kz) & \text{for} \quad z < 0 \\ B\exp(-\kappa z) + C\exp(\kappa z) & \text{for} \quad 0 \leq z \leq s \\ D\exp(\mathrm{i}kz) & \text{for} \quad z > s \end{cases}, \tag{3.2}$$

with the two constants

$$k = \sqrt{\frac{2mE}{\hbar^2}} \quad \text{and} \quad \kappa = \sqrt{\frac{2m(V_0 - E)}{\hbar^2}}, \tag{3.3}$$

where k is the wave number and κ is the decay constant. As depicted in figure 3.1 the wave function of the electron has a plane wave character if $E > V_0$. Inside the potential barrier, in the case of $E < V_0$, the electron wave function Ψ decays exponentially, which means that there will *always* be a finite probability for the electron to cross the potential barrier as long as $V_0 < \infty$ and $s < \infty$.

Using the *wave matching method*, meaning that the wave function has to be continuously differentiable, one can derive A, B, C and D from Eq. 3.2 and thus the transmission coefficient which is the ratio between the transmitted and the incident current density j_t and j_i

$$T \equiv \frac{j_\mathrm{t}}{j_\mathrm{i}} = |D^2| = \frac{1}{1 + \frac{(k^2+\kappa^2)^2}{(4k^2\kappa^2)} \cdot \sinh(\kappa s)^2}. \tag{3.4}$$

In the limit of $\kappa s \gg 1$ the transmission coefficient T can be simplified to

$$T \approx \frac{16k^2\kappa^2}{(k^2+\kappa^2)^2} \cdot \exp(-2\kappa s). \tag{3.5}$$

This means that the tunnel current in this model depends exponentially on the barrier width s which equals the tip-sample separation in STM experiments. Plugging in typical tunnel parameter ($V_0 - E = 4\,\mathrm{eV}$ and $s = 5\,\text{Å}$) one gets an increase in the tunnel current by almost one order of magnitude if the distance of the electrodes is decreased by one Å. Even though this model is too simple to describe realistic STM experiments it explains the high sensitivity to height changes in the sample topography.

3.2. Experimental realization

As indicated in the previous section the tunnel current between two electrodes is extremely sensitive to the distance between them and it is used in the STM to determine the structural configuration of a sample. But in order to use the current as a measurement signal the counter electrode, which is a very sharp, metallic tip, has to be positioned with sub-nanometer precision. This is accomplished by using piezoelectric

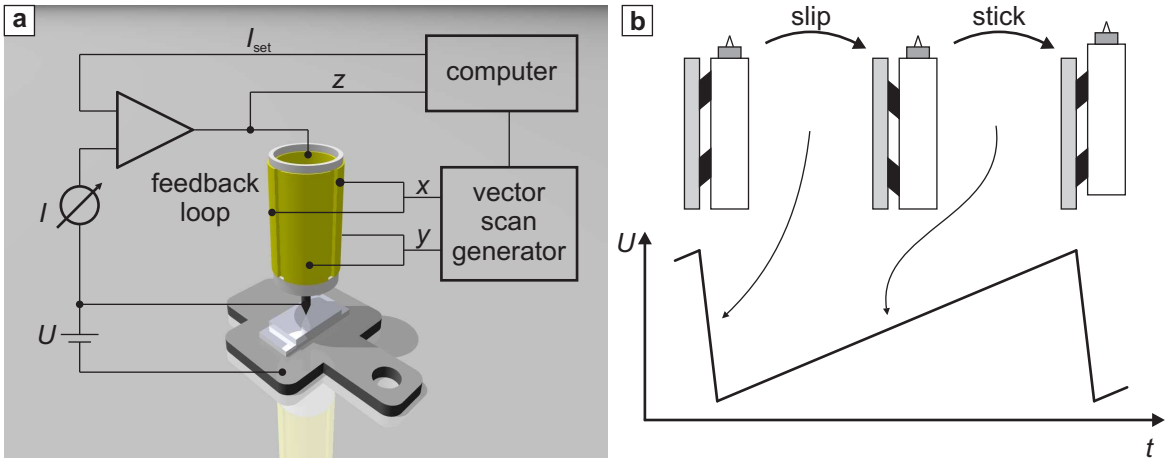

Figure 3.2: **a**, Working principle of an STM. The tunnel current is kept constant at a set point I_{set} using a feedback loop while the tip scans laterally across the surface by applying voltages to the $x-$ and $y-$electrodes of the tube scanner. The feedback loop adjusts the tip height until the measured current is identical to the set point. A computer records the $\Delta z(x, y)$ points and constructs a topographic map out of those height changes. **b**, Schematic drawing of the coarse approach unit. The tube scanner (gray) with the tip is mounted in a sapphire prism (white) which is clamped by six stacks of piezoelectric material (black). A sawtooth voltage is applied to the stacks which leads to a shear motion of the stacks with two different speeds. Due to its inertia the prism will not follow the motion if it is too fast and will thereby slip on the stacks. If the motion of the stacks is slow the prism will stick to the stacks and will be moved.

actuators to control the tip-sample separation as well as the scan direction parallel to the surface [25, 26].

The piezoelectric effect describes the ability of a material to generate electric fields by applying mechanical stress to the material. In an STM the reverse piezoelectric effect, stress or strain in a material due to an applied electric field, is exploited to move the tip very precisely with respect to the sample surface. The movement of the tip is divided in two independent motions: i.) the *coarse approach* and ii.) the fine adjustment of the distance between tip and sample which is also used for scanning the surface.

In the STMs used for this study the fine adjustment was ensured by a tube scanner made of piezoelectric material as illustrated in Fig. 3.2 a. In this geometry the top part of the scanner is fixed. If a voltage U_z is applied to the z-electrode inside the tube, the whole scanner will either contract or elongate depending on the sign of the applied voltage, which can be used to adjust the distance between the tip and the sample. The piezoelectric material on the outside of the scanner is divided in four independent electrodes which can be addressed by separate connections. Applying a voltage to just

one of the four electrodes, this electrode will either contract or elongate and therefore the whole scanner will bend. This motion can be used to position the tip precisely at one point of the surface and to scan a surface area by applying voltages U_x and U_y.

With the coarse positioning device the scanner with the STM tip can be moved away from or closer to the sample. For this motion the scanner is fixed to a sapphire prism which is moved by stacks made of piezoelectric material using the slip-stick mode, see Fig. 3.2 b. In this mode a sawtooth voltage is applied to the stacks which leads to a shearing of the stacks. At the steep edge of the sawtooth the shearing of the stacks is so fast, that the prism will not follow the motion due to its inertia: it *slips* on the piezoelectric stacks. During the gentle incline of the sawtooth voltage the surface of the prism *sticks* to the surface of the stacks and therefore follows the movement of the stacks. By repeating the cycle the scanner-tip unit can be moved macroscopically.

Since the tip has to be positioned only $\approx 5\,\text{Å}$ above the sample for measurements, and it is also crucial not to crash the tip into the surface, the two motions described above are executed automatically to establish a tunnel current. First, the scanner is elongated to check if a tunnel current can be stabilized in the current position of the prism. If no tunnel current is detected at full expansion of the scanner the tip is retracted by contracting the scanner and the prism is moved closer to the surface by one coarse step of the piezoelectric shear elements. The two motions are executed alternately until the measured tunnel current between tip and sample matches the set point I_{set}.

If the tunnel current between the tip and the sample is established, there are two possible measurement modes to obtain topographic images of the sample surface.

In the *constant height mode* the tip is scanned over the surface at one fixed height z while the tunnel current I is recorded. A change in the tunnel current in this measurement mode is an indicator for a change of the distance d between the tip and the sample and therefore it indicates a change in the topography of the sample, e.g. a step edge (see Fig. 3.3 a). One drawback of this mode is that the distance between the tip and the sample is not controlled which could lead to an accidental crash of the sample and the tip. To avoid such tip-sample contacts it is much more common to use the *constant current mode* where a feedback loop controls the distance between tip and sample. A feedback loop keeps the tunnel current I_{out} fix to a set point I_{set} by adjusting the tip height z. In this mode the tip is scanned with a constant distance and a constant current over the surface and all the changes in the topography of the surface lead to changes in the tip height (see Fig 3.3 b). However, a perfect constant current mode cannot be realized in practice since the feedback loop has a finite response time.

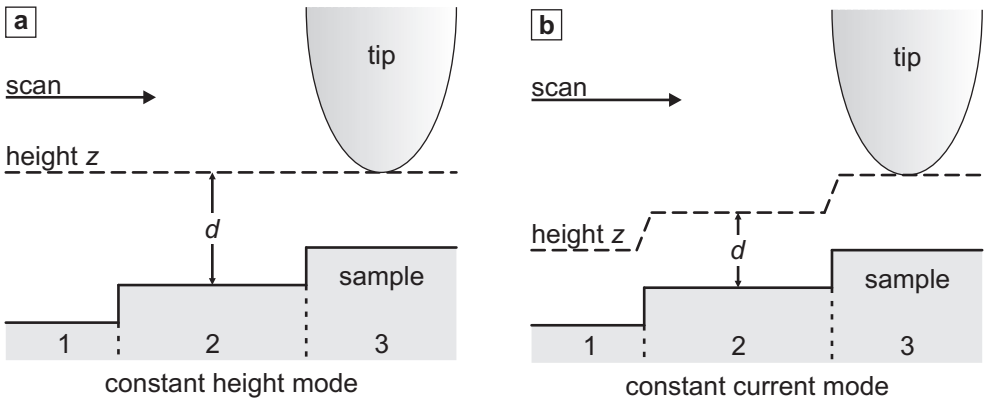

Figure 3.3: Two different measurement modes. **a**, In the constant height mode the tip is scanned with a constant height z over the surface and the tunnel current I is the measurement signal. Differences in the tunnel current indicate differences in the height profile of the sample. **b**, In the constant current mode the tunnel current between tip and sample is kept constant by a feedback loop and differences in the height profile of the sample lead to a change in the z position of the tip, which is the measurement signal.

3.3. Topography

Although the model presented in Sec. 3.1 explains the exponential dependence of the tunnel current on the separation of the two electrodes a more generalized model is needed to interpret STM experiments. First of all the model presented in Sec. 3.1 is only one-dimensional while STM experiments are mostly carried out in three dimensions and secondly the electronic structure of the two electrodes is not accounted for.

3.3.1. Time-dependent perturbation theory

To describe the tunnel current between two metallic electrodes J. Bardeen used first-order time-dependent perturbation theory [27]. In this work the tunnel current is described by the overlap of the electron wave functions of the two electrodes. From the calculations of first-order perturbations the transition rate $\omega_{\mu\nu}$ between an electron state Ψ_ν^{T} in the tip and an electron state Ψ_μ^{S} in the sample is given by

$$\omega_{\mu\nu}(t) = \frac{2\pi}{\hbar}\delta(E_\nu^{\mathrm{T}} - E_\mu^{\mathrm{S}})\,|M_{\mu\nu}|^2\,, \tag{3.6}$$

where the δ-function guarantees the required conservation of energy. $M_{\mu\nu}$ is Bardeen's matrix element and only depends on the wave functions Ψ_ν^{T} and Ψ_μ^{S} on a separation

plane Σ in between the electrodes:

$$M_{\mu\nu} = -\frac{\hbar^2}{2m} \int_{\Sigma} \mathrm{d}\mathbf{S} \ \left(\Psi_{\nu}^{\mathrm{T}*} \nabla \Psi_{\mu}^{\mathrm{S}} - \Psi_{\mu}^{\mathrm{S}} \nabla \Psi_{\nu}^{\mathrm{T}*} \right). \tag{3.7}$$

From the transition rate in Eq. 3.6 it is possible to calculate the net current between the two electrodes by summation over the states μ and ν. The current is given by

$$I = \frac{4\pi e}{\hbar} \sum_{\mu\nu} \left[f(E_{\nu}^{\mathrm{T}} - E_{\mathrm{F}}^{\mathrm{T}}) - f(E_{\mu}^{\mathrm{S}} - E_{\mathrm{F}}^{\mathrm{S}}) \right] |M_{\mu\nu}|^2 \delta \left(E_{\nu}^{\mathrm{T}} - E_{\mu}^{\mathrm{S}} \right), \tag{3.8}$$

where $f(\ldots)$ is the Fermi-Dirac distribution. In this expression for the tunnel current no voltage is applied to any of the two electrodes. Therefore the transition rate from the tip to the sample is equal to the transition rate from the sample to the tip and no net current flows between the electrodes. If one substitutes the summation over discrete states by an integration over the density of states and applies a voltage to one of the electrodes, the tunnel current can be expressed as

$$\begin{aligned} I \ = \ & \frac{4\pi e}{\hbar} \int \mathrm{d}\epsilon \left[f(E_{\mathrm{F}}^{\mathrm{T}} - eU + \epsilon) - f(E_{\mathrm{F}}^{\mathrm{S}} + \epsilon) \right] \\ & \times \rho^{\mathrm{T}}(E_{\mathrm{F}}^{\mathrm{T}} - eU + \epsilon) \rho^{\mathrm{S}}(E_{\mathrm{F}}^{\mathrm{S}} + \epsilon) |M(E_{\mathrm{F}}^{\mathrm{S}} + \epsilon, E_{\mathrm{F}}^{\mathrm{T}} - eU + \epsilon)|^2, \end{aligned} \tag{3.9}$$

where ρ^{T} and ρ^{S} are the density of states for the tip and the sample, respectively. This means that the tunnel current in Eq. 3.9 depends on the electronic structure of the sample as well as the tip. In the limit of temperature $T \to 0$, meaning that the Fermi distribution becomes a step function, Eq. 3.9 simplifies to

$$I = \frac{4\pi e}{\hbar} \int_{0}^{eU} \mathrm{d}\epsilon \, \rho^{\mathrm{T}}(E_{\mathrm{F}}^{\mathrm{T}} - eU + \epsilon) \rho^{\mathrm{S}}(E_{\mathrm{F}}^{\mathrm{S}} - \epsilon) |M|^2. \tag{3.10}$$

With this Ansatz of Bardeen it is theoretically possible to exactly calculate the tunnel current between the tip and the sample in an STM. However, one problem is the determination of the matrix element $M_{\mu\nu}$ (Eq. 3.7) since it depends on the wave function of the tip and the sample. Since it is (almost) impossible to identify the atomic structure of the STM tip also the wave function of the tip is unknown.

3.3.2. Tersoff-Hamann model

J. Tersoff and D. R. Hamann were the first to apply Bardeen's model to STM experiments. In order to calculate the tunnel current without the exact knowledge of the atomic structure of the tip, Tersoff and Hamann introduced a tip which is approximated with a spherical symmetry and only s-type wave functions are allowed to contribute to the tunnel current [28, 29]. In Bardeen's model (Eq. 3.8) the potentials

of the tip and the sample are (almost) negligible at the position of the separation plane Σ. Therefore, the wave functions of the sample and the tip (Ψ_μ^{S} resp. Ψ_ν^{T}) have to satisfy the vacuum Schrödinger equation

$$\left[\Delta - \kappa^2\right] \Psi = 0, \tag{3.11}$$

with $\kappa^2 = 2m|E|/\hbar^2$. With the approximation that the tip is just a single atom which has an s-orbital as wave function, this equation has two solutions which are the spherical, modified Bessel functions of first and second kind. Since the spherical, modified Bessel function of first kind cannot be normalized, it can be discarded and the solution for Eq. 3.11 is

$$\Psi_\nu^{\mathrm{T}}(\mathbf{r} - \mathbf{R}) = C \frac{\exp(-\kappa|\mathbf{r} - \mathbf{R}|)}{\kappa|\mathbf{r} - \mathbf{R}|} \quad \text{mit} \quad |\mathbf{r} - \mathbf{R}| \neq 0. \tag{3.12}$$

In this equation C is a normalization constant, $\mathbf{R}$ gives the position of the tip atom and $\mathbf{r}$ points to the separation plane Σ. This configuration is depicted in figure 3.4. The condition $|\mathbf{r} - \mathbf{R}| \neq 0$ is always fulfilled since the separation plane is in between

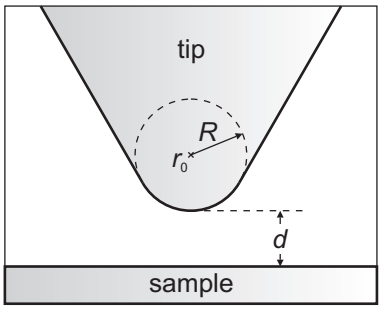

Figure 3.4: Scheme of the tunnel junction geometry in the Tersoff-Hamann model. $\mathbf{R}$ marks the position of the center of a spherical tip with the radius r_0 and d is the smallest distance between the tip and the sample.

the tip and the sample. With this wave function plugged into Eq. 3.7 the solution for the matrix element is

$$M_{\mu,s}(\mathbf{R}) = -\frac{2\pi C\hbar^2}{\kappa m} \Psi_\mu^{\mathrm{S}}(\mathbf{R}), \tag{3.13}$$

where the index s denotes the s-type wave function for the tip. With this matrix element the equation for the tunnel current (Eq. 3.10) results in

$$I(\mathbf{R}, U) = \frac{16\pi^3 C^2 \hbar^3 e}{\kappa^2 m^2} \rho^{\mathrm{T}} \int_0^{eU} \mathrm{d}\epsilon\, \rho_{\mathrm{local}}^{\mathrm{S}}(\mathbf{R}, E_{\mathrm{F}}^{\mathrm{S}} + \epsilon). \tag{3.14}$$

A closer look to this equation shows that the tunnel current in the Tersoff- Hamann model is directly proportional to the integrated, *local density of states* (LDOS) of the sample $\rho_{\mathrm{local}}^{\mathrm{S}}$ at the position of the tip atom.

While this model reproduces experimentally observed corrugation amplitudes for quite open structures, where the lateral distance between two objects is $a_0 \geq 6\,\text{Å}$, very

well, it fails to describe corrugation amplitudes for densely packed metal surfaces, where the distance between two atoms is $a_0 = 2 \ldots 3\,\text{Å}$. Another problem of this model is the fact that for most tip materials, which are heavy transition metals like tungsten, platinum and iridium, the s-type orbital is not a good approximation.

3.3.3. Chen's expansion of the Tersoff-Hamann model

The problems which arise from the Tersoff-Hamann model can be overcome by expanding the model using generalized wave functions for the tip. Such an expansion was introduced by C. J. Chen [30, 31, 32, 33] who considered the general solutions of the vacuum Schrödinger equation (Eq. 3.11)

$$\Psi^{\mathrm{T}}(\mathbf{r}) = \sum_{l,m} c_{l,m} k_l(\kappa|\mathbf{r} - \mathbf{R}|) Y_{l,m}(|\mathbf{r} - \mathbf{R}|). \tag{3.15}$$

In those wave functions $Y_{l,m}$ are the spherical harmonics and k_l are the modified Bessel functions of the second kind while $c_{l,m}$ is a normalization coefficient. For the simplest case $l = 0$ the solution leads to the Tersoff-Hamann model. If the tip is described by a p_z-type orbital, an evaluation of the spherical harmonic and the modified Bessel function results in the wave function

$$\Psi^{\mathrm{T}}_{p_z}(\mathbf{r}) \propto \frac{\partial}{\partial Z} \Psi^{\mathrm{T}}_{s} \mathbf{r}. \tag{3.16}$$

Inserting this wave function into Bardeen's transition matrix element (Eq. 3.7) leads to (analogous to the Tersoff-Hamann model)

$$M_{\mu,p_z}(\mathbf{R}) \propto \frac{\partial}{\partial Z} \Psi^{\mathrm{S}}_{\mu}(\mathbf{R}). \tag{3.17}$$

This means, that the matrix element is proportional to the derivative of the sample wave function at the position of the tip, if the tip is described by a p_z-type orbital. In this way the matrix element can be derived also for higher order orbitals, which is known as the derivative rule of Chen [31]. Using p- or d-type orbitals for the tip, the experimentally observed corrugation amplitudes of densely packed metal surfaces can be explained. One possible way to determine the tip apex structure experimentally was recently proposed by Vitali *et al.* [34] by measuring vibrational excitation spectra and comparing those to theoretical calculations.

3.3.4. Effects of the electronic structure of the sample

From all the theoretical considerations in the previous sections it is obvious that the tunnel current carries information about several different sample properties. In a first approximation (see Sec. 3.1) the tunnel current depends exponentially on the distance

between tip and sample, see Eq. 3.5. By applying a more precise model of the tunnel junction in Sec. 3.3.2 it becomes clear from Eq. 3.10 that also the LDOS of the sample has an important contribution to the tunnel current. Figure 3.5 shows the tip-sample

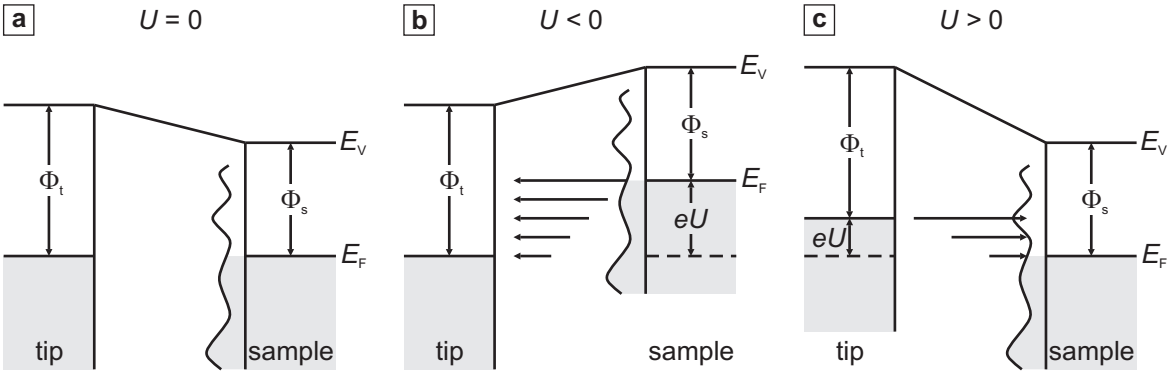

Figure 3.5: Schematic drawings of the tip-sample system for three different applied bias voltages. **a**, For $U = 0$ the Fermi energies of the tip and the sample are identical and no tunnel current is flowing between the two electrodes. **b** and **c**, With $U \neq 0$ the Fermi levels of the tip and sample are not at the same energy and depending on the polarity of the bias voltage electrons tunnel from the sample to the tip or vice versa.

system in tunnel contact in three different states. In these schematic drawings Φ_n indicates the work function of the respective electrode and E_F and E_V are the Fermi energy and the vacuum energy, respectively. In Fig. 3.5 a no voltage is applied, the system is in equilibrium and the same number of electrons tunnel from the tip to the sample as vice versa, which leads to a vanishing net tunnel current. In this state sample and tip have the same Fermi energy which indicates the energy of the highest occupied state. By applying a negative voltage to the sample (Fig. 3.5 b) the Fermi energy of the sample shifts to a higher value with respect to the Fermi energy of the tip. This leads to a non-zero tunnel current since electrons tunnel from the occupied states in the sample to unoccupied states in the tip. For a positive sample voltage (Fig. 3.5 c) the situation is reversed and electrons tunnel from the occupied states of the tip into unoccupied states of the sample. If the sample and the tip have a constant, or flat, LDOS, the tunnel current is directly proportional to the applied bias voltage giving rise to an ohmic behavior of the tunnel junction.

By assuming that the sample has the same height but a varying LDOS depending on the lateral position, schematically shown in Fig. 3.6, this simplified picture breaks down. Figure 3.6 shows schematically a scan with the tip over the sample which is perfectly flat but has a different LDOS ρ and work function Φ depending on the lateral position. In this example region 2 in the center has a smaller LDOS than the surrounding regions (1). This means that the number of states in region 2, which can contribute to the tunnel current, is reduced compared to region 1, and in order to

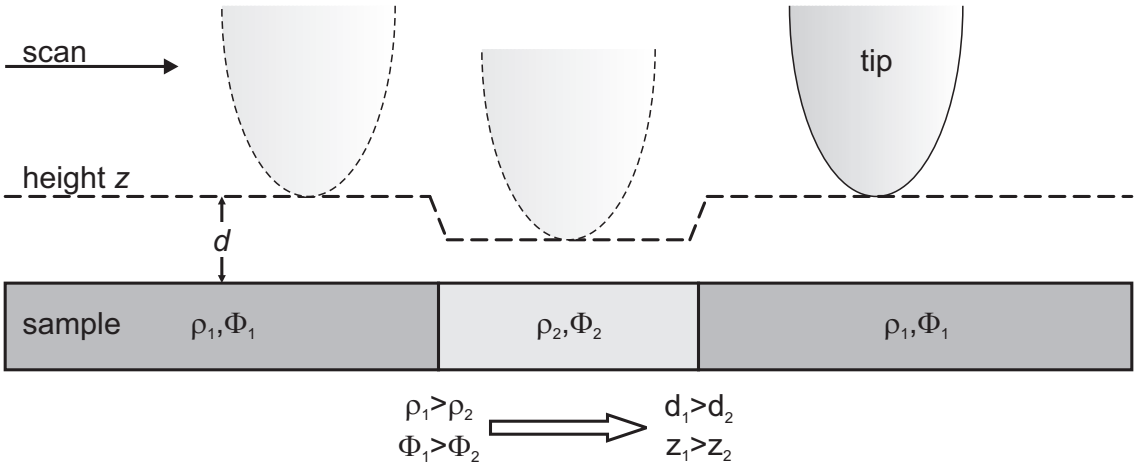

Figure 3.6: Effect of electronic properties of the sample. Even though region 1 and region 2 of the sample have the same height, the differences in the local density of states ρ and work functions Φ between the two areas lead to a different apparent height z if the STM is operated in the constant current mode.

keep the tunnel current constant the tip has to move closer to the sample. This leads to an apparent change in the tip height z even if the sample is flat. Since the tunnel current also depends on the work function of tip and sample (see Eq. 3.3), a similar effect would be observed by a locally varying work function.

Some nice examples for the contribution of the LDOS to the tunnel current are single molecules or adsorbates which sit on top of a flat metal surface. If only the sample profile would contribute to the tunnel current those adsorbates should appear as protrusions in constant current images. But some of those adsorbates appear as an indentation rather than a protrusion as e.g. CO molecules on Cu(111) [35] or single O atoms on an Fe surface [36], which means that the LDOS above the adsorbates is drastically reduced, so that the tip has to move closer to the adsorbate even if it is sitting on top of the surface (see also Ref. [37]).

In Sec. 6.2.3 I present another example of how the LDOS contributes to the tunnel current. As shown in Sec. 2.2, the spin-orbit interaction leads to a lifting of the energy degeneracy of different spin directions. This means, that the surface atoms' LDOS varies depending on how their magnetic moments arrange with respect to the atomic lattice, e.g., if the moments align along or perpendicular to the easy axis. In STM experiments this leads to the *tunneling anisotropic magnetoresistance* (TAMR). By exploiting this effect, it is possible to observe magnetic domain walls in Fe stripes on W(110) [38] and also LDOS changes on the atomic scale due to spin spiral states [15, 19].

3.4. Scanning Tunneling Spectroscopy

More information about the electronic structure of the sample system can be gained by using *scanning tunneling spectroscopy* (STS). It is obvious from Eq. 3.10 that the tunnel current is proportional to the integrated density of states of the sample. Differentiation of the expression for the tunnel current with respect to the applied voltage U leads to the *differential conductance*

$$\frac{\mathrm{d}I}{\mathrm{d}U} = \frac{4\pi e^2}{\hbar}\rho^{\mathrm{T}}(E_{\mathrm{F}}^{\mathrm{T}})\rho^{\mathrm{S}}(E_{\mathrm{F}}^{\mathrm{S}}+eU)\left|M(E_{\mathrm{F}}^{\mathrm{S}}+eU, E_{\mathrm{F}}^{\mathrm{T}})\right|. \tag{3.18}$$

This approximation is only valid in the limit of $eU \ll \Phi$, where Φ is the work function of the sample given by $\Phi = E_{\mathrm{V}} - E_{\mathrm{F}}$. Differentiating Eq. 3.14 the differential conductance in the approximation of Tersoff and Hamann is given by

$$\frac{\mathrm{d}I}{\mathrm{d}U} \propto \rho^{\mathrm{T}}\rho^{\mathrm{S}}_{\mathrm{local}}(\mathbf{R}, E_{\mathrm{F}}^{\mathrm{S}}+eU). \tag{3.19}$$

This means that the derivative of the tunnel current I with respect to the applied voltage U is directly proportional to the LDOS of the sample at the position of the tip $\mathbf{R}$ and the energy $E_{\mathrm{F}} + eU$. Thus it is possible to map the LDOS of the sample by stabilizing the tip over the position of interest, given by the spatial coordinates (x_0, y_0), at the stabilization parameters U_0 and I_0, switching off the feedback loop, and sweeping the bias voltage (*single point spectroscopy*). During the voltage sweep the tunnel current is recorded while the tip position z remains constant. The resulting $I(U)$-curve contains information about the LDOS $\rho(x_0, y_0)$ which can be derived by numerical differentiation or – more commonly used – via lock-in technique. The bias voltage is modulated by a small AC voltage U_{mod} with a typical frequency of $\nu = 2\ldots5\,\mathrm{kHz}$ and a known phase and the $\mathrm{d}I/\mathrm{d}U$-signal is measured by a lock-in amplifier. This extremely narrow band pass filters very efficiently AC voltages of different frequencies (e.g. electrical 50 Hz noise) or other random noise and often results in a much higher signal quality compared to the numerical differentiation of the $I(U)$-curve.

In contrast to the single point spectroscopy which records $\mathrm{d}I/\mathrm{d}U(U)$ at a fixed position (x_0, y_0), the $\mathrm{d}I/\mathrm{d}U$*-map* gives information about the spatial variation of the differential conductance at a fixed energy, $\mathrm{d}I/\mathrm{d}U(x, y)$. It is acquired simultaneously to the constant current image using a lock-in amplifier, which allows direct correlation of the sample topography with the map of differential conductance.

Spectroscopic data acquired in one of the two ways has to be analyzed very carefully since it does not only depend on the LDOS of the sample but also on the LDOS of the tip, see Eq. 3.19. So far the electronic structure of the tip has been assumed to be constant, see also Fig. 3.5, which is almost never the case in a real experiment.

3.5. Spin-polarized scanning tunneling microscopy

If the tunnel current flows between two magnetic electrodes, in addition to the contributions of the distance between the electrodes and their respective electronic properties it also contains information of their magnetic properties. In Fig. 3.7 the tunnel current between two ferromagnetic electrodes is shown schematically. Due to the exchange interaction the density of states of the electrodes are split into majority electrons (↑) and minority electrons (↓), which leads to a spin polarization at the Fermi energy of $P(E_\mathrm{F}) = (\rho_\uparrow(E_\mathrm{F}) - \rho_\downarrow(E_\mathrm{F}))/(\rho_\uparrow(E_\mathrm{F}) + \rho_\downarrow(E_\mathrm{F}))$. By assuming that the electron spin is conserved during the tunneling process, the ↑-electrons from the tip can only tunnel into unoccupied ↑-states in the sample; the same for the ↓-electrons. When the magnetization directions of the two electrodes are in parallel alignment (Fig. 3.7 a) the tunnel current is different compared to the antiparallel alignment (Fig. 3.7 b).

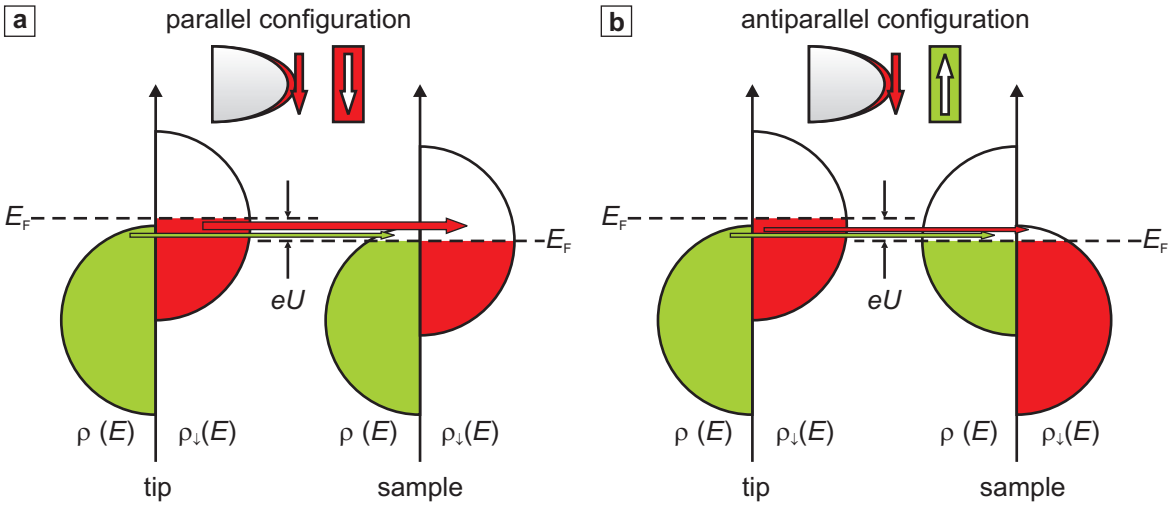

Figure 3.7: Scheme of spin-polarized scanning tunneling microscopy. **a**, For the case of parallel alignment of tip and sample magnetization electrons with the spin ↓ (↑) can tunnel from the tip to unoccupied states with the spin ↓ (↑) in the sample. **b**, Antiparallel alignment: since the number of unoccupied states in the sample with spin ↓ is reduced compared to the parallel configuration, the tunnel current between tip and sample is smaller for the same applied voltage.

M. Jullière first discovered this *spin valve effect*, or *tunneling magnetoresistance* (TMR), in planar Fe-Ge-Co tunnel junctions which showed a decreased conductance in the case of non-parallel alignment of the electrodes' magnetizations compared to the parallel case [39]. In a theoretical work, J. C. Slonczewski extended the model of tunneling in one dimension (see Sec. 3.1) by spin-polarized electrodes [40]. In the limit

of vanishing bias voltage U and free electrons the tunnel current can be expressed by

$$I = I_0[1 + P_\mathrm{T} P_\mathrm{S} \cdot \cos(\mathbf{M}_\mathrm{T}, \mathbf{M}_\mathrm{S})], \tag{3.20}$$

where I_0 is the non-polarized current, P is the polarization and $\mathbf{M}$ is the magnetization direction of the tip (T) and the sample (S), respectively. Assuming an electronically homogeneous sample and a stable tip, I_0, P_S, P_T and $\mathbf{M}_\mathrm{T}$ are constant for a given bias voltage U_0 and any change in the tunnel current I can be attributed to changes of $\mathbf{M}_\mathrm{S}$.

This cosine dependence of the tunnel current has been experimentally verified in planar Fe-Al_2O_3-Fe tunnel junctions [41], and in 1990 R. Wiesendanger *et al.* showed for the first time that the TMR can also be measured in the STM geometry [42]. Since more than 10 years, SP-STM is a well-established technique which can be used to investigate the magnetic ground state of nanostructures down to the atomic scale [43, 44]. In the past years, the technique has been extended to study also dynamics of magnetic systems like spin-flip processes [45, 46] or magnon excitation [47, 48] and it has been shown that atom manipulation with a magnetic tip is feasible [49, 50]. Only very recently SP-STM has been used to probe spin relaxations of single atoms on the time scale of nanoseconds [51].

4. Instrumental setup and preparation

Within the framework of my PhD thesis I conducted (SP-)STM measurements of Fe nanostructures on Ir surfaces. Since the STM is a very surface sensitive technique, it is crucial that the investigated sample system remains uncontaminated from adsorbates during the measurements, which can last for hours or even days. Due to the extremely small distances between the sample and the probe tip, adsorbates on the surface or in the tunnel junction can lead to measurement artifacts. In Sec. 4.4.5 I will show an example of how adsorbates affect the sample and could lead to misinterpretation of the STM measurements.

Roughly estimated, a surface is completely covered by adsorbates within 1 s in a pressure of $p \approx 10^{-6}$ mbar [52], while it remains clean for several hours at $p = 10^{-10}$ mbar. For this reason, all experiments were performed in ultra-high vacuum (UHV) conditions ($p < 10^{-10}$ mbar). In this chapter I will give an overview of the UHV chamber and the instruments, which were used for the studies of Fe nanostructures on Ir surfaces, Sec. 4.1 and 4.2, as well as the preparation of the probe tips and the investigated samples, Sec. 4.3 and 4.4.

4.1. UHV system

The measurements presented in chapters 5 and 6 were performed in the UHV system presented in Fig. 4.1. It is based on a standard UHV system from Omicron [53] (see Fig. 4.1 a) which consists of three separate UHV chambers connected by a central distribution chamber (Fig. 4.1 b shows a schematic drawing of the system). The UHV system has been augmented by an additional chamber which hosts a low-temperature STM and is shown in Fig. 4.1 c (see 4.2.2). The base pressure in all chambers during normal operation is usually $p \leq 2 \cdot 10^{-10}$ mbar. Attached to the distribution chamber is a fast entry load lock (LL) which allows to introduce new samples and tips, which can be moved from one chamber to another by an elaborate shuttle system.

One of the chambers, the preparation chamber (Prep), accommodates an electron beam heater as well as an ion sputter gun which are needed in order to clean the sample surfaces and tips (see Sec. 4.3 and Sec. 4.4). The second chamber is mainly used to deposit materials onto the clean surfaces or tips using molecular beam epitaxy (MBE) and is additionally equipped with a room temperature STM, see Sec. 4.2.1. The third chamber, the analysis chamber (Ana), is used to investigate the quality

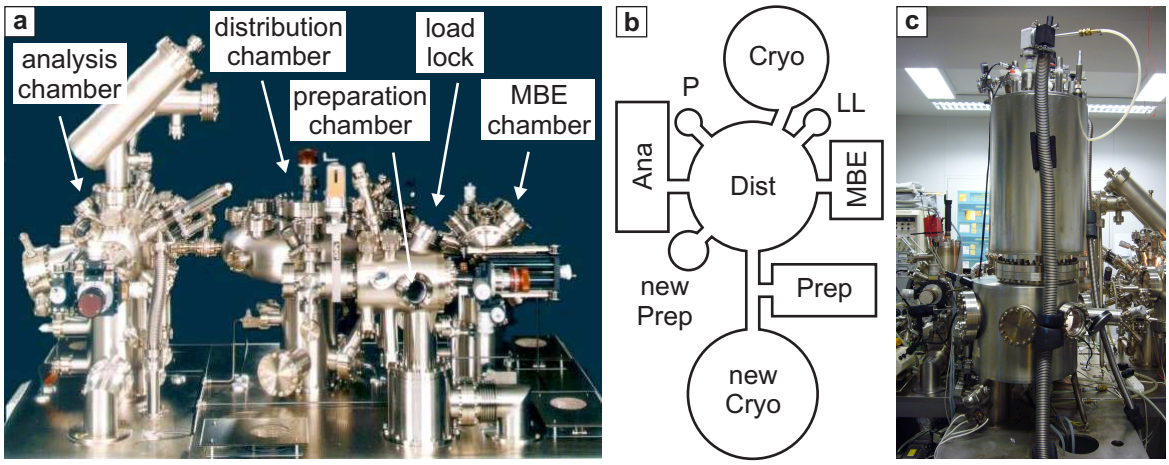

Figure 4.1: Overview of the UHV system. **a**, Photograph of the multi-chamber system as delivered by Omicron (courtesy of Omicron [53]). **b**, Schematic drawing of the system with all extensions (top view). A parking spot for tips and samples (P), an additional preparation chamber (new Prep) and two chambers for low temperature STMs (Cryo and new Cryo) have been attached to the main system shown in **a**. **c**, Photograph of the cryostat which contains the low-temperature STM presented in Sec. 4.2.2.

of our samples by the standard surface characterization methods, low energy electron diffraction (LEED) and Auger electron spectroscopy (AES). While LEED is very useful to gain insight into the symmetry of the sample surface [13, 54], AES gives information about the chemical composition of the surface [55, 56]. In addition, an STM for use at variable temperatures is installed in this chamber. As can be seen in the schematic drawing, the UHV system has been extended recently with a second preparation chamber (new Prep) as well as a second cryostat (new cryo) for (SP-)STM measurements at $T < 1\,\mathrm{K}$ and high magnetic fields ($B_{\mathrm{max}} = 9\,\mathrm{T}$).

4.2. Scanning tunneling microscopes

4.2.1. Room temperature scanning tunneling microscope

The microscope which resides in the MBE chamber (see 4.1) is a home-built STM designed by Christian Witt [57]. This STM was specifically designed to study the growth of deposited metal atoms on a surface and it allows the investigation of the very same spot of the sample at different coverages. In conventional STM designs, the sample has to be taken out of the microscope in order to deposit material onto the surface. Therefore it is basically impossible to find the same spot on the sample again after the deposition. To avoid that problem the sample stays in the sample stage of

the STM during the deposition. This is possible since the axis of the sample movement and the scanner axis include an angle of 60° (see Fig. 4.2 a) allowing not only a vertical but also a lateral movement away from the tip. With this geometry it is possible to deposit material onto the sample when it is in the deposition position without affecting the tip. Additionally the beam from the evaporator is almost parallel to the sample normal which ensures a uniform growth of material on the whole sample. The MBE chamber is equipped with four electron beam evaporators, three of them pointing at the deposition position, which allows growth studies of many different sample systems.

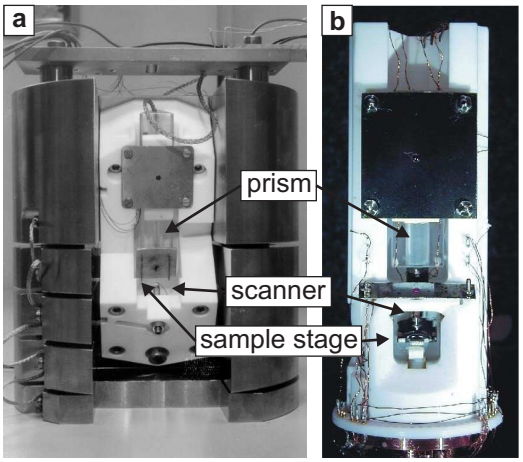

Figure 4.2: Photographs of the two STMs used for the studies in this thesis. **a**, Room-temperature STM used for growth studies, taken from Ref. [58]. **b**, Low-temperature STM for STS studies as well as SP-STM measurements.

4.2.2. Low temperature scanning tunneling microscope

The low temperature (LT-) STM shown in Fig. 4.2 b was designed and built by Dr. Oswald Pietzsch, and Dr. André Kubetzka optimized it for spin-polarized STM measurements by including a tip exchange mechanism [59, 60, 61]. It is mounted in a cryostat consisting of a reservoir for liquid helium (lHe), a reservoir for liquid nitrogen (lN_2) and a superconducting Helmholtz coil. The STM is in thermal contact with the lHe ($T \approx 4.2\,\mathrm{K}$) which is shielded by the lN_2 ($T \approx 77\,\mathrm{K}$) from radiation of the surrounding. In thermal equilibrium, the STM works at $T \approx 8\,\mathrm{K}$, which is measured in the STM directly on the sample stage. The Helmholtz coil produces a homogeneous magnetic field at the sample position which is normal to the sample surface with a strength of up to $B = 2.5\,\mathrm{T}$. Sample and tip can be exchanged using a wobble stick and are held in place by metallic springs, which also provide the thermal and electric contact. Compared to the room temperature STM, the LT-STM has the advantage of a much higher energy resolution ($k_\mathrm{B} \cdot (300\,K) \approx 25\,\mathrm{meV}$ vs. $k_\mathrm{B} \cdot (8\,K) < 1\,\mathrm{meV}$) as well as reduced thermal drift between tip and sample.

4.3. Preparation of tips for SP-STM measurements

For SP-STM measurements it is crucial to have mechanically stable and sharp tips which also provide a high spin-polarization. The tips used for the experiments presented in this work are made from 0.75 mm tungsten (W) wire and are prepared in four steps.

First, the tips are etched *ex situ* by dipping the wire into a base solution (2 M sodium hydroxide (NaOH)) and applying an AC voltage of 4 . . . 5 V. The lower part of the wire is covered with an insulating material and will be the STM tip. The wire is lowered until the insulated part is completely in the solution and the area just above the insulation is etched. This leads to a tapering of the W wire until it breaks and the lower part falls down. After carefully removing the insulation and cleaning the tip from residua of the base it is mounted in a tip holder and introduced in the UHV chamber.

The second tip preparation step consists of heating the tip inside the UHV chamber to temperatures > 2000 K using an electron beam heater. This treatment removes possible impurities and oxide layers from the tip. In the third step, the clean W tip is coated with a thin film consisting of either Fe or chromium (Cr) [43]. After the deposition of the magnetic material the coated tip is slightly heated to $T \approx 600 \ldots 700$ K to ensure a smooth film.

After these three preparation steps the tip is inserted into the STM and can be used for SP-STM measurements. A fourth preparation step, which is the *in situ* sharpening of the STM tip, might be necessary when the tip is not sharp, unstable or consists of multiple micro-tips. By approaching the tip to or even gently dipping it into the surface the foremost end of the tip can be rearranged or tip atoms can be lost. Similarly, the tip can be formed by applying voltage pulses between the tip and the sample. The outcome of such a treatment does not need to be positive, the tip can actually get worse, but by patiently repeating these procedures it is very likely that the tip will be sharp some day.

Both tip coatings – Fe and Cr – have their advantages and disadvantages and are used depending on the design of the experiment. On the one hand, tips covered with an Fe film have the advantage that their spin polarization is usually larger than the polarization of the Cr-coated tips. Additionally, it is from my experience easier to get a sharp and stable Fe-coated tip compared to the Cr-coated tips. On the other hand, the stray field of Fe-coated tips can affect a magnetic sample and thereby lead to measurement artifacts while the stray field of Cr-coated tips is (almost) negligible due to their antiferromagnetic ordering.

Depending on the investigated sample system and the experimental requirements it is not only crucial that the tip is magnetic but also its behavior in an external magnetic field becomes important. Usually, the magnetic origin of an observed SP-STM contrast is proven by applying an external magnetic field in opposite directions.

Therefore, only one of the two electrodes – tip or sample – should be influenced by the magnetic field, i.e. one of the two electrodes should be a *hard* magnet the other one a *soft* magnet.

Due to the ferromagnetic order of Fe-coated tips their magnetization direction aligns with an applied magnetic field, which makes them useful to investigate hard magnetic samples, e.g. an antiferromagnet [6], a spin spiral [15] or ferromagnets with a large anisotropy, which remain unaffected by the magnetic field. This leads to inverted SP-STM contrasts in opposite magnetic field directions, which is an ultimate proof for magnetic contrast. In a recent work it was demonstrated how an Fe-coated tip can be aligned in any direction with a vector field magnet, thereby detecting all components of a spin-spiral [5].

In order to study sample systems with a soft magnetization, e.g. small ferromagnetic structures or single atoms, it is desirable that the tip magnetization is independent of the external magnetic field. Cr-coated tips meet these demands due to their antiferromagnetic ordering and it was thereby possible to investigate e.g. field dependence of Co islands on copper (Cu) [62] or record magnetization curves of single atoms or dimers [63, 64].

While I only utilized such coated tips for the investigations presented in the following chapters, there are different preparation procedures for magnetic tips available. It has been shown, that an initially non-magnetic tip can become spin-sensitive by dipping it *in situ* into a magnetic sample [65] or by picking up a single magnetic atom [45]. In a different approach there have been several successful attempts to utilize Cr bulk tips for SP-STM studies [66, 67, 68].

4.4. Sample preparation

In this section I describe how to prepare Fe nanostructures on the two Ir surfaces. Since both sample preparations are very similar I restrict the discussion to the preparation of Fe chains on the reconstructed Ir(001) surface.

4.4.1. Preparation of Fe chains on (5×1)-reconstructed Ir(001)

The first step of the preparation of the (5×1)-reconstruction is to clean the Ir(001) surface. Since embedded carbon (C) atoms are the main contamination of an Ir single crystal, the creation of a surface without C atoms is the first preparation step. In order to eliminate the C impurities, the Ir crystal is annealed using a temperature ramp with a constant increase in temperature and a maximum temperature of 1800 K in an atmosphere of oxygen (O_2) with p_{O_2} ranging from 10^{-6} to 10^{-7} mbar. The elevated temperature leads to an increased mobility of the C impurities which can move to the surface where they react with the O_2 molecules to either CO or CO_2. Due

to the high temperature the molecules desorb from the surface and can be pumped out of the UHV chamber by a turbo molecular pump. Many successive cycles of this procedure lead to a large depletion zone below the surface which contains almost no C atoms.

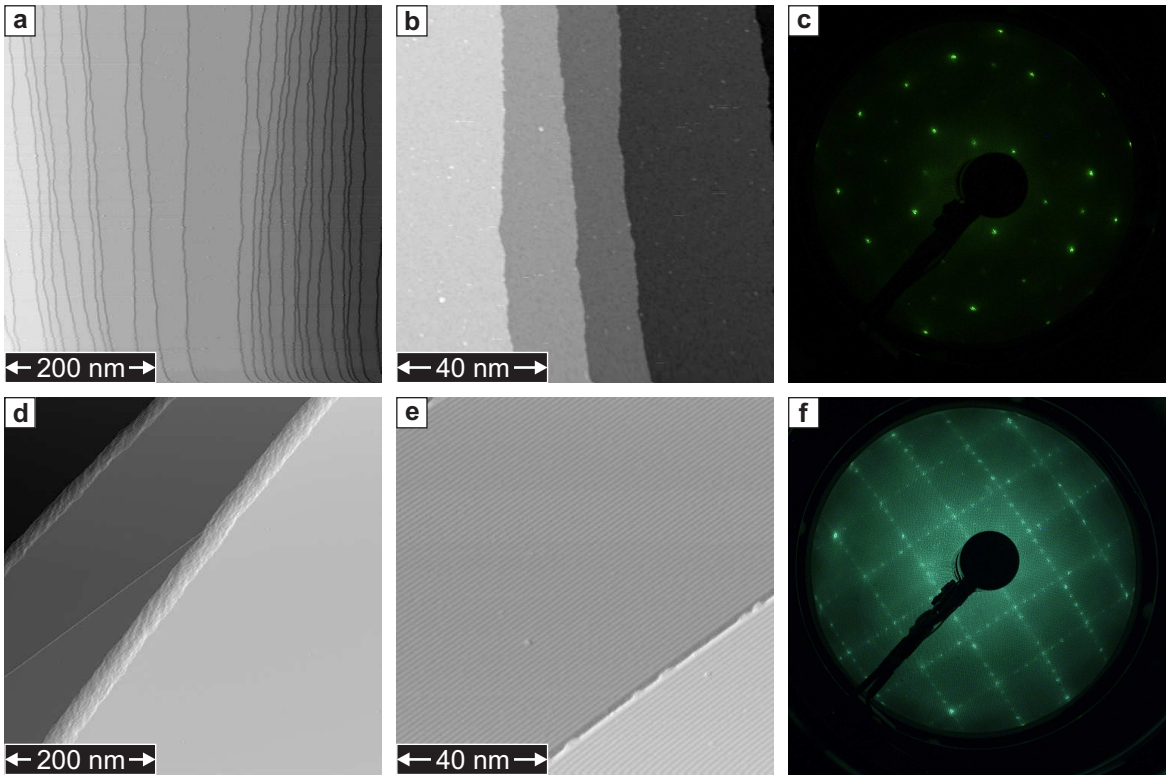

Figure 4.3: Comparison of the (1×1)-surface and the (5×1)-reconstruction of the Ir(001) surface. **a**, Overview constant current STM image ($U = -500\,\mathrm{mV}$, $I = 0.5\,\mathrm{nA}$, RT) and **b**, closer view of the unreconstructed Ir(001) surface ($U = +100\,\mathrm{mV}$, $I = 1\,\mathrm{nA}$, RT). **c**, photograph of the LEED pattern of the (1×1)-surface (electron energy: $E = 326\,\mathrm{eV}$). **d** - **f**, Similarly, STM images and LEED pattern of the (5×1)-reconstructed Ir(001) surface (**d** and **e**, $U = -800\,\mathrm{mV}$, $I = 0.4\,\mathrm{nA}$, RT; **f**, $E = 325\,\mathrm{eV}$).

After obtaining a carbon free surface, the preparation of the reconstructed surface follows a standard UHV cleaning recipe. Therefore the topmost surface layers, and the adsorbates on top of the surface, are removed by bombardment with argon (Ar) ions ($U_{\mathrm{acc}} \approx 800\,\mathrm{V}$ at $p_{\mathrm{Ar}} \approx 8 \cdot 10^{-5}\,\mathrm{mbar}$) and subsequent annealing to 1600 K to restore the surface reconstruction. If carried out properly once, the O_2-treatment does not need to be repeated every time, e.g., I did not need to repeat it for more than two years.

In Fig. 4.3 the differences between the unreconstructed surface and the (5×1)-

reconstructed surface are shown:

a and d: The unreconstructed (1×1)-surface exhibits terraces, which all have a similar width, separated by monatomic steps. In contrast, the (5×1)-surface exhibits huge terraces separated by bunches of many steps (see also Fig. 4.4).

b and e: The reconstructed surface shows a regular arrangement of trenches on the surface while the unreconstructed surface is – except for some defects or adsorbates – rather flat.

c and f: The two surfaces can also be easily distinguished by their respective LEED pattern. In addition to the spots of the (1×1)-surface, c, the reconstructed surface exhibits higher order spots in the LEED pattern reflecting the (5×1)-superstructure, f. Due to the crystal symmetry the reconstruction exhibits two rotational domains perpendicular to each other[1].

After the last preparation step, annealing to 1600 K, the surface was cooled down to room temperature before Fe atoms were deposited onto the surface with a commercially available electron beam evaporator [70]. In this setup the Fe atoms were evaporated from a high purity Fe wire with a diameter of 2 mm. The deposition rate was controlled by an integrated flux monitor, which measures the current of ionized Fe atoms. The deposition rate is in good approximation directly proportional to the detected flux current. Once calibrated, the time needed to deposit the desired amount of material can be determined very precisely.

Now the sample is prepared and can be investigated by (SP-)STM. For the preparation of a new sample one just has to repeat the steps described above. Since the Ir(001) surface tends to form alloys with deposited metal atoms quite easily (see 4.4.3) I want to emphasize that the crystal should not be heated if the deposited atoms are still on the surface. This will result in a diffusion of the metal atoms into the Ir crystal bulk, and it will be extremely difficult to obtain a clean Ir(001) surface again. Therefore, the first step to prepare a new sample should *always* be a cycle of Ar^+-etching.

4.4.2. Ir(001) surface and its reconstruction

The (001) surface of an iridium single crystal exhibits two different structures, the meta-stable unreconstructed (1×1)-surface as well as the energetically more favorable quasi-hexagonal (5×1)-reconstruction. This surface and its reconstruction have been studied to quite some extent over the last 40 years from the experimental side [69, 71, 72] as well as from the theoretical side [69, 73]. The interest in this surface stems from

[1] While the (5×1)-reconstruction is energetically favorable compared to the unreconstructed surface, it can be lifted by annealing the surface in an atmosphere of hydrogen (H_2), giving rise to a clean but metastable (1×1)-surface [69].

the fact that the exact form of the reconstruction was under debate for a long time, but lately the reconstruction draws attention since it is a nice template for growth of self-organized one-dimensional nanostructures [74, 75].

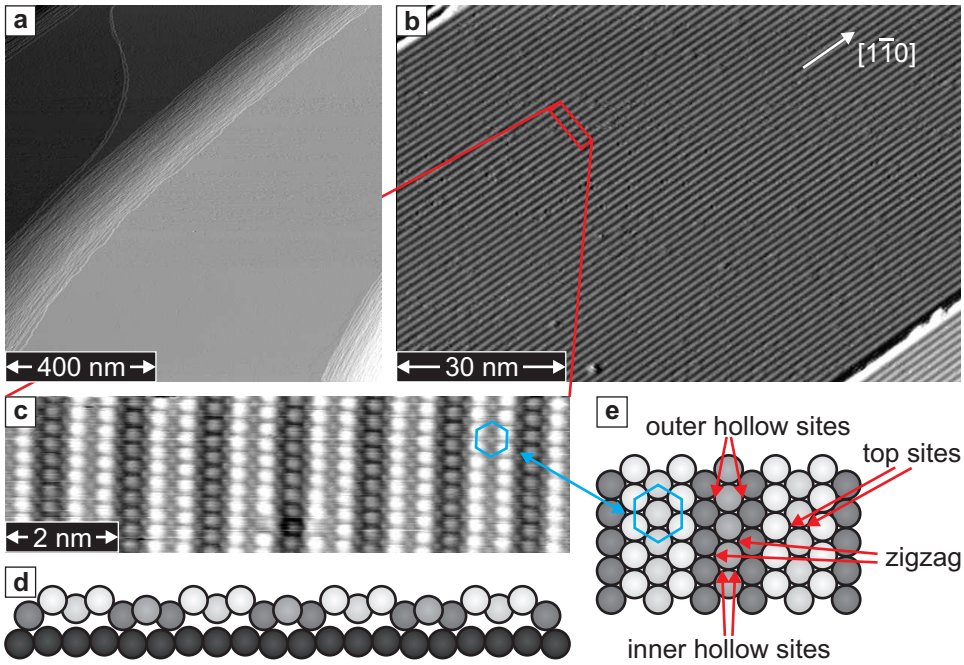

Figure 4.4: The (5×1)-reconstruction of the Ir(001) surface. **a**, Large terraces on the μm scale are separated by step bunches (measurement parameters: $U = -500\,\mathrm{mV}$, $I = 1\,\mathrm{nA}$, RT). **b**, STM image showing the trenches and hills of the reconstruction running along the [1$\bar{1}$0]-direction ($U = -800\,\mathrm{mV}$, $I = 0.4\,\mathrm{nA}$, RT). **c**, Atomically resolved STM image of the reconstruction ($U = -2\,\mathrm{mV}$, $I = 40\,\mathrm{nA}$, RT). **d** and **e**, Top view and side view of the corresponding ball model, respectively.

As it is shown in Fig. 4.4 a, the (5×1)-reconstructed Ir(001) surface exhibits huge terraces (with a width of up to 1 μm) which are separated by bunches of monatomic steps. A closer look to one of the terraces shows a regular arrangement of parallel trenches running along a ⟨1$\bar{1}$0⟩-direction with a distance between two adjacent trenches of 1.35 nm. The apparent depth of the trenches in the STM image in Fig. 4.4 b is ≈ 50 pm which is in excellent agreement with LEED measurements and DFT calculations [69, 76, 77]. This buckling of the topmost surface layer is due to an additional amount of 20 % more atoms compared to the underlying layers. In an STM image with true atomic resolution the quasi-hexagonal arrangement of the atoms in the topmost layer (see blue hexagon in Fig. 4.4 c) as well as the internal structure of the reconstruction becomes visible. The hills and the trenches consist of three rows of atoms, each, and the row of atoms in the center of the trench (hill) is sitting slightly higher

(lower) than the two neighboring rows (see also side and top view of the ball model in Fig. 4.4 d and e).

This arrangement of the Ir atoms in the surface reconstruction leads to several different adsorption sites which are marked in Fig. 4.4 e. The adsorption sites in the trench of the reconstruction are labeled with respect to the distance to the center row of the trench (*inner* and *outer hollow site*). The mixture of the two sites is entitled *zigzag* and the adsorption sites on the hill of the reconstruction are named *top sites*.

4.4.3. Growth of Fe on reconstructed Ir(001)

Due to its trenches the reconstructed Ir(001) surface is an ideal template for the self-organized growth of one-dimensional nanostructures. As it has been shown before [75, 78], the growth of Fe on the reconstructed surface can be divided into four regimes:

1. If the coverage of Fe atoms does not exceed 20 to 25 % of an atomic layer (also monolayer (ML)), Fe grows almost solely in the trenches of the reconstruction forming bi-atomic chains (see Fig. 4.5 a).

2. For coverages between 0.25 and 0.8 ML the deposited Fe atoms start to lift the reconstruction and a more or less ordered surface alloy is formed. The beginning of this alloying process can be seen in Fig. 4.5 a (marked by the arrows). At this stage the alloy is rather disordered while with increasing coverage a regular (5×1)-superstructure develops [75].

3. The second and third atomic layers grow in the Frank-van-der-Merwe mode forming rectangular islands with the edges along the $\langle 1\bar{1}0\rangle$-directions. Even though the reconstruction is lifted, it still influences the growth of these islands. All of them grow with the long edge parallel to the direction of the former trenches [78][2].

4. Also the fourth atomic layer grows in the layer-by-layer mode, but the rectangular islands show no preferred direction of growth as the islands of the second and third layer [78].

In this work I concentrated on the Fe chains which form in the first growth stage and studied their structural, electronic and magnetic properties. Since the structural configuration of the Fe chains is not clear from previous experimental and theoretical publications [75, 76, 77, 81], it is necessary to determine the favorable adsorption sites of the Fe atoms. Figure 4.5 a shows an overview STM image of the reconstructed Ir(001) surface covered by ≈ 0.15 ML of Fe. In this STM image all chains but one,

[2] More information about the growth of 3*d*-transition metals on the different Ir(001) surfaces can be found in an overview article by K. Heinz and L. Hammer [79] and in the PhD thesis of A. Klein [80].

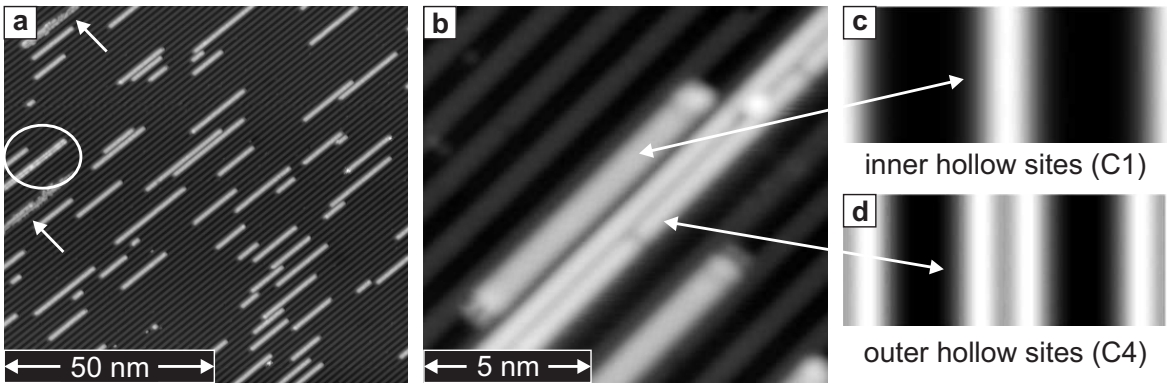

Figure 4.5: Growth of Fe on Ir(001) in the submonolayer regime. **a**, Overview constant current STM of Ir(001) covered by ≈ 0.15 ML of Fe ($U = +50$ mV, $I = 0.2$ nA, $T = 8$ K). All chains but one (marked by the circle) appear similar and only differ in height. **b**, Constant current STM image of two Fe chains grown in the inner and outer hollow site configuration, respectively ($U = +20$ mV, $I = 5$ nA, $T = 8$ K). **c** and **d**, Simulated STM images, taken from Ref. [77], of chains in the inner and outer hollow site, respectively.

which is marked by the circle, appear as a single strand, indicating that the Fe prefers only one of the possible adsorption sites. In Fig. 4.5 b a high resolution STM image of these two types of chains shows that the one rarely observed consists of two parallel strands which are well separated in the STM image.

In addition to the four adsorption sites shown in Fig. 4.4 e a fifth possibility (DEC), where the Fe atoms partially lift the reconstructed Ir surface, was proposed in Ref. [81]. From these five possible configurations we can exclude three structures by simple arguments: The adsorption position on top of the hill of the reconstruction, which is denoted as top sites in Fig. 4.4 e, does not occur, since STM images clearly show that the chains are located in the trenches of the reconstruction. Also the structural configuration denoted as DEC in Ref. [81] can be excluded, since it is known that a restructuring of the surface from the quasi-hexagonal (5×1)-phase to the quadratic (1×1)-phase has a rather large activation energy and once a (1×1)-patch has formed large parts of the reconstruction are lifted [75]. This process leads to an immediate intermixing of the deposited Fe atoms with the Ir surface atoms and surface alloy formation as it can be seen in Fig. 4.5 a (marked with the red arrows). The third structural configuration which we can directly exclude is the formation of zigzag chains (see Fig. 4.4 e). Such a structure would be asymmetric with respect to the trench and therefore it should be easily distinguishable in the STM images[3].

This leaves us with two possible structural configurations which are the inner and outer hollow sites in the trench (see Fig. 4.4 e). From Refs. [77, 81] it becomes evident

[3]Very rarely some parts of an Fe chain grow in the zigzag configuration as can be seen on p. 49.

that those two configurations are very close in their total energy which could make it possible to observe both structures at the same time. Comparing the STM image in Fig. 4.5 b to simulated STM images for the inner and outer hollow site structural configuration (see Fig. 4.5 c and d) we find a nice agreement and conclude that almost all of the observed chains are in the inner hollow site and only very rarely the Fe atoms grow in the outer hollow sites[4].

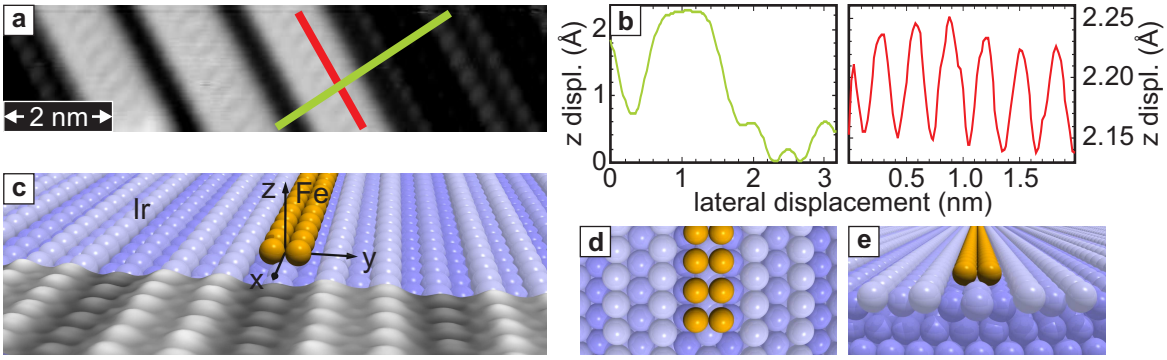

Figure 4.6: Atomic resolution of the Fe chains. **a**, Constant current STM image of three Fe chains and **b**, the profiles corresponding to the red and green line in **a**, respectively ($U = -2\,\mathrm{mV}$, $I = 40\,\mathrm{nA}$, $T = 8\,\mathrm{K}$). **c**, Ball model of an Fe chain on Ir(001) superimposed with the atomically resolved STM image from Fig. 4.4 c. **d** and **e**, Top and side view of the ball model with the Fe chains residing in the inner hollow site, respectively.

Further evidence for the inner hollow site as the preferred adsorption site for the Fe atoms is shown in an atomically resolved STM image in Fig. 4.6 a. While atomic resolution can be achieved along the chain axis (red line profile in Fig. 4.6 b), it has not been possible to resolve the two neighboring atoms perpendicular to the chain axis, see green line profile in Fig. 4.6 b. A ball model illustrating the structural configuration of these Fe chains is shown in different perspectives in Fig. 4.5 c - e.

4.4.4. Electronic properties of the Fe chains

During my diploma thesis [78] I studied not only the growth of Fe on the Ir(001) surface but also the electronic properties of the bi-atomic Fe chains which I will briefly present in this section. Figure 4.7 a and b show a constant current STM image of a typical sample area and the simultaneously acquired $\mathrm{d}I/\mathrm{d}U$-map, respectively. Most strikingly, the ends of the chains appear much darker in the $\mathrm{d}I/\mathrm{d}U$-map compared to the chain center. Since the $\mathrm{d}I/\mathrm{d}U$-signal is proportional to the LDOS (see Sec. 3.4) this is evidence that – at this particular energy – the LDOS of the chain ends is smaller than

[4]The abbreviations *C1* and *C4* for the inner and outer hollow site growth, respectively, stem from Ref. [76] and were also used in the following theoretical papers [77, 81].

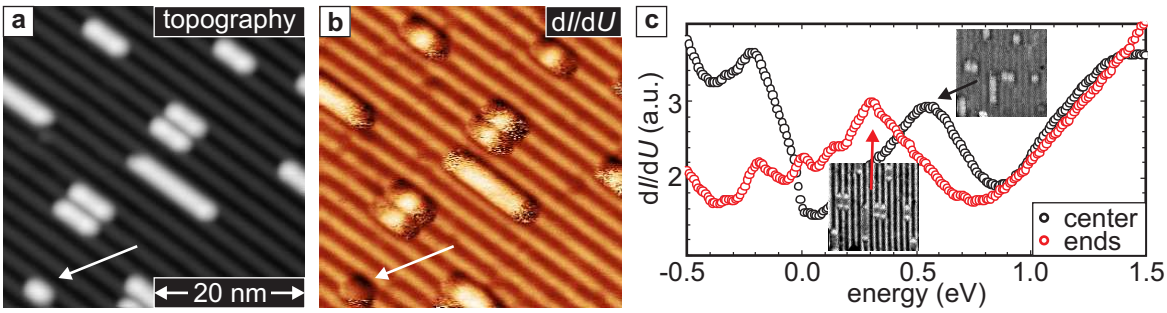

Figure 4.7: Electronic properties of Fe chains on the Ir(001) surface. **a** and **b**, Constant current STM image and the simultaneously acquired $\mathrm{d}I/\mathrm{d}U$-map of a typical sample area, respectively ($U = +500\,\mathrm{mV}$, $I = 1\,\mathrm{nA}$, $U_{\mathrm{mod}} = 20\,\mathrm{mV}$, $T = 13\,\mathrm{K}$). **c**, Spectra taken at the chain centers (black dots) and the chain ends (red dots) ($U_{\mathrm{stab}} = +1500\,\mathrm{mV}$, $I_{\mathrm{set}} = 1\,\mathrm{nA}$, $U_{\mathrm{mod}} = 15\,\mathrm{mV}$, $T = 13\,\mathrm{K}$). The insets show slices from the spectroscopic field for $U = 300\,\mathrm{mV}$ and $U = 553\,\mathrm{mV}$, respectively.

the LDOS of the chain center, meaning that the Fe chains develop an *end state* similar to Ref. [82], which can be regarded as the zero-dimensional analog to the surface state of bulk material. Furthermore, the LDOS seems to be independent of the chain length since all of the chains displayed in Fig. 4.7 b show the same contrast in their center as well as at their ends. To further investigate this intriguing difference between the ends and the center of the chains, I recorded a full spectroscopic field at this sample spot resulting in a three-dimensional data cube of the spatially and energetically resolved LDOS. This spectroscopic field confirms the independence of the LDOS from the chain length and Fig. 4.7 c shows exemplarily spectra of the chain center (black dots) and the chain ends (red dots) averaged over several chains in Fig. 4.7 a. The insets in Fig. 4.7 c show two slices of the spectroscopic field for $U = 300\,\mathrm{mV}$ and $U = 553\,\mathrm{mV}$, respectively, further illustrating the occurrence of end states in the Fe chains.

Closer examination of the $\mathrm{d}I/\mathrm{d}U$-map in Fig. 4.7 b reveals that the extremely short chain in the bottom left (marked by the white arrow) which is only $\approx 1\,\mathrm{nm}$ long, corresponding to ≈ 8 atoms, does not show the characteristics of a chain center, but only consists of ends. This means, that the observed end states are not confined to the last pair of atoms of the chain but are extended over two to three atomic distances into the chain.

Apart from the variance at the chain ends, the LDOS does not vary for chains of different lengths, see Fig. 4.7 b, and shows no modulation along the chain axis for any bias voltage applied during these investigations. This is particularly important with regard to the interpretation of the spin-resolved results presented in Sec. 5.2.

4.4.5. Sample quality and effects of contaminations

After the characterization of the growth (Sec. 4.4.3) and the electronic properties (Sec. 4.4.4) of the Fe chains I want to discuss effects due to contaminations, which can be easily misinterpreted as magnetic structure related signatures.

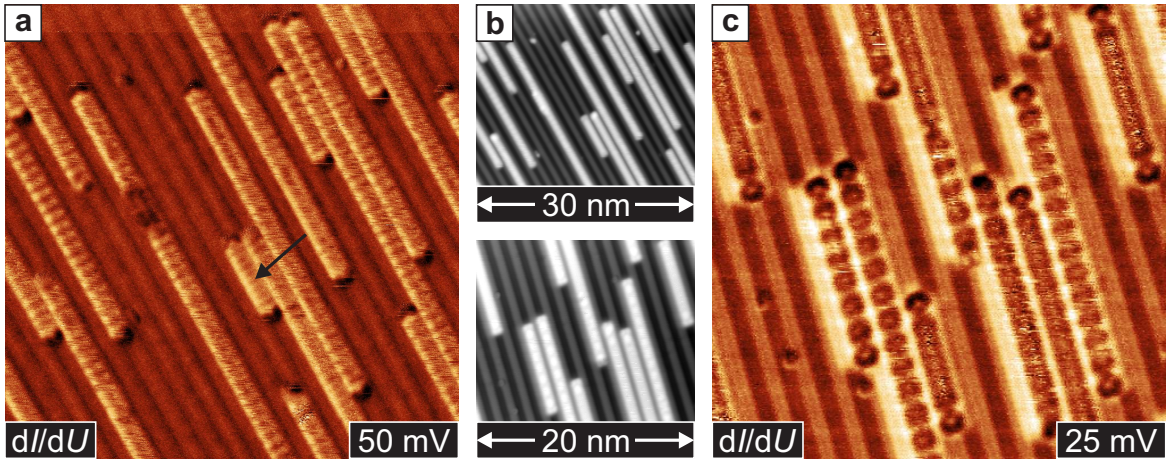

Figure 4.8: Fe chains displaying different periodic LDOS modulations. **a**, $\mathrm{d}I/\mathrm{d}U$-map, corresponding to the upper constant current image in **b**, with (almost) all Fe chains exhibiting a three atom periodicity ($I = 0.2\,\mathrm{nA}$, $U_{\mathrm{mod}} = 4\,\mathrm{mV}$, $T = 13\,\mathrm{K}$). **c**, $\mathrm{d}I/\mathrm{d}U$-map, simultaneously acquired with the lower constant current image in **b**, of Fe chains with a four atom periodicity ($I = 0.2\,\mathrm{nA}$, $U_{\mathrm{mod}} = 6\,\mathrm{mV}$, $T = 13\,\mathrm{K}$). Note that **a** and **c** show images of different preparations.

As shown in the previous section, the LDOS of the Fe chains is homogeneous along the chain axis for bias voltages $U > 300\,\mathrm{mV}$. While this is also true for most of the chains imaged at low voltages ($U \leq 100\,\mathrm{mV}$), for some preparations the chains exhibit periodic LDOS modulations in the low bias voltage regime. Figure 4.8 a and c show exemplarily $\mathrm{d}I/\mathrm{d}U$-maps of two different sample preparations acquired at bias voltages close to the Fermi level, and Fig. 4.8 b shows the respective constant current images. All of the Fe chains in those two images show modulations along the chain axes in the $\mathrm{d}I/\mathrm{d}U$-maps, which have periodicities of either three (4.8 a) or four (4.8 c) atomic distances. In very rare cases a modulation with a periodicity of just two atomic distances can be observed, see the chain marked by an arrow in Fig. 4.8 a.

As I will show in this section, these modulations are caused by contamination of the chains with adsorbates, most probably hydrogen. The observation of the modulations in only some of the sample preparations is a first indication that the periodic patterns are not due to the intrinsic electronic or magnetic structure of the chains. In most cases the chains just do not show any modulation, while the sample preparation was identical for all measurements (see Sec. 4.4). Further evidence for adsorbates as the cause for

the periodic modulations is shown in Fig. 4.9, which displays how the sample changes its appearance in STM images over time. I prepared a typical sample of Fe chains on

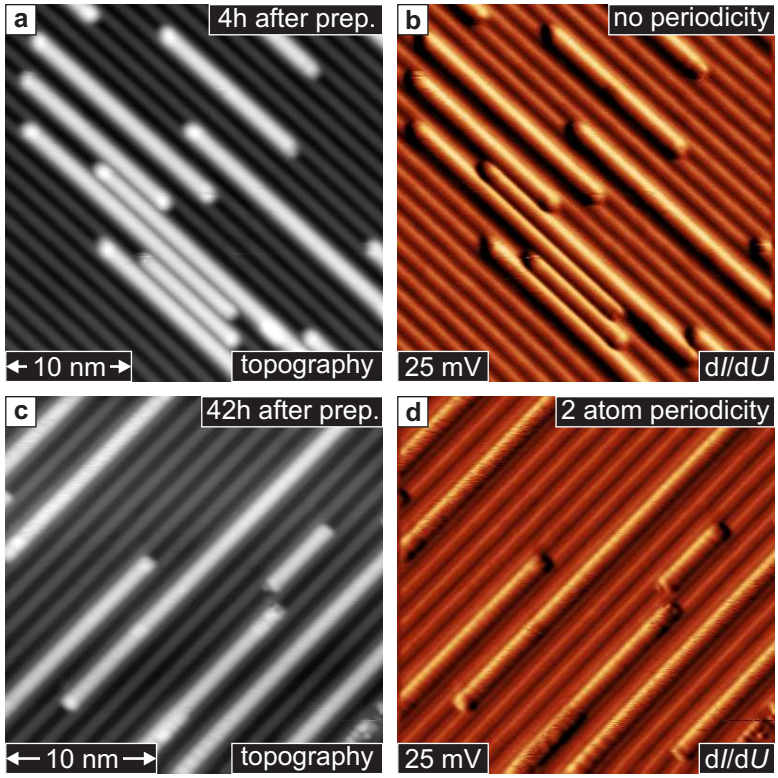

Figure 4.9: Time evolution of the sample system at low temperatures. **a** and **b**, Constant current image and the simultaneously acquired $\mathrm{d}I/\mathrm{d}U$-map of the sample four hours after the preparation. **c** and **d**, Images of the same sample but 38 h later (for all images: $I = 5\,\mathrm{nA}$, $U_{\mathrm{mod}} = 5\,\mathrm{mV}$, $T = 8\,\mathrm{K}$).

(5×1)-reconstructed Ir(001) and studied if the time, which the sample resides in the cryostat, has an effect on the appearance of the Fe chains. In Fig. 4.9 a, a constant current STM image of the sample is shown four hours after the insertion into the low temperature microscope. All of the chains look featureless in the topography channel as well as in the $\mathrm{d}I/\mathrm{d}U$-map, see Fig. 4.9 b. The very same sample, only 38 hours later, exhibits periodic modulations along the chain axes with different periodicities, see Fig. 4.9 c and d, which is a strong indication that the Fe chains getter a significant amount of adsorbates even at cryogenic temperatures. Since H_2 is the most abundant molecule in UHV, it is likely that the modulations are caused by adsorbed hydrogen atoms.

I further studied the voltage dependence of the adsorbate induced modulations to be able to distinguish them from periodic patterns due to complex magnetic structures

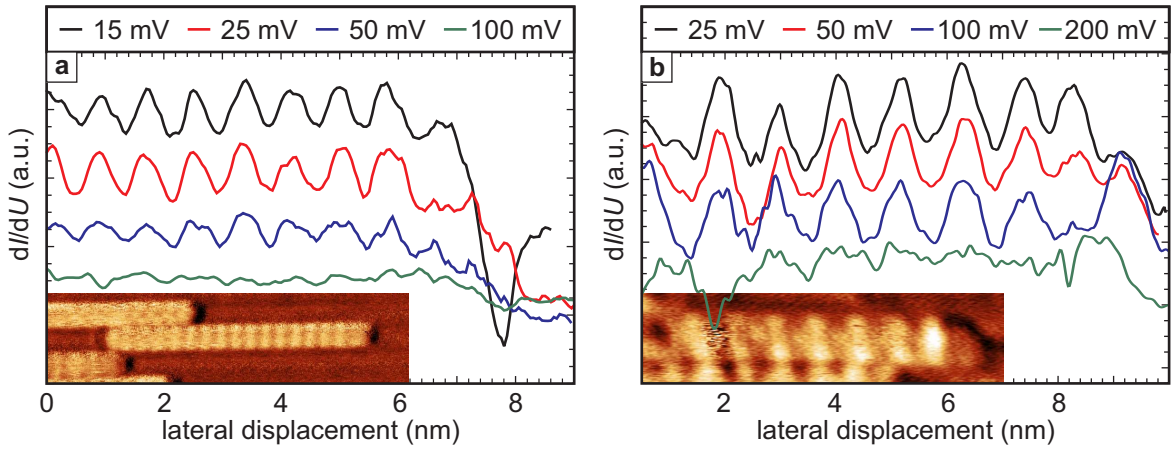

Figure 4.10: Energy dependence of the periodic modulations. **a** and **b**, Line profiles of a chain with periodicities of three and four atomic distances, respectively, taken from $\mathrm{d}I/\mathrm{d}U$-maps at different voltages. The insets show $\mathrm{d}I/\mathrm{d}U$-maps of the respective chain (**a**, $U = 15\,\mathrm{mV}$, $I = 0.2\,\mathrm{nA}$, $U_{\mathrm{mod}} = 4\,\mathrm{mV}$, $T = 13\,\mathrm{K}$; **b**, $U = 25\,\mathrm{mV}$, $I = 0.2\,\mathrm{nA}$, $U_{\mathrm{mod}} = 4\,\mathrm{mV}$, $T = 13\,\mathrm{K}$).

which can be seen in SP-STM measurements [15]. Figure 4.10 a shows line profiles at different bias voltages of a chain exhibiting a modulation with three atom periodicity (see inset). The amplitude of the periodic pattern, which is very pronounced at energies close to the Fermi level (black line), becomes smaller for larger energies, until it vanishes at bias voltages $U \geq 100\,\mathrm{mV}$. Similarly, in Fig. 4.10 b the energy dependence for a chain with the four atom periodicity is shown. While the general trend is the same as for the chains with a periodicity of three atoms – weaker contrast for higher voltages – the modulation is still quite pronounced at $U = 100\,\mathrm{mV}$ (blue line) and vanishes for voltages $U > 200\,\mathrm{mV}$[5]. In contrast to this distinct dependence of the bias voltage, the appearance of the periodic pattern does not change much with increasing tunnel current.

On closer examination, the periodicity of three atomic distances, shown in the inset of Fig. 4.10 a, seems to jump at times from one scan line to the next. In order to investigate those jumps of the periodic pattern, the measurement mode was switched from scanning a whole frame to scanning along a line on top of a chain. Though this kind of measurement requires very stable tunneling conditions, meaning no thermal drift or scanner creep, it increases the time-resolution significantly. While it takes around 5 minutes to scan a frame, which leads to a sampling rate of $\approx 0.003\,\mathrm{Hz}$, a line scan just takes $\approx 1/4$ seconds or a rate of 4 Hz, meaning that the time-resolution regarding

[5] One-dimensional quantum well states, which can lead to periodic modulations in STM images [83, 84], can be ruled out from these measurements since the periodicities change neither with the applied bias voltage nor with the chain length.

the chain is increased by three orders of magnitude. Additionally this method has the advantage that almost all recorded data is of interest – on top of a chain – while around 90 % of a frame scan is on the bare Ir surface.

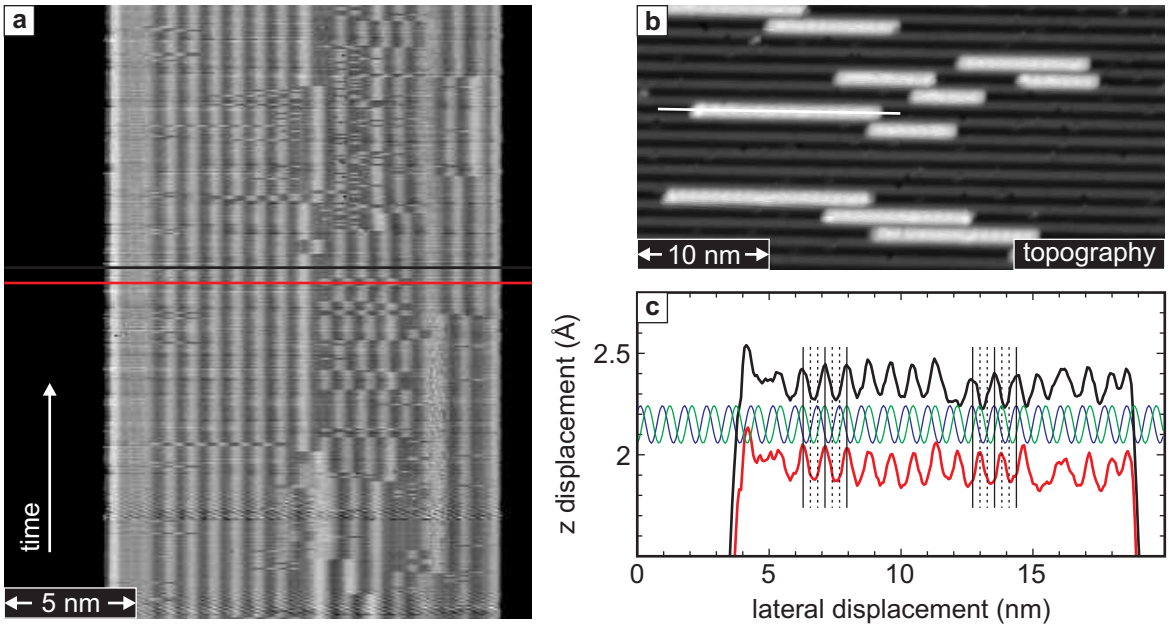

Figure 4.11: Time-resolved measurements on top of an Fe chain. **a**, Constant current waterfall plot of a single chain with the x-axis being along the white line in **b** and the y-axis as the time (**a**, $U = +5\,\mathrm{mV}$, $I = 0.5\,\mathrm{nA}$, $T = 8\,\mathrm{K}$; **b**, $U = +50\,\mathrm{mV}$, $I = 0.2\,\mathrm{nA}$, $T = 8\,\mathrm{K}$). **c** Profiles along the two lines in **a** are shown together with two cosine fits (blue and green) to the modulation of the black line. Note, that the red line is offset with respect to the black line for better visibility.

A typical measurement is shown in a waterfall plot in Fig. 4.11 a. The Fe chain, which is marked by the white line in Fig. 4.11 b, lies parallel to the fast scan direction (horizontal) and the vertical axis is the time evolution of the chain profile. This image is recorded with an applied bias voltage of 5 mV and the modulation (with a periodicity of three atomic distances) is clearly visible on the left as well as on right end of the chain while a brighter region is visible in the center of the chain. The black line in Figure 4.11 c shows a line profile along the black line in Fig. 4.11 a with a modulation amplitude on the order of 15 to 20 pm, while the blue and green line represent cosine fits to the modulation. The vertical lines reflect the atomic positions[6] and it can be

[6]The atomic positions are assumed in a way that an atom is below one maximum of the modulation, but it could very well be below a minimum since we do not know the exact adsorption position of the hydrogen atoms. Fortunately, this uncertainty does not make the following conclusions less valid.

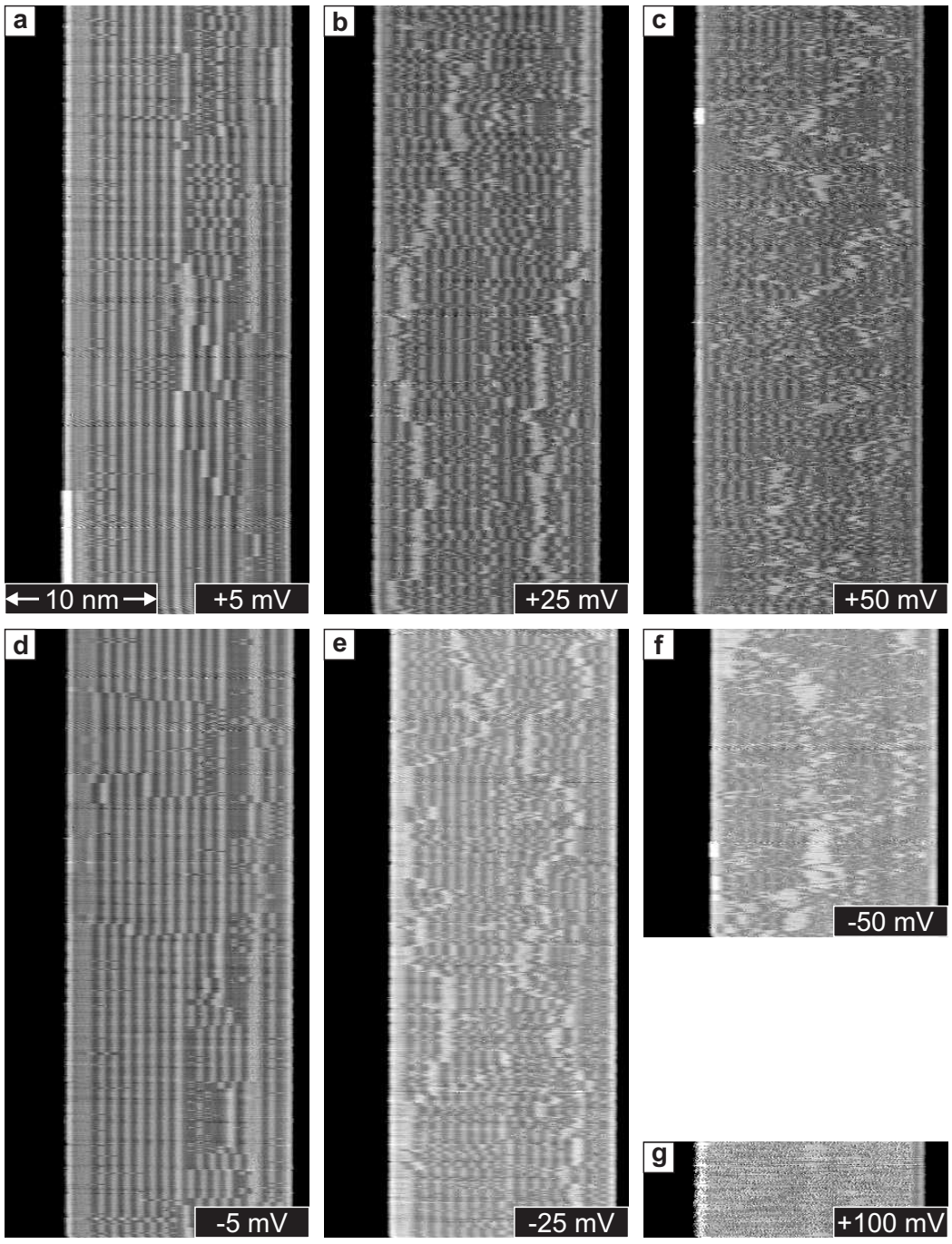

Figure 4.12: Time evolution of the same Fe chain as in Fig. 4.11 a for different voltages. The bias voltages are displayed in the lower right corner of each STM image ($I = 0.2\,\mathrm{nA}$, $T = 8\,\mathrm{K}$). The switching rate increases with increasing bias voltage.

seen that the two cosine fits exhibit a phase shift of exactly one atomic distance. This means that the bright area in the chain center acts as some kind of domain boundary which separates the two phase domains.

As it can also be seen in Fig. 4.11 a, in rare cases jumps of the modulation occur from one line to the next. Comparison of two adjacent scans showing a jump, see the black and red line profiles in Fig. 4.11 c, reveals that the modulation shifts by one atomic distance to the left or right. Since the atoms of the Fe chain act as a periodic potential for the adsorbates, leading to energetically preferred adsorption positions in atomic distances, no jumps of smaller distance can be observed. These shifts could be explained by an excitation of the periodic adsorbate structure due to interaction with the tunneling electrons from the tip.

This explanation is corroborated by line mode measurements at different tunneling parameters shown in Fig. 4.12. In these measurements the absolute value of the bias voltage is increased from left to right and it can be clearly seen that the switching rate of the modulation increases with increasing voltage until the switching is too fast to be resolved in the line scan mode for a bias voltage of $U = 100\,\mathrm{mV}$.

In summary, I have shown that adsorbates can form periodic patterns on top of the Fe chains and can be imaged using STM. Depending on the amount of adsorbates the modulations in the constant current images as well as the $\mathrm{d}I/\mathrm{d}U$-maps have periodicities of four, three or two atomic distances along the Fe chains axes. These periodic modulations can be excited by the tunneling electrons to shift laterally, which leads to a vanishing contrast for larger bias voltages $U > 100\,\mathrm{mV}$. All the measurements presented in this section are important to judge if the sample is really clean and to understand and interpret the SP-STM measurements presented in Ch. 5.

Even though I concentrated on studying the magnetic properties of uncontaminated chains, the chains with adsorbates on top could be also interesting to investigate with spin-polarized STM. In a theoretical work Vukajlovic *et al.* studied the magnetic structure of single Fe chains on the unreconstructed Ir(001) surface and the influence of hydrogen on top of these chains [85]. In their work the energy difference between the ferromagnetic and antiferromagnetic state in dependence of the hydrogen coverage is calculated. Interestingly, the Fe chains couple AFM along the chain axis when no hydrogen is present, and become FM when they are covered with hydrogen. Analogous, also the magnetic structure of the bi-atomic Fe chains on the reconstructed Ir(001) surface could be influenced by the adsorbates.

5. Magnetism of iron chains on iridium(001)

5.1. Magnetism in atomic chains

5.1.1. What is special about one-dimensional magnetism?

In the 1960's, N. D. Mermin and H. Wagner unambiguously proved that in the limit of the Heisenberg model there is no long-range magnetic order in one- and two-dimensional systems at a finite temperature T [86]. By introducing MAE, which leads to the Ising model in the limit of large K, long-range magnetic order can be found in a two-dimensional magnetic system at sufficiently low T, as it has been shown in numerous SP-STM measurements, e.g. [87, 6]. In contrast, even in the Ising model one-dimensional structures develop no long-range magnetic order at $T \neq 0\,\mathrm{K}$. Any system tries to minimize its free energy

$$F(T) = E - T \cdot S, \tag{5.1}$$

which is a competition between the energy E and the entropy S. In the limit of low temperatures, $F(0\,\mathrm{K}) = E$ meaning that the system tends to its magnetic ground state, while for high temperatures $F(T) \approx -T \cdot S$, which leads to disorder since this maximizes S. In the one-dimensional Ising model the energy for a chain of N atoms with their spins S_n^z is given by $E = -2J \sum_{i=1}^{N} S_i^z S_{i+1}^z$, and assuming FM order ($J > 0$) the ground state energy is $E_0 = -JN/2$ for $S^z = \pm 1/2$. By introducing a domain wall, one bond of the chain becomes AFM and the system loses the energy of $\Delta E = J$. This is accompanied by a gain in entropy of $\Delta S = k_\mathrm{B} \ln N$. For sufficiently large systems, i.e. in the thermodynamical limit, the entropy gain outweighs the loss in energy for *all* $T \neq 0\,\mathrm{K}$ driving the system into a magnetically disordered state. However, this also means that for extremely short chains (small N), with a length L smaller than the magnetization correlation length $\xi(T)$, the competition between E and S is won by the energy leading to a mono-domain state at finite temperatures.

Due to the lack of long-range magnetic order, the main interest in spin chains is not due to their ground state but rather their excitations. For instance, it has been shown that the excitations of an AFM Heisenberg chain with $S = 1/2$, called *spinons*, show a gapless excitation spectrum, meaning that excitations with an arbitrary small

excitation energy exist [88, 89]. A gap between the ground state and the first excited state can be created by the *spin-Peierls distortion*, which is a periodical pairing of two neighboring spins [90, 91]. This lattice distortion causes two different exchange constants $J \pm \Delta J$ which corresponds to the formation of singlet pairs with $S = 0$, a nonmagnetic ground state with an energy gap to the excited triplet state. The loss in energy due to the lattice distortion is overcompensated by the gain in magnetic energy[1].

F. D. M. Haldane proposed that, in contrast to the gapless excitations of half integer spin chains, chains with integer spins have a gap in their excitation spectra due to complex, nonlinear quantum fluctuations [94]. Although AFM Heisenberg spin chains with $S = 1$, often called *Haldane chain*, have been subject of many theoretical works [95, 96], an exact solution of those chains is still lacking [97]. Haldane's conjecture is supported by inelastic neutron scattering experiments on inorganic materials which incorporate chains of nickel (Ni) ions ($S = 1$), e.g. $CsNiCl_3$ [98].

Truly one-dimensional magnetic systems remain a theoretical concept which can be best approximated by magnetic chains in bulk systems with a very weak interchain coupling [98, 99]. Since those systems are not accessible by surface sensitive techniques as SP-STM, atomic chains deposited onto surfaces became a focal point of recent research.

5.1.2. Magnetic chains on surfaces

In general there are two possible ways to prepare atomic chains on surfaces. By choosing an adequate substrate, atoms deposited onto this surface can form one-dimensional structures due to self-organization. It has been shown that this approach works very well on semiconductor surfaces [82, 100, 101], and also on stepped or reconstructed metal surfaces [102, 103]. While this preparation procedure is very fast and allows to grow many chains simultaneously, it is not possible to control the length of the chains. Due to the vast number of chains on the surface, this preparation procedure is ideally suited for investigations using spatially averaging methods as XMCD as well as local probe techniques as STM.

The second possibility is the manipulation of single atoms on a surface with the STM tip. The feasibility of this method has also been demonstrated on numerous

[1] The name of the distortion reflects the similarity to the *Peierls distortion*, which describes a metal-insulator transition due to the rearrangement of the lattice. The energy costs for the change of the atomic position is more than compensated by the gain in electron energy due to a new band structure with a gap at the Fermi energy. Rudolf Peierls first described the effect in the 1930's in a solid-state textbook, but did not publish his results. Ironically, the first experimental evidence for a Peierls distortion and the resulting transition to an *insulating* state was found in crystals of polymer-like molecules (TTF-TNCQ), which were expected to become *superconducting* at low temperatures [92, 93].

metal surfaces [104, 83] as well as on thin insulating layers [105]. Artificial chains of well-defined length can be constructed upon employing atom manipulation, which allows the detailed investigation of size dependent effects. However, the preparation of a single chain is already very time consuming and it can only be studied using STM.

While the structural and electronic properties of atomic chains on surfaces have been studied to quite some extent, to my knowledge there are only two experimental investigations of the magnetic properties, which are also good examples for the two aforementioned preparation methods. Co atoms deposited on a vicinal platinum (Pt) surface form self-organized chains at the step edges of the substrate [106]. It has been shown by XMCD magnetization curves, that these Co atoms couple ferromagnetically along the chain axis and for $T < 10\,\mathrm{K}$ a remanent magnetization with a relaxation time of $\tau \geq 100\,\mathrm{s}$ was detected. Due to a strong hybridization with the Pt substrate, the Co chains lack the quantum mechanical behavior introduced in the previous section and can be described within a classical model.

On the other hand, up to 10 atoms long Mn chains have been constructed from single atoms on the Cu_2N/Cu(001) surface using an STM tip [105]. Spin-flip excitations were detected by STS which revealed an AFM coupling of the Mn atoms. This coupling gives rise to differences between chains consisting of an even and odd number of atoms. Due to the insulating Cu_2N layer the Mn chain is almost decoupled from the metallic surface giving rise to quantum mechanical effects. The ground state of these chains cannot be described by a static magnetic structure, but is given by a superposition of all possible spin configurations. The energy of the spin-flip excitations is equivalent with the energy of the first, second, etc, excited state.

While both studies revealed intriguing magnetic properties of atomic chains, they did not provide a real-space image of the magnetic structure, either due to the lack of spatial resolution of XMCD in the case of the Co chains or due to quantum mechanical fluctuations in the Mn chains. In the framework of my PhD thesis, I conducted SP-STM measurements on Fe chains on an Ir substrate to investigate the magnetic properties in real space with atomic resolution.

5.2. SP-STM measurements on Fe chains on (5×1)-reconstructed Ir(001)

As discussed in Sec. 5.1, the magnetic order in one-dimensional structures is much more prone to quantum and thermal fluctuations compared to two- or three-dimensional structures. This makes magnetic measurements in real space especially difficult. In addition, the observed modulation along the Fe chains due to contaminations (see Sec. 4.4.5) can be mistaken for magnetic contrast which can appear very similar, cf. [15]. Therefore, the SP-STM data has to be evaluated very carefully.

As I have shown in the previous sections, the Fe chains on the reconstructed Ir(001) surface can grow in different adsorption sites and are sometimes contaminated with adsorbates on top of the chain. During my thesis I investigated the magnetic structure of the clean Fe chains grown in the inner hollow sites of the reconstruction. In order to prove that any contrast observed in SP-STM measurements is due to magnetic contrast, I characterized the very same sample in advance using conventional STM. For the SP-STM measurements I used W tips which were coated with either a Cr film or an Fe film (see Sec. 4.3 for details).

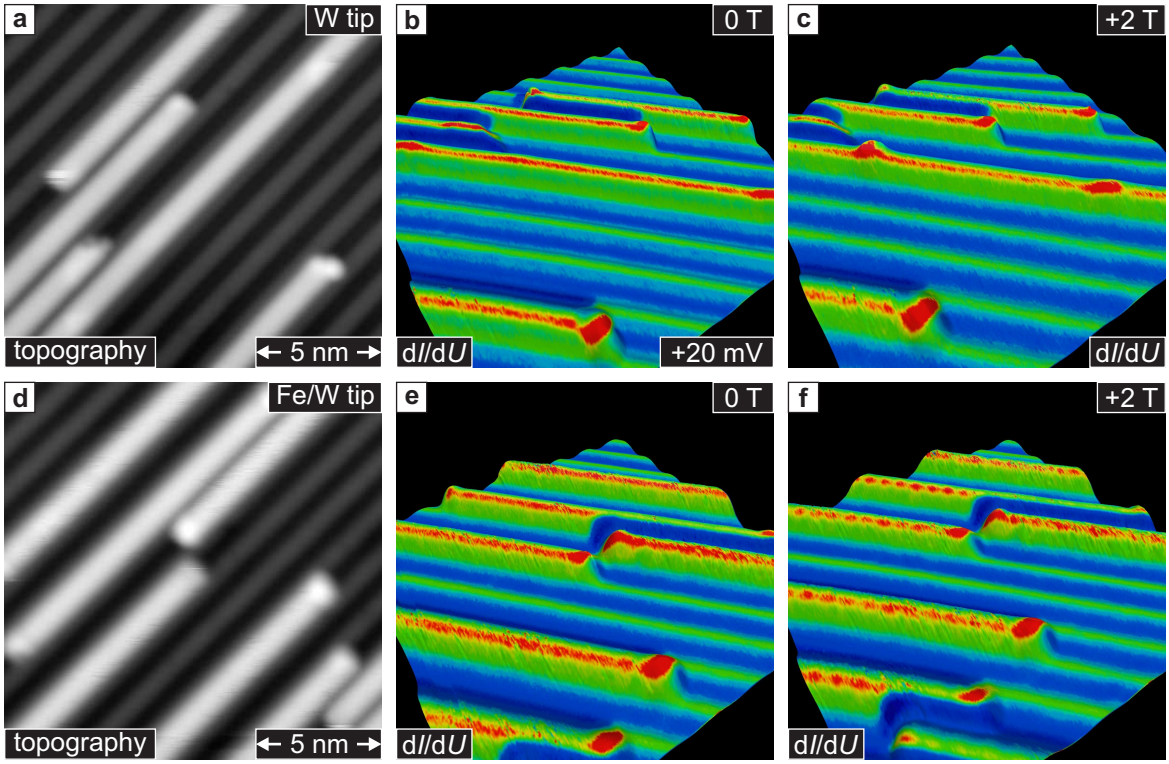

Figure 5.1: STM and SP-STM measurements on the same sample. **a** and **b**, Constant current STM image and the simultaneously acquired $\mathrm{d}I/\mathrm{d}U$-map at $B = 0\,\mathrm{T}$, respectively. **c**, The same sample area in an external magnetic field of $B = +2\,\mathrm{T}$. Similarly, **d** - **f**, SP-STM images using an Fe-coated W tip (for all images: $U = +20\,\mathrm{mV}$, $I = 5\,\mathrm{nA}$, $U_{\mathrm{mod}} = 2\,\mathrm{mV}$, $T = 8\,\mathrm{K}$). The periodic modulation is only visible when imaged with a spin-sensitive tip in an external magnetic field.

Figure 5.1 a and b show a constant current image and the simultaneously acquired $\mathrm{d}I/\mathrm{d}U$-map of the sample, respectively, taken with a nonmagnetic W tip at $B = 0\,\mathrm{T}$. All of the chains reside in the inner hollow sites and no modulation along the chain axis is visible in either image. In Fig. 5.1 c a $\mathrm{d}I/\mathrm{d}U$-map of the same sample area is shown, this time at an external magnetic field of $B = +2\,\mathrm{T}$. Again, no periodic modulation can

be observed. Since these measurements are performed with an applied bias voltage of $U = +20\,\mathrm{mV}$, I can conclude that the Fe chains are devoid of adsorbates (see Sec. 4.4.5). After these characterization measurements, I replaced the W tip by a spin-sensitive, Fe-coated W tip, while the sample resided in a parking spot next to the STM at lHe temperature, and repeated the measurement. The SP-STM images in Fig. 5.1 d - f are recorded with the same parameters as the images in Fig. 5.1 a - c but with the Fe-coated tip. As can be seen, also in the measurements with the spin-sensitive tip no modulation along the chain axis is visible, but when a magnetic field is applied a very weak periodic modulation arises on every chain, see Fig. 5.1 f. Given that the chains do not exhibit this periodic modulation when imaged with a nonmagnetic tip at any magnetic field, its origin is definitely the magnetic structure of the Fe chains. A closer look into the SP-STM data in Fig. 5.1 d shows more noise compared to the STM measurements presented in Fig. 5.1 a, which is probably due to an increase in the adsorbate density during the time the sample was residing outside of the STM. Since the magnetic signal in Fig. 5.1 f is very small and to avoid the contamination of the sample during the tip exchange, I performed additional SP-STM measurements on freshly prepared samples.

Figure 5.2 a shows an SP-STM constant current image of the Fe chains recorded with a Cr-coated tip without an external magnetic field. As can be seen in this image, the chains appear featureless, and also the simultaneously acquired $\mathrm{d}I/\mathrm{d}U$-map in Fig. 5.2 b shows a homogeneous LDOS on the chains and no differences between different chains. This measurement is in accordance with the measurements shown in Fig. 5.1 b: the chains do not display any magnetic feature for these measurement parameters. The uniform appearance of the chains changes significantly when examined with the Cr-coated tip in an external magnetic field, since all of the chains, regardless of their length, exhibit a modulation along their axes with a periodicity of three atomic distances (see Fig. 5.2 c and line profiles in d). In contrast to the modulation due to adsorbates on top of the chains described in the previous section, this modulation is not only visible close to the Fermi energy but persists over a wide range of applied bias voltages (see also Fig. 5.4).

The tip used for these measurements was sensitive to the out-of-plane component of magnetization, maxima and minima along the chain axis therefore represent areas with magnetization components pointing up or down with respect to the surface [107]. The modulation can be explained by a spin spiral state with an angle of 120° between the magnetic moments of neighboring atoms along the chain axis, as sketched in Fig. 5.2 d. By applying a magnetic field in the opposite direction (Fig. 5.2 d) the periodic contrast is reversed when using a Cr-coated tip. Due to the AFM ordering of the Cr-coated tip, its magnetization direction does not change when applying magnetic fields of this strength (see also Sec. 4.3). Thus, the inversion of magnetic contrast along the chain axis can only be explained when the spin spiral structure of the Fe chains aligns with

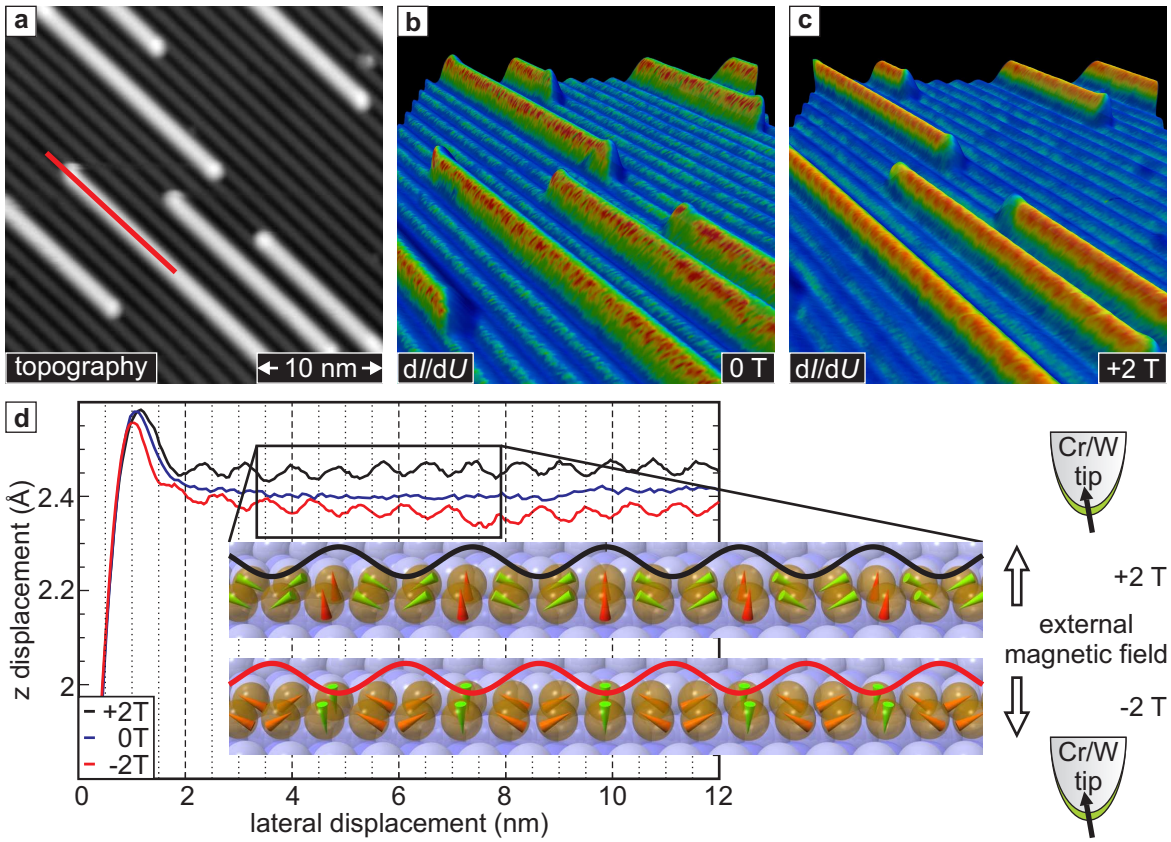

Figure 5.2: SP-STM measurements on Fe chains on Ir(001) using a Cr-coated W tip. **a** and **b**, Constant current STM image and the simultaneously acquired dI/dU-map at $B = 0\,\mathrm{T}$ ($U = +50\,\mathrm{mV}$, $I = 5\,\mathrm{nA}$, $U_{\mathrm{mod}} = 5\,\mathrm{mV}$, $T = 8\,\mathrm{K}$). **c**, dI/dU-map of the same sample area at $B = +2\,\mathrm{T}$ ($U = +400\,\mathrm{mV}$, $I = 5\,\mathrm{nA}$, $U_{\mathrm{mod}} = 20\,\mathrm{mV}$, $T = 8\,\mathrm{K}$). All chains display a periodic modulation when imaged in a magnetic field. **d**, Line profiles of the chain marked by the red line in **a** for different values of B.

the magnetic field. When turning off the magnetic field the modulation vanishes and the chains again appear featureless (blue line in Fig. 5.2 d).

Repeating this experiment with an Fe-coated tip, the modulation is expected to show no phase shift between opposite magnetic fields, since the magnetic structure as well as the magnetization of the tip align with the magnetic field (see Sec. 4.3). Similar to Fig. 5.2, Fig. 5.3 a shows a constant current image of the sample while Fig. 5.3 b and c are dI/dU-maps of the same area at $B = 0\,\mathrm{T}$ and $B = +2\,\mathrm{T}$, respectively. As for the Cr-coated tip, the modulation on the chains shows up when an external magnetic field is applied, while it is not visible for $B = 0\,\mathrm{T}$. In Fig. 5.3 d line profiles of the same chain in different magnetic fields are shown and the periodic modulation due to the spin spiral does not show a phase shift for opposite magnetic fields as expected.

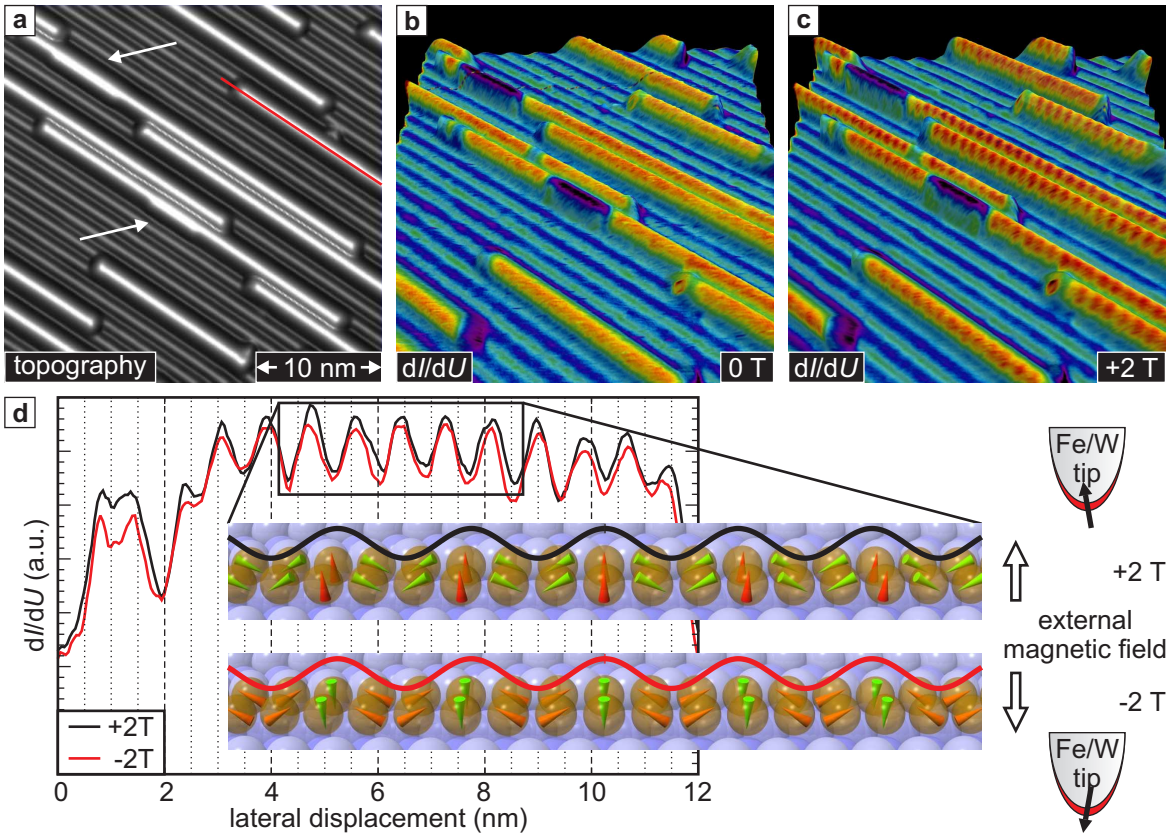

Figure 5.3: SP-STM measurements with an Fe-coated tip. **a**, Constant current SP-STM image and **b**, the simultaneously acquired $\mathrm{d}I/\mathrm{d}U$ map at $B = 0\,\mathrm{T}$. **c**, The same sample area in an external magnetic field of $B = +2\,\mathrm{T}$ (for all images: $U = +500\,\mathrm{mV}$, $I = 5\,\mathrm{nA}$, $U_{\mathrm{mod}} = 20\,\mathrm{mV}$, $T = 8\,\mathrm{K}$). **d**, Line profiles in opposite magnetic fields corresponding to the red line in **a**.

By comparing Fig. 5.2 c to Fig. 5.3 c one observes that the magnetic contrast is much larger when using an Fe-coated tip instead of a Cr-coated tip. However, the amplitude of the magnetic contrast is well below 10 pm for both tips, which is a factor of 2 smaller compared to the contrast due to contaminations. Therefore, the amplitude of the modulation is an additional indicator for the origin of the periodic pattern.

On closer examination, the amplitude of the magnetic contrast differs from chain to chain, indicating a correlation of the contrast strength and the chain length (see also p. 65). In addition, two chains in Fig. 5.3 a show areas where the chains exhibit protrusions (white arrows), which appear much darker in the $\mathrm{d}I/\mathrm{d}U$-map in Fig. 5.3 b. Since the chains widen only in one direction, these areas can be identified as a local zigzag configuration of an otherwise inner hollow site chain.

As described in Sec. 4.4.5, the periodic modulations due to contaminations vanish in

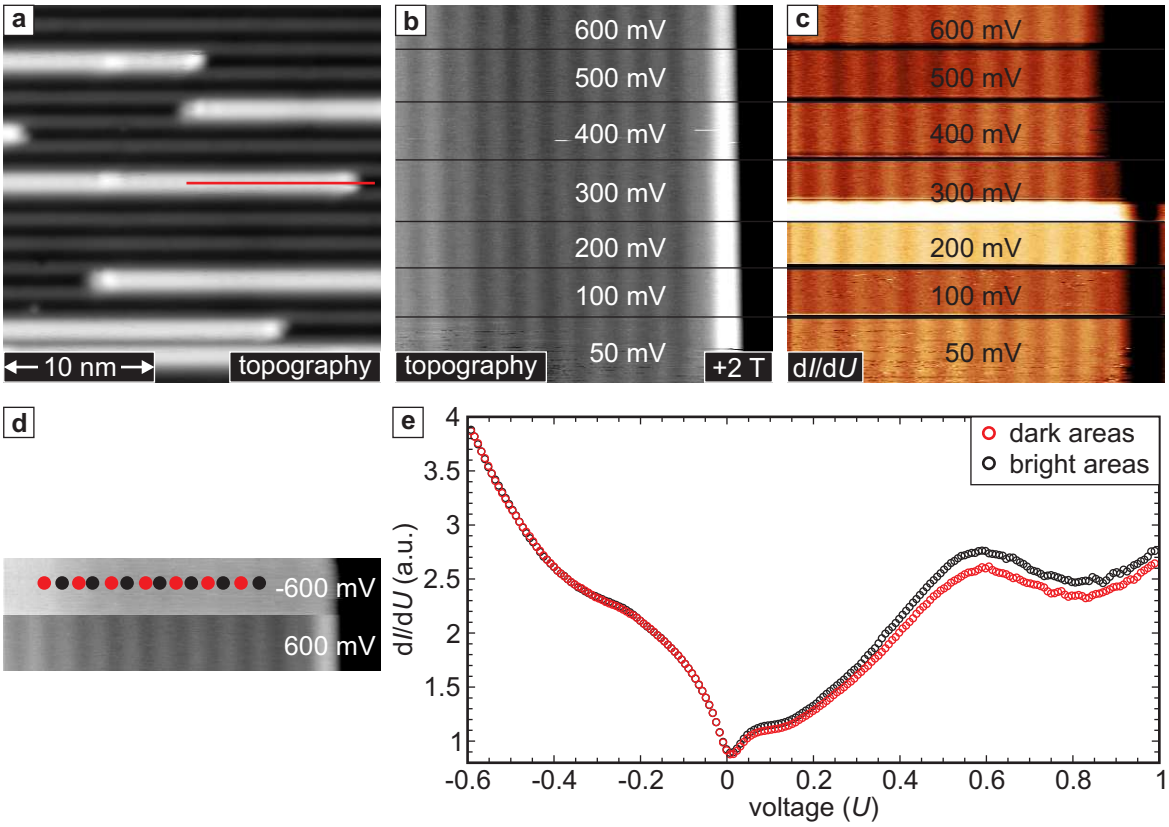

Figure 5.4: SP-STM measurement on an Fe chain at different bias voltages. **a**, Constant current SP-STM image at $B = +2\,\mathrm{T}$ ($U = +50\,\mathrm{mV}$, $I = 5\,\mathrm{nA}$, $T = 8\,\mathrm{K}$). **b** and **c**, Constant current and $\mathrm{d}I/\mathrm{d}U$ line mode measurements on top of the chain marked by the red line in **a**, respectively. The modulation due to the magnetic structure persists over a wide range of applied bias voltages, in contrast to the modulation due to hydrogen. **d**, Constant current line mode measurements at $U = \pm 600\,\mathrm{mV}$ on the same chain as in **b**. **e**, $\mathrm{d}I/\mathrm{d}U$-spectra taken at spots marked with the dots in **d** on top of bright areas (black dots) and dark areas (red dots) of the modulation, respectively ($U_{\mathrm{stab}} = -600\,\mathrm{mV}$, $I_{\mathrm{set}} = 5\,\mathrm{nA}$, $U_{\mathrm{mod}} = 10\,\mathrm{mV}$, $T = 8\,\mathrm{K}$).

the STM images for voltages far away from the Fermi level. To investigate the voltage dependence of the magnetic contrast I scanned the chain marked by the red line in Fig. 5.4 a in the line mode at different voltages. Figure 5.4 b and c show waterfall plots similar to Fig. 4.12 and the magnetic contrast persists over a wide range of voltages, from close to the Fermi level ($U = 50\,\mathrm{mV}$) up to $U = 600\,\mathrm{mV}$. This acts as further evidence that the contrast is not due to the contaminations with hydrogen described in the previous section. The modulation shows no phase shift over the whole voltage range displayed in Fig. 5.4 b and c, indicating that the polarization of the sample does not

change its sign. This is further corroborated by $\mathrm{d}I/\mathrm{d}U$-spectra on the bright and dark areas of the modulation. Figure 5.4 d shows a line mode measurement at $U = \pm 600\,\mathrm{mV}$ on the same chain as in Fig. 5.4 b and c. The modulation, which is clearly visible at $U = +600\,\mathrm{mV}$ is almost vanished at the negative bias voltage. Therefore I stabilized the tip at $U = -600\,\mathrm{mV}$ for the $\mathrm{d}I/\mathrm{d}U$-spectra shown in Fig. 5.4 e to avoid distance related measurement artifacts. Each spectrum is averaged over 7 single point spectra (see black and red dots in Fig. 5.4 d). They lie perfectly on top of each other in the negative bias range while they reveal a spin contrast for the whole positive range. The shape of the spectra is in very good agreement to the spin-averaged $\mathrm{d}I/\mathrm{d}U$-spectra presented in Sec. 4.4.4.

5.3. Physical origin of the spin spiral in the Fe chains

5.3.1. DFT calculations

While I have unambiguously shown that the periodic modulation along the chain axis is due to the magnetic structure of the Fe chains, the proposed spin spiral structure (see Fig. 5.3 d) cannot unequivocally be identified as the ground state of the system. The three atom periodicity could also be explained by a collinear ↑↑↓-state, whose magnetic unit cell consists of three pairs of atoms as well, with two moments pointing up (↑) and one moment pointing down (↓). However, this state is unlikely since it has been shown in a previous theoretical work that among the collinear states (FM, AFM and ↑↑↓) the ↑↑↓ is not the ground state of the Fe chains [77].

The occurrence of the spin spiral state and the interplay of the different magnetic interactions can be understood based on DFT calculations. Dr. Yuriy Mokrousov from the Forschungszentrum Jülich performed these calculations in the local density approximation using the `FLEUR` code [108]. The magnetic phase space can be explored by calculating flat spin spirals, which are the general solution of the classical Heisenberg model $E_\mathrm{H} = -\sum_{ij} J_{ij}\mathbf{S}_i \cdot \mathbf{S}_j$ for a periodic lattice, as discussed in Sec. 2.1. Such a spin spiral, propagating along the chain, is given by $\mathbf{S}_i = S(\cos(qai), 0, \sin(qai))$, where a is the lattice constant and $\mathbf{q} = (q, 0, 0)$ is the characteristic spin spiral vector. Varying q from $q = 0$ (FM state) to $q = \pm 0.5\,\frac{2\pi}{a}$ (AFM state), all possible spin spirals are covered giving rise to the spin spiral dispersion energy $E(q)$ (blue dots in Fig. 5.5 a). Positive and negative values of q denote clockwise and counter-clockwise spin spirals, respectively, and the dispersion is symmetric with respect to $\pm q$, as expected from the Coulomb interaction. It can be seen, that the FM solution is most favorable among all states, however, the strong FM exchange found in free-standing bi-atomic Fe chains (FM state $\approx 75\,\mathrm{meV/Fe}$ atom below the AFM state, see blue dashed line) is almost completely quenched. This is due to the strong hybridization with the Ir substrate resulting in a difference between the FM and the AFM state of only $\approx 1\,\mathrm{meV/Fe}$ atom.

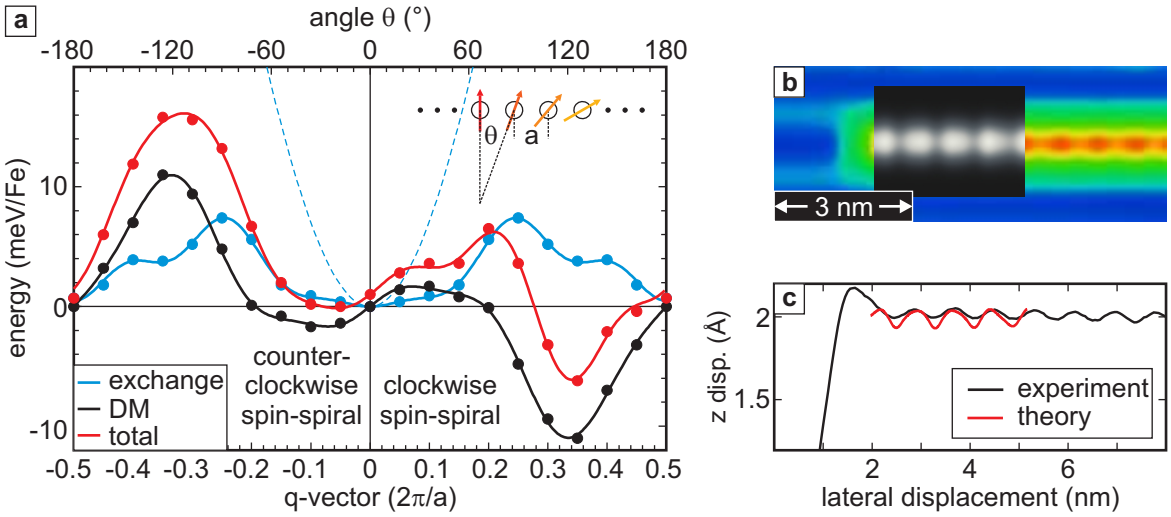

Figure 5.5: DFT calculations and comparison to experimental findings. **a**, The spin spiral dispersion from first principles calculations: contributions from Heisenberg exchange (blue dots) and DM interaction (black dots) and their sum (red dots). The lines represent fits to the calculations with an extended Heisenberg model and the dashed blue line is the Heisenberg exchange dispersion of a free-standing bi-atomic Fe chain. **b** and **c**, Comparison of a simulated SP-STM image of a 120° spin spiral (gray scale inset) with experimental data (color) and the corresponding line profiles, respectively.

Since the exchange interactions in these bi-atomic Fe chains are very small, the spin-orbit interaction can have a strong influence on the spin spiral dispersion as proposed in Ref. [81]. As shown in Sec. 2.2.1, the SOI gives rise to the magnetic anisotropy energy $E_{\mathrm{ani}} = \sum_i K_i \sin^2 \varphi_i$. The easy axis of the Fe spin moments is out-of-plane (z-axis in Fig. 4.5 b) and about 2 meV/Fe atom lower in energy than the two high-symmetry in-plane directions. Additionally, the SOI induces the anti-symmetric DM interaction $E_{\mathrm{DM}} = \sum_{i,j} \mathbf{D}_{ij} \cdot (\mathbf{S}_i \times \mathbf{S}_j)$, see Sec. 2.2.2. A non-vanishing E_{DM} can only arise when the sample system lacks inversion symmetry [17]. Since the Fe chains reside on the Ir surface, which breaks the inversion symmetry, E_{DM} can play a crucial role for the magnetic structure of the Fe chains. Based on symmetry arguments, $\mathbf{D}_{ij}$ aligns along the y-axis, favoring cycloidal spin spirals where the magnetic moments rotate in the xz-plane (cf. Fig. 4.5 b) [18, 22].

The correction to $E(q)$ due to the DM interaction, $E_{\mathrm{DM}}(q)$, is calculated by DFT using the charge density of the spin spiral state without SOI as the starting point. The results for $E_{\mathrm{DM}}(q)$ are presented as black dots in Fig. 5.5 a, and show that the magnitude of $E_{\mathrm{DM}}(q)$ competes with the contribution from the Heisenberg exchange, reaching as much as 10 meV. Summing up Heisenberg and DM contributions and including an energy shift due to the MAE, we get a robust cycloidal spin spiral ground

state several meV below the FM state, in the vicinity of $q \approx +1/3\,\frac{2\pi}{a}$ (red dots). This value of the spin spiral vector corresponds to a clockwise 120° spin spiral, running along the chain axis[2]. Owing to the antisymmetric nature of $E_{\mathrm{DM}}(q)$ with respect to $\pm q$, the counter-clockwise spin spiral state with $q = -1/3\,\frac{2\pi}{a}$ is much higher in energy, with $\Delta E \approx 20\,\mathrm{meV}$. Noticeably, the magnetic unit cell of the 120°-state consists of three Fe atoms along the chain axis, which is the *minimal* size necessary to obtain a non-collinear solution. As shown in Fig. 5.5 b and c, a simulated SP-STM image of such a 120° spin spiral based on the DFT calculations is in excellent agreement with the experimental findings.

5.3.2. MC simulations

While the first-principles calculations find this 120° spin spiral as the magnetic ground state of the Fe chains, it is still an open question why no magnetic contrast was observed in the SP-STM experiments at $B = 0\,\mathrm{T}$. To understand the influence of temperature and magnetic field on the Fe chains Dr. Robert Wieser from the University of Hamburg performed simulations using a heat-bath Monte-Carlo (MC) method [24]. He employed an extended Heisenberg model $E_{\mathrm{tot}} = E_{\mathrm{H}} + E_{\mathrm{ani}} + E_{\mathrm{DM}} + E_{\mathrm{B}}$ which includes the effect of an out-of-plane magnetic field $E_{\mathrm{B}} = -\mu_s B \sum_i S_i^z$, where μ_s is the magnetic moment. The material parameters J_{ij} and $\mathbf{D}_{ij}$ are obtained from fits to the first-principles calculations (see blue and black line in Fig. 5.5 a). To capture the non-trivial dispersions of $E(q)$ and $E_{DM}(q)$, J_{ij} and $\mathbf{D}_{ij}$ parameters up to six nearest neighbors along the chain axis were included, which are displayed in Table 5.1. Due to a strong FM coupling between the pair of Fe atoms along the y axis ($J_{\mathrm{perp}} \approx 160\,\mathrm{meV/Fe\ atom}$) the chains can be described as a single strand of spins in the MC simulation.

$\mathrm{n^{th}}$ neighbor	1	2	3	4	5	6
J_{ij} (meV)	+0.53	+1.42	−0.12	−0.34	−0.29	+0.37
D_{ij} (meV)	+2.58	−2.77	−0.07	+0.63	−0.36	−0.12

Table 5.1: Exchange constants extracted from fits to the DFT calculations of Fig. 5.5. Note that the DM vector $\mathbf{D}_{ij}$ is given by $(0, D_{ij}, 0)$.

Since the Fe chains observed in the experiments show a broad length distribution ranging from only a few nm, corresponding to ≈10 pairs of atoms, up to several

[2]The energy minimum of the DFT calculations corresponds to an angle θ slightly larger than 120° leading to a spin spiral which is incommensurate to the underlying atomic lattice, and I will come back to this aspect later. However, the SP-STM measurements do not allow to distinguish between a commensurate and an incommensurate spiral.

tens of nm, corresponding to up to 150 pairs, we chose to investigate a representative chain consisting of 30 atoms along the chain axis with open boundary conditions. The magnetic moment of each Fe atom and the MAE were set to their DFT value of $\mu_s = 2.75\,\mu_\mathbf{B}$ and $K_i = 2\,\text{meV}$, respectively, and for reasons of simplicity the atoms at the ends of the chain are assumed to have the same magnetic moment and MAE as the atoms in the chain center. The value of the time-averaged magnetization in our MC simulations is normalized, meaning that a value of 1 corresponds to a non-fluctuating magnetic moment, while a value < 1 indicates thermal fluctuations.

To determine the magnetic state of the Fe chain at the measurement conditions, we started with a disordered configuration at $T = 200\,\text{K}$ in a magnetic field of $B = +2\,\text{T}$ and cooled down the chain to $T = 8\,\text{K}$. The resulting x-, y- and z-component of the time-averaged magnetization for each lattice site within the chain are shown in Fig. 5.6 a. This non-collinear magnetic state is similar to the experimentally observed 120° spin spiral except for small deviations of the angles, meaning that the spin spiral is inhomogeneous and incommensurate to the atomic lattice (compare Fig. 5.2 d and Fig. 5.6 a). The spins at the ends of the chain are aligned with the applied magnetic field and contribute to a finite total magnetization of the chain. The analogous simulation without a magnetic field also yields spin spiral order, however, while a snapshot looks similar to Fig. 5.6 a, thermal fluctuations lead to a vanishing time-averaged magnetization, see also Sec. 5.4. The same behavior is observed for chains with the same number of atoms but periodic boundary conditions, i.e. an infinite chain, at any magnetic field value. This means that in the finite chain the applied field locks the spin spiral in real space via an alignment of the end spins with the magnetic field, which underlines the importance of finite size effects for the experimental observations. Because end atoms have a lower coordination number and the end spins are therefore less bound, they are more susceptible to an external magnetic field than the spins in the chain center. Note that the time-averaged magnetization of the chain atoms is far below 1, indicating that thermal fluctuations are still pronounced at the measurement temperature of 8 K.

To gain more insight into the magnetic ordering of this finite chain, we investigate its spatial- and time-averaged out-of-plane magnetization M_z as a function of temperature for different values of B (see Fig. 5.6 b). Here, $M_z = 1$ means that all moments of the chain point along z. For $B = 0\,\text{T}$, M_z of the chain is zero at all T due to fluctuations, while as soon as an external magnetic field is applied a non-vanishing out-of-plane magnetization arises. At higher temperature this is the paramagnetic response of the magnetic moments to the applied magnetic field (see lower inset in Fig. 5.6 b), while upon decreasing the temperature, thermal fluctuations are reduced and the value of M_z increases. At the threshold temperature of $\approx 30\,\text{K}$ a crossover from paramagnetism to the spin spiral order occurs in the chain (see upper inset in Fig. 5.6 b), leading to a decrease of M_z for $T < 30\,\text{K}$. The small residual net magnetization is due to the

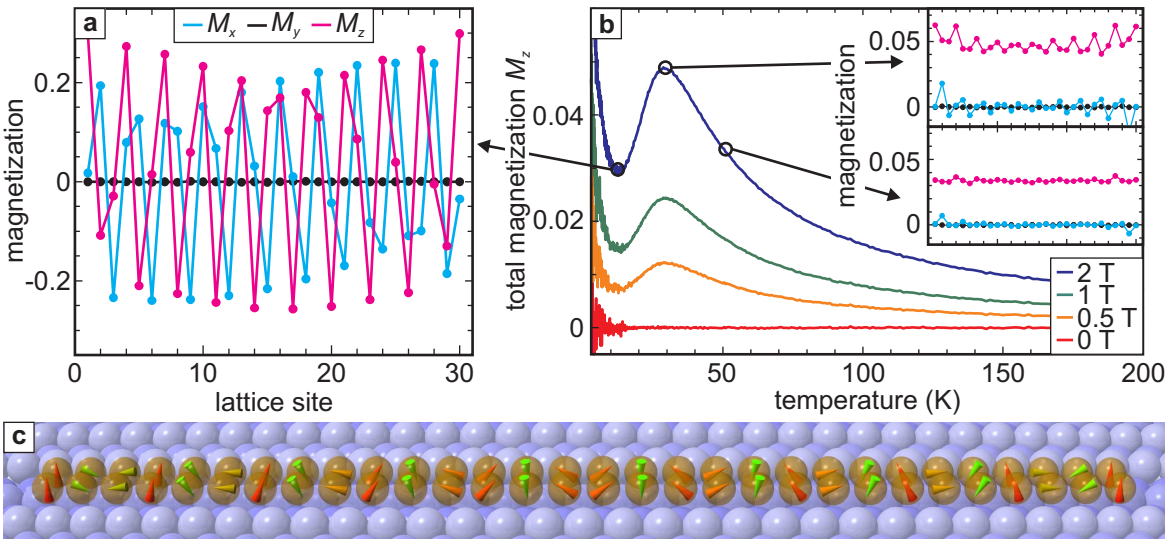

Figure 5.6: MC simulations for a chain 30 atoms long. **a**, Magnetization components of every atom for $T = 8\,\mathrm{K}$ and $B = +2\,\mathrm{T}$. **b**, Temperature dependence of M_z for different external magnetic fields applied along the z-axis is displayed. The insets show the laterally resolved magnetization for two different temperatures at $B = +2\,\mathrm{T}$ (components similar to **a**). **c**, Ball model of the Fe chain with the spin structure shown in **a**.

alignment of the end spins with the magnetic field and small distortions of the spin spiral ground state, see Sec. 5.4.

In addition to M_z, the temperature dependence of two order parameters was calculated which bare a very interesting and unique behavior. For ferromagnetic systems the order parameter is usually just the magnetization M of the system, which has a finite value if $T < T_\mathrm{C}$ and vanishes for $T > T_\mathrm{C}$. Since non-collinear magnetic structures usually have a vanishing magnetization, it is common to define the order parameter as $\boldsymbol{\kappa} \propto \mathbf{S}_i \times \mathbf{S}_j$ [109], the *vector spin chirality*. The direction of the vector $\boldsymbol{\kappa}$ defines the rotational sense of the magnetic structure and its length determines the thermal stability. For the Fe chains we define $\boldsymbol{\kappa}$ as

$$\boldsymbol{\kappa} = \langle \frac{1}{N} \sum_{i=1}^{N} \frac{1}{\sin(\theta_\mathrm{DFT})} (\mathbf{S}_i \times \mathbf{S}_{i+1}) \rangle, \tag{5.2}$$

where N is the number of atoms along the chain axis and $\theta_\mathrm{DFT} = 122.8°$ is the angle between neighboring moments for the DFT ground state of an infinite chain. For the spin spiral in the Fe chains the time-averaged vector $\boldsymbol{\kappa}$ is always pointing along the y-axis, similar to $\mathbf{D}_{ij}$, and can be written as $\boldsymbol{\kappa} = (0, \kappa, 0)$. A second order parameter θ, which gives the mean angle between neighboring magnetic moments, can be defined

as

$$\theta = \langle \frac{1}{N} \sum_{i=1}^{N} \arccos(\mathbf{S}_i \cdot \mathbf{S}_{i+1}) \rangle. \tag{5.3}$$

For the spin spiral order at $T = 0\,\mathrm{K}$, θ will tend to θ_{DFT}, while $\theta = 90°$ indicates complete magnetic disorder. Figure 5.7 a displays the temperature dependence of κ

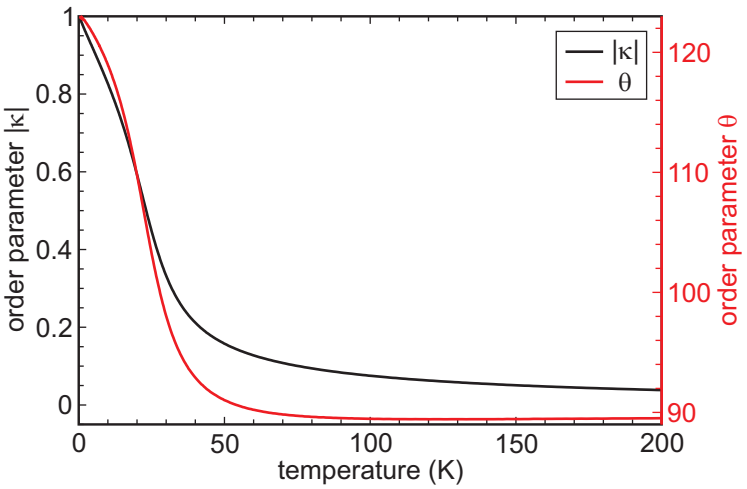

Figure 5.7: The two order parameters $|\boldsymbol{\kappa}|$ and θ as a function of temperature. Note that θ decays much faster with increasing temperature compared to $|\boldsymbol{\kappa}|$.

and θ which both show a continuous rise with decreasing temperature. Qualitatively, the two curves agree very well with the magnetization M_z shown in Fig. 5.6. For low temperatures $\kappa \approx 1$ and $\theta \approx 123°$, which indicates a stable spin spiral order in the chain and both order parameters decrease with increasing temperature. Interestingly, the order parameter κ has still a value significantly above zero at $T = 50\,\mathrm{K}$, $\kappa \approx 0.2$, while for the other order parameter $\theta(T = 50\,\mathrm{K}) \approx 90°$, indicating disorder. This means, that even though thermal fluctuations of the spins destroy the magnetic order, the rotational sense of the spin spiral is preserved. It can be interpreted as the fingerprint of the DM interaction, which favors one rotational sense over the other, and it is similar to a *chiral spin liquid phase* found in helical spin structures [109]. In the next section I will present further investigations of this intriguing aspect.

5.4. Simulations of magnetization dynamics in the Fe chains

5.4.1. The OOMMF simulation program and its extensions

To further understand the magnetization dynamics of the Fe chains I performed additional simulations using the Object Oriented MicroMagnetic Framework (OOMMF).

OOMMF was developed at the Information Technology Laboratory (ITL) at the National Institute of Standards and Technology (NIST) [110], and is a platform independent open source software package written in `C++`. It simulates the time evolution of micromagnetic systems by numerically solving the Landau-Lifshitz equation [111]

$$\frac{\mathrm{d}\mathbf{M}}{\mathrm{d}t} = -|\gamma|\mathbf{M} \times \mathbf{H}_{\mathrm{eff}} - \frac{|\gamma|\alpha}{M}\mathbf{M} \times (\mathbf{M} \times \mathbf{H}_{\mathrm{eff}}), \tag{5.4}$$

where $\mathbf{H}_{\mathrm{eff}}$ represents an effective magnetic field summing up all forces which act on the magnetic moment $\mathbf{M}$, γ is the gyromagnetic ratio and α is a damping constant. In contrast to the MC simulations presented in the previous section, Eq. 5.4 provides magnetization dynamics in real time which allows an estimation of the time scales in the experiment. The magnetic system is built up by identical cuboids which allows the investigation of basically every sample shape. These cuboids can interact with each other via, e.g., Heisenberg exchange or stray field. Additionally it is possible to study the response to an external magnetic field and define various magnetic anisotropies. The program has been proven to describe very accurately the magnetization dynamics in various micromagnetic structures.

In order to use this solver also for the dynamics of the Fe chains I had to include exchange interactions beyond the nearest neighbor interaction, which play a crucial role in the Fe chains. Therefore, the solver had to be extended by two routines which describe the Heisenberg exchange and the DM interaction, respectively, including these additional interactions. The two routines are based on the standard routine `uniformexchange` which describes the isotropic nearest neighbor Heisenberg exchange, given by the energy

$$H_{\mathrm{exch}} = \sum_{i,j} J_{ij}\mathbf{S}_i \cdot \mathbf{S}_j \tag{5.5}$$

with $J_{ij} = 0$ for $j = i$, and the resulting effective magnetic field

$$\mathbf{A}_{\mathrm{exch}} = \sum_{i,j} J_{ij}\mathbf{S}_j. \tag{5.6}$$

I adapted and modified these descriptions for the Heisenberg exchange to make it applicable to the specific demands of the bi-atomic Fe chains, namely

- no Heisenberg exchange along z-direction (see Fig. 4.5 b) since the chains are only one atomic layer high,
- a strong ferromagnetic coupling along the y-direction, which is in accordance to the DFT calculations (see Sec. 5.3.1),
- Heisenberg exchange up to the tenth nearest neighbor along the x-direction.

The source code which describes this interaction is included in the appendix A in the files `my_1dexchange.cc` and `my_1dexchange.h`.

The DM interaction is not included at all in this framework, since it is not important for most of the micromagnetic problems and it has been shown only very recently that this interaction can lead to non-collinear ground states in nanostructures on surfaces [15]. Similar to the routine described above, the DM interaction in this routine is described by its energy

$$H_{\mathrm{DM}} = \sum_{i,j} \mathbf{D}_{ij} \cdot (\mathbf{S}_i \times \mathbf{S}_j) \tag{5.7}$$

and the resulting effective magnetic field is given by

$$\mathbf{A}_{\mathrm{DM}} = \sum_{i,j} \mathbf{D}_{ij} \times \mathbf{S}_j. \tag{5.8}$$

For the specific problem of the Fe chains, with $\mathbf{D}_{ij}$ being parallel to the y-axis, this interaction couples magnetic moments up to the tenth nearest neighbor only along the x-axis (chain axis). The description of the DM interaction is attached in the appendix A in the files `my_dzyamoexchange.cc` and `my_dzyamoexchange.h`. Both routines, the Heisenberg exchange and the DM interaction, have been included into the existing OOMMF program and tests with beyond-nearest-neighbor interaction in one dimension have been successful. In general both routines should also work for three-dimensional problems but this has not been tested yet.

Since the standard OOMMF program works at zero temperature I included an additional routine which mimics the effects of a finite temperature [112, 113]. This program introduces a randomly fluctuating magnetic field $\mathbf{H}_{\mathrm{temp}}$ into the Landau-Lifshitz equation 5.4 with $\mathbf{H}_{\mathrm{eff}} \rightarrow \mathbf{H}_{\mathrm{eff}} + \mathbf{H}_{\mathrm{temp}}$. In this routine $\mathbf{H}_{\mathrm{temp}}$ matches two requirements:

1. the time average of the fluctuations $\langle \mathbf{H}_{\mathrm{temp}} \rangle$ cancels out, since the temperature does not drive a system into a certain magnetic state,

2. the random distribution of the values of $\mathbf{H}_{\mathrm{temp}}$ has a Gaussian shape.

5.4.2. Comparison between MC and OOMMF simulations

With all the ingredients now at hand, the program has to be tested to check, if it can describe the Fe chains and reproduce the experimental findings as well as the MC simulations. Therefore I included the same parameters as for the MC simulations and calculated the time evolution of a bi-atomic chain 30 atoms long for $T = 8\,\mathrm{K}$ at different values of an out-of-plane magnetic field B. Each cuboid in the simulation represents one chain atom and they were set to cubes with an edge length of 2 Å.

The time interval between subsequent simulation steps had to be set to the very small value of $\Delta t = 2 \cdot 10^{-16}$ s, since for any larger time constant the estimated changes of magnetization are too large and the system becomes chaotic. For each value of the magnetic field we ran $i = 10^8$ iterations which corresponds to a simulation time of $t_{\mathrm{tot}} = \Delta t \cdot i = 20$ ns. For each 10000th step all energies due to the different contributions as well as the magnetization components in x-, y- and z-direction for each atom were stored to a file.

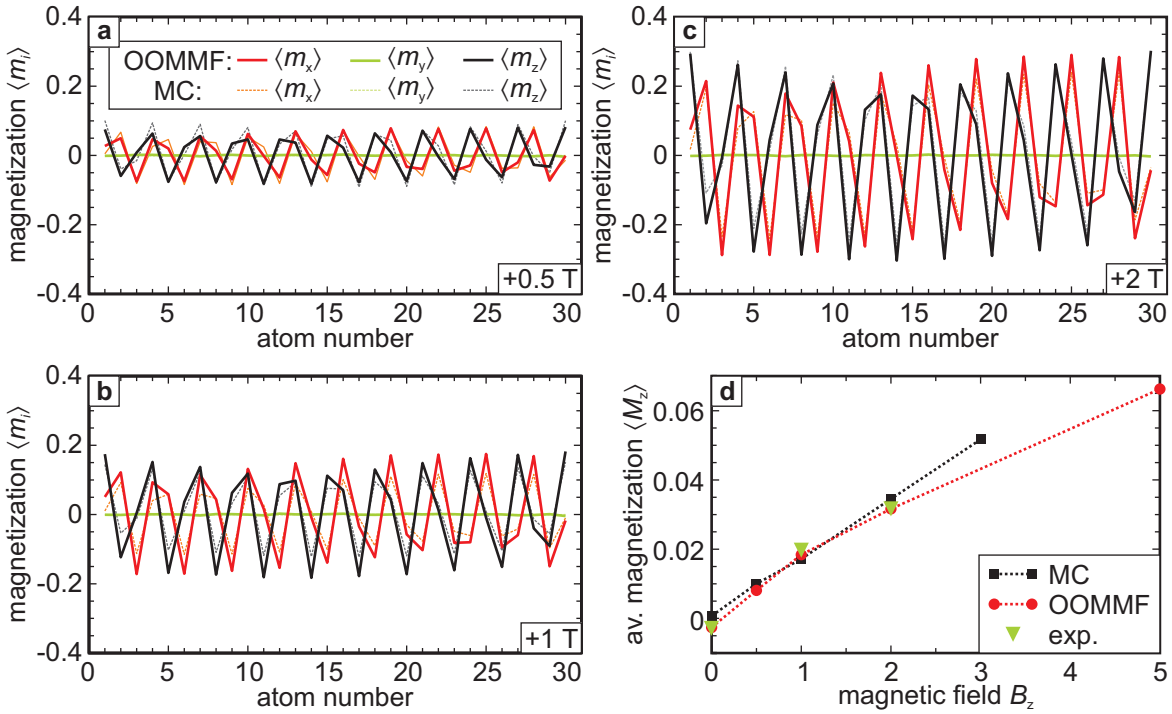

Figure 5.8: Comparison of simulations using OOMMF and MC for a chain of 30 atoms at $T = 8$ K. **a** - **c**, Time-averaged components of magnetization $\langle m_i \rangle$ for each atom of the chain for different values of B. **d**, Spatially averaged z-component of the magnetization $\langle M_z \rangle$ as well as the total magnetization $\langle M \rangle$ in dependence of B. Squares and circles represent the MC simulations and OOMMF simulations, respectively. The dashed gray curve is the magnetization curve of a superparamagnetic particle and is fitted to the data points. The green triangles represent the amplitude of the magnetic contrast from the experiments.

While for every time step the magnetization m of each atom equals 1, the time-averaged magnetization $\langle m \rangle = \sqrt{\langle m_x \rangle^2 + \langle m_y \rangle^2 + \langle m_z \rangle^2}$ gives information about the stability of the system against thermal fluctuations. In Fig. 5.8 a the time-averaged magnetization components for each atom of the chain at $B = 0.5$ T are shown and compared to the outcome of the MC simulations . It can be seen, that the two sim-

ulation methods give almost identical results. Similarly, the methods are in excellent agreement also for different values of B, as shown in Fig. 5.8 b and c, which justifies the use of OOMMF to study the time evolution of the Fe chains. In addition, we calculated the time-averaged magnetization of the whole chain, which is plotted in Fig. 5.8 d in dependence of the magnetic field B. Again, the two simulation methods are in good agreement.

Figure 5.8 d not only shows the comparison between MC and OOMMF simulations but also compares these results to the experiments. The green triangles represent the amplitude of the magnetic contrast measured along the chains for different magnetic fields. It is scaled so that the data point for $B = +2\,\mathrm{T}$ coincides with the total magnetization from the OOMMF simulations. It can be seen that the simulations agree quite well with the trend in the experimental findings, even though the data might be insufficient to draw conclusions.

Furthermore, I used OOMMF to calculate the ground state energy ($T = 0\,\mathrm{K}$) of the 30 atoms long, bi-atomic Fe chain as well as the contributions due to the different interactions. The energy contributions agree very well with the energies from the DFT calculations as it is shown in the appendix B in Table B.1. The comparisons of the OOMMF simulations to the experiment, the MC simulations and the DFT calculations show that the interactions presented in Sec. 5.4.1 are implemented correctly in the program and validate the use of OOMMF for simulations of the bi-atomic Fe chains.

5.4.3. Thermal fluctuations

The Mermin-Wagner theorem states that no long-range magnetic order exists in one-dimensional systems even at zero temperature. While the theorem is still valid for the Heisenberg model, it is obvious from the MC simulations (see Fig. 5.7) that the Fe chains exhibit the spin spiral order for temperatures below $\approx 30\,\mathrm{K}$ even at $B = 0\,\mathrm{T}$. Below that temperature the Fe chains act like superparamagnetic particles. Since the magnetic moments at the ends of the chain are less bound compared to the moments of the center atoms they will try to align with the easy axis, hence they will have a large z-component. Therefore, the chain fluctuates between two different states with the moments at the chain ends pointing either up (1) or down (-1). This results in a telegraph noise for the z-component of the end atoms which might be possible to detect at sufficiently low temperatures.

In Fig. 5.9 the z-component of the magnetic moment at one of the chain ends is shown in dependence of the simulation time for three different temperatures. For $T = 8\,\mathrm{K}$ the chain fluctuates quite often in the span of only 5 ns proving that it is difficult to observe the thermal fluctuations using conventional (SP-)STM at that temperature, see Fig. 5.9 a. This is in accordance with the SP-STM measurements in Fig. 5.2 b and 5.3 b since the fluctuations are in the GHz regime which is way too

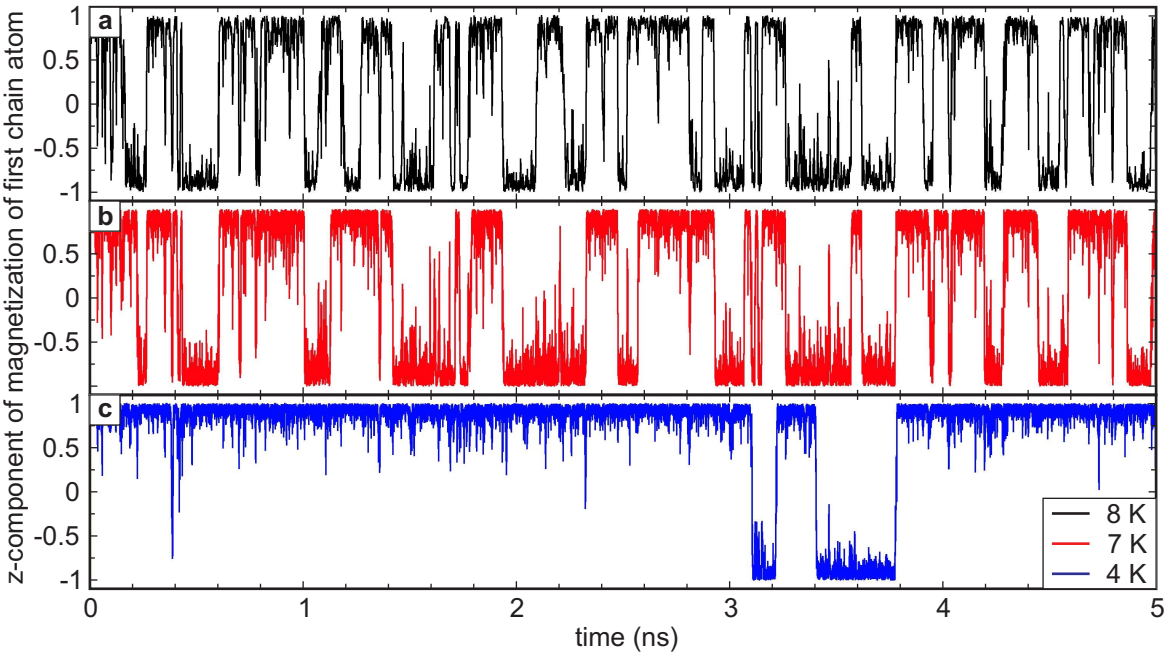

Figure 5.9: Thermally activated magnetization switching for a 30 atoms long chain at different temperatures. **a** - **c**, Time evolution of the z-component of magnetization of the first chain atom for $T = 8\,\mathrm{K}$, $T = 7\,\mathrm{K}$ and $T = 4\,\mathrm{K}$, respectively. Note, that the figure shows only cutouts of the simulation.

fast for standard STM measurements with the pre-amplifier cutting off all frequencies above $\approx 10\,\mathrm{kHz}$. Figure 5.9 b and c indicate that the switching rate is drastically decreased for lower temperatures ($T = 7\,\mathrm{K}$ and $T = 4\,\mathrm{K}$, respectively), but the thermal fluctuations at $T = 4\,\mathrm{K}$ are still in the GHz-regime.

However, it is possible to extract the mean lifetime τ from the simulations by assuming that the switching of the Fe chains follows the Néel-Brown law

$$\tau = \nu_0^{-1} \exp\left(\frac{E_b}{k_\mathrm{B} T}\right). \tag{5.9}$$

The attempt frequency ν_0 as well as the energy barrier E_b can be obtained by fitting the data points with an Arrhenius curve [114, 115]. This allows us to calculate a temperature at which the thermal switching could become observable in STM measurements. Comparison of the z-component of the magnetic moment of the first and the last atom reveals that the chain switches coherently from one state to the other, thereby validating the use of the Néel-Brown law. The mean lifetimes $\tau(T)$ for the 3 different temperatures can be calculated by dividing the simulation time t_tot by the number of switching events in this period, and they are presented as black dots in Fig. 5.10. Fitting these data points with Eq. 5.9 leads to an attempt frequency

$\nu_0 = 1.18 \cdot 10^{11}$ Hz and an energy barrier of $E_b = 1.64$ meV. To check if the value for E_b is reasonable, we can roughly estimate the energy barrier by comparing the ground state energy to the energy of the state with the magnetic moment of one chain end fixed along the x-axis. Since the chains switch from state 1 to state -1 by a rotation of the spin spiral around the y-axis, this energy difference ΔE should be a good estimation of E_b, and for a 30 atoms long Fe chain it is $\Delta E = 1.54$ meV, which is in very good agreement with the fit value of E_b. Moreover, the attempt frequency has a reasonable size given that values between 10^{10} Hz and 10^{16} Hz have been reported for magnetic nanoparticles [115, 116].

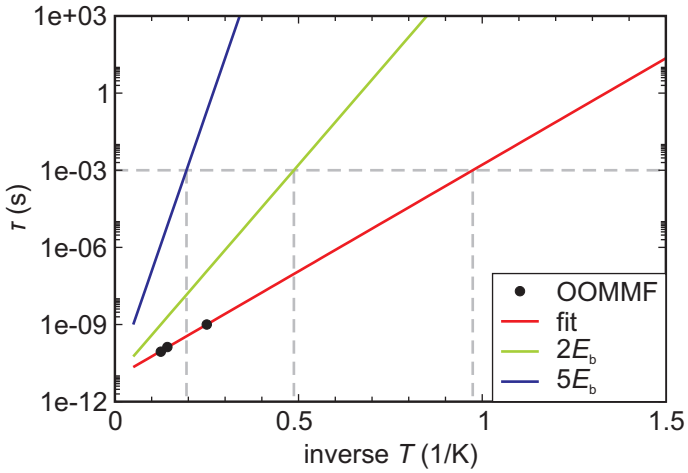

Figure 5.10: Temperature dependence of the mean lifetime. The black dots represent the data points from the OOMMF simulations shown in Fig. 5.9 and the red curve is a fit to these data points with Eq. 5.9. The green and blue lines are similar curves corresponding to an energy barrier twice and five times as large as the fit value, respectively.

By inserting the fit values for ν_0 and E_b in Eq. 5.9, τ can be plotted as function of the inverse temperature, which is the red line in Fig. 5.10. Assuming that the best time resolution which can be achieved by conventional STM is in the range of 1 kHz (gray dashed line), the temperature at which a switching should be observable is in the range of $T_{\text{obs}} \approx 1$ K. As already stated before, these simulations have been performed with the same magnetic moment and magnetic anisotropy energy for all atoms in the chain, regardless of their position. However, it is very common, that these values tend to become larger for atoms with reduced coordination [117] or for the edges of nanostructures [118]. Therefore the OOMMF simulations, and the respective fit, give a lower boundary for the expected mean lifetime τ. The green and red curve in Fig. 5.10 represent mean lifetimes for the same attempt frequency as the red curve but with an energy barrier twice and five times as large, which increases the observation temperature to $T_{\text{obs}} \approx 2$ K and $T_{\text{obs}} \approx 5$ K, respectively.

5.4.4. Temperature dependence of the order parameter

As I have shown in Sec. 5.3.2, the order parameter $\boldsymbol{\kappa}$ (Fig. 5.11 a and Eq. 5.2), which indicates the rotational sense of the spin spiral, is preserved for temperatures above the order temperature of $T \approx 30\,\mathrm{K}$. This can be evaluated quantitatively by investigating the angles between neighboring magnetic moments along the chain axis from snapshots of the simulation. In Fig. 5.11 b a histogram of the angle distribution for

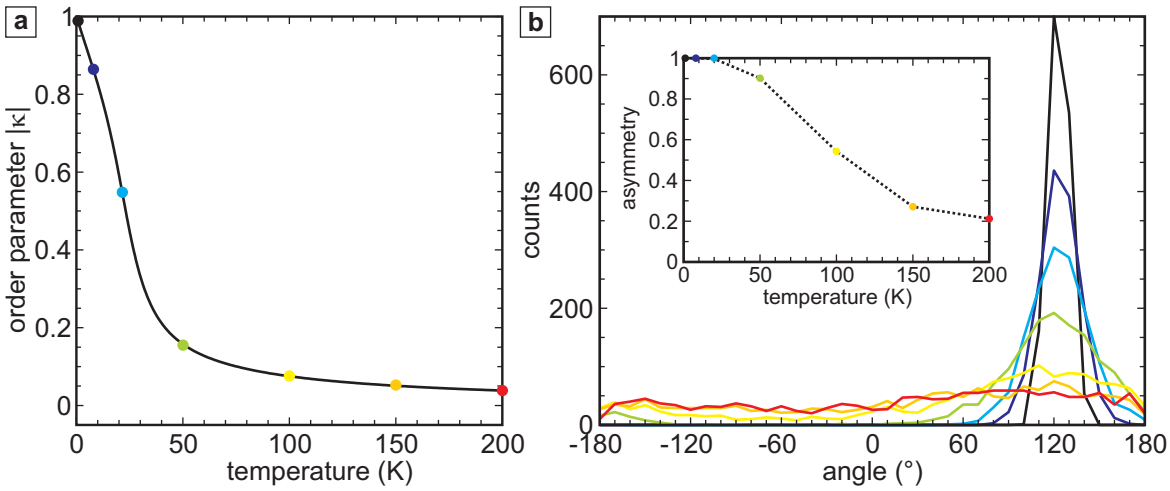

Figure 5.11: Angle distribution in a 30 atoms long Fe chain for different temperatures. **a**, $|\boldsymbol{\kappa}|$ as a function of temperature, see also Sec. 5.3.2. **b**, Histogram of the angle distribution in the xz-plane between neighboring spins. The angles are taken from 50 simulation snapshots of a 30 atoms long chain. The colors represent different temperatures, indicated by the colored circles in **a**. The inset shows the asymmetry of the angle distribution.

different temperatures is shown. For this histogram I evaluated the angles in the xz-plane between neighboring spins in a 30 atoms long chain from 50 snapshots of the simulations, which results in a total of 1450 angles for each temperature step. At $T = 1\,\mathrm{K}$ the angle distribution has a very narrow peak around θ_{DFT} (black line). This maximum is still very pronounced for $T = 8\,\mathrm{K}$ (blue line) which is in accordance to the measurements. The peak becomes broader for higher temperatures and is still visible at $T = 50\,\mathrm{K}$ (green line), which is well above the order temperature. Even at $T = 200\,\mathrm{K}$ (red line) a distinct imbalance between positive and negative angles can be observed from the simulations. This asymmetry can be expressed by $a = (\mathrm{counts}_+ - \mathrm{counts}_-)/(\mathrm{counts}_+ + \mathrm{counts}_-)$, where $+$ and $-$ indicate positive and negative angles, respectively, and it is shown in the inset of Fig. 5.7 b. This further illustrates that the DM interaction affects the thermal fluctuation even at $T = 200\,\mathrm{K}$, which leads to an asymmetry of $a \approx 0.2$ at this temperature.

5.4.5. Outlook I: Chains of different lengths

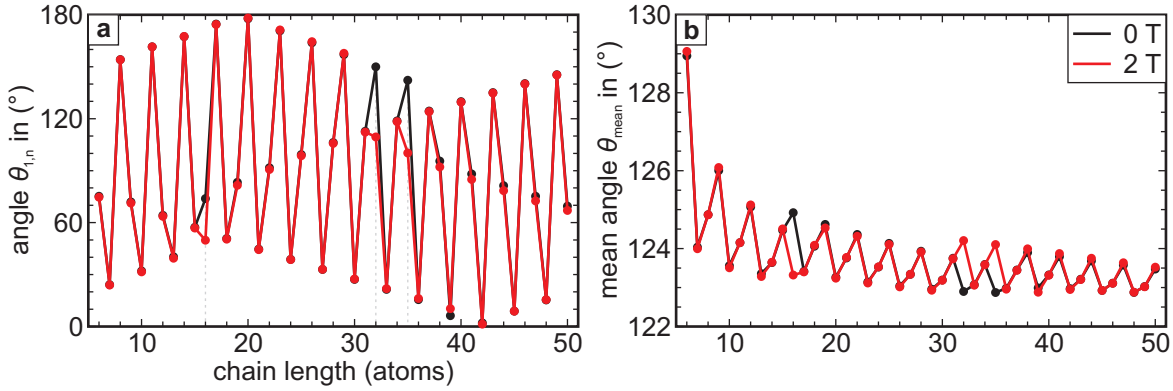

Figure 5.12: Angles in a spin spiral for different chain lengths with and without a magnetic field $T = 0\,\mathrm{K}$. **a**, Angle between the magnetic moments of both chain ends in dependence of the chain length. **b**, Mean angle of neighboring moments along the chain axis. The black and red curve represent values for $B = 0\,\mathrm{T}$ and $B = 2\,\mathrm{T}$, respectively.

Up to now, the simulations were performed only for a chain consisting of 30 pairs of atoms. I performed additional simulations for chains of different length, in order to study how the length affects the spin spiral structure. Therefore, I calculated the ground state energy ($T = 0\,\mathrm{K}$) for different chain lengths at $B = 0\,\mathrm{T}$ and $B = +2\,\mathrm{T}$. Figure 5.12 a shows the angle enclosed by the magnetic moments of the first and the last pair of atoms in the chain $\theta_{1,n}$ as function of the chain length n for $B = 0\,\mathrm{T}$ (black line) and $B = +2\,\mathrm{T}$ along the z-axis (red line), respectively. Since the spin spiral angle is close to 120°, $\theta_{1,n}$ shows a periodic dependence of the chain length modulo 3, e.g. $\theta_{1,20} \approx \theta_{1,23}$, with a long range pitch since the spin spiral is incommensurate to the atomic lattice. This is true not only for $B = 0\,\mathrm{T}$ but also for an applied magnetic field, which (almost) does not affect $\theta_{1,n}$. Only for very few chain lengths – namely 16, 32 and 35 atom long chains – the magnetic field changes $\theta_{1,n}$ significantly. This can also be seen in the mean angle θ_{mean} shown in Fig. 5.12 b, which is the average angle enclosed by neighboring magnetic moments along the chain axis. While θ_{mean} is almost the same at $B = 0\,\mathrm{T}$ and $B = 2\,\mathrm{T}$ for most of the chain lengths, it differs for the three, aforementioned chains. This means, that the energy of the external magnetic field E_{B} is quite small and cannot compete with the energy contributions from Heisenberg exchange, DM interaction and MAE (see appendix B for the energy contributions of the different interactions). Only for some chain lengths, E_{B} is large enough to force a comparably strong distortion of the spin spiral. In reverse, this means that small variations of the spin spiral angle do not cost much energy for the three chain lengths.

To further illustrate the dependence of the spin spiral on the chain length, Fig. 5.13 a and b show the angle enclosed by the magnetic moment of the first chain atom and the

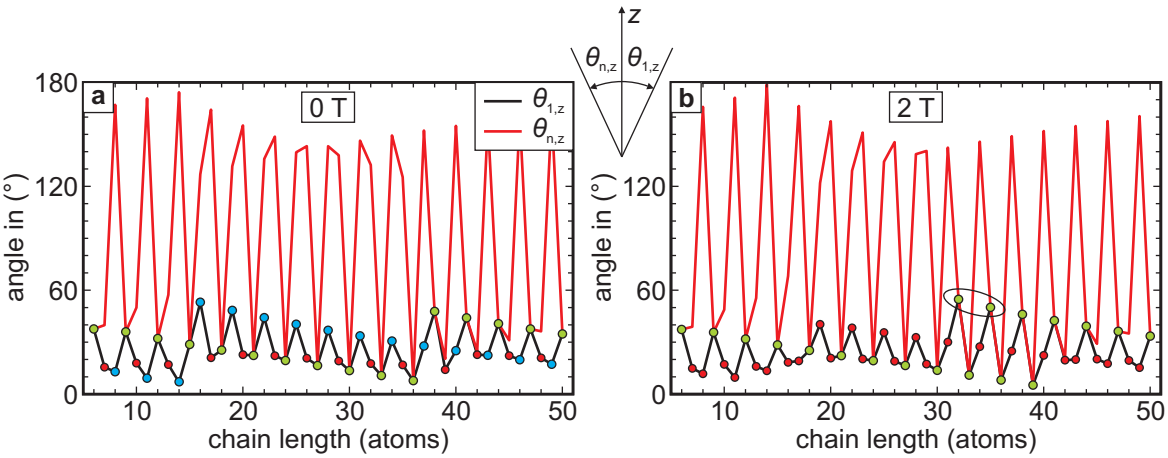

Figure 5.13: Angle of the first (red line) and last spin (black line) of the chain with respect to the z-axis for different chain lengths. **a** and **b**, Simulations for $B = 0\,\mathrm{T}$ and $B = 2\,\mathrm{T}$, respectively. The green and blue circles indicate chain lengths whose end spins enclose the same angle with the z-axis or x-axis, respectively. The red circles indicate chains which do not show a specific magnetic symmetry.

z-axis $\theta_{1,z}$ and the last atom and the z-axis $\theta_{n,z}$ at $B = 0\,\mathrm{T}$ and $B = 2\,\mathrm{T}$, respectively. The green circles in Fig. 5.13 a indicate the chain lengths for which $\theta_{1,z}$ and $\theta_{n,z}$ are identical. This does *not* mean that the first and last moment are parallel, but that the nth moment is a mirror image of the first moment with respect to the plane perpendicular to the chain axis and therefore both moments have the same z-component, $m_{z,1} = m_{z,n}$ (see inset in Fig. 5.13). This leads to a highly symmetric spin spiral, since also the second and the $(n-1)$th, the third and the $(n-2)$th, ... are mirrored (similar to Fig. 5.6 c). On the other hand, the blue circles mark the chain lengths for $\theta_{1,z} + \theta_{n,z} = 180°$. Similarly, this does *not* mean that the moments are antiparallel aligned, but that the moment of the last atom is a mirror image of the moment of the first atom, this time with respect to the plane parallel to the surface. In this state the two magnetic moments have the opposite z-component, i.e. $m_{z,1} = -m_{z,n}$. Since the Heisenberg and DM interaction are isotropic in the plane of the spin spiral, and the MAE is uniaxial (along the z-axis), also this state is highly symmetric. Given that $m_{z,i} = -m_{z,(n+1-i)}$ is true for all i, this state does not possess a net magnetic moment in z-direction. The chain lengths which do not have one of the aforementioned magnetic symmetries are marked with red circles.

With an applied magnetic field, shown in Fig. 5.13 b, all states with $m_{z,1} = m_{z,n}$ are preserved and still symmetric, while the symmetry is lifted for all chains, which have $m_{z,1} = -m_{z,n}$ at $B = 0\,\mathrm{T}$ including the 16 atoms long chain. This is due to the influence of B, which prefers the magnetic moments to align parallel, thereby distorts the spin spiral and lifts the degeneracy of the magnetic anisotropy energy. On

the other hand, some of the asymmetric chains become symmetric with an applied magnetic field, including the chains consisting of 32 and 35 atom pairs, cf. Fig. 5.12.

This could also explain the different magnetic contrast levels of the chains observed in the SP-STM measurements, cf. Fig. 5.3 c. The chains marked by a green circle in Fig. 5.13 with $m_{z,1} = m_{z,n}$ have an intrinsic net magnetization and are therefore more stable compared to the chains marked by a blue circle, which have only a magnetic moment induced by the external field.

These simulations reveal that the spin spiral angle depends strongly on the chain length and can be affected by an external magnetic field. However, I want to emphasize that the simulations are based on the simplification that all Fe atoms in the chain have the same magnetic moment and anisotropy. Due to these simplifications the discussion of the length effects and the influence of an external magnetic field on the spin spiral is rather speculative and of academic nature. Nevertheless, it might lead to a further understanding of the interplay of the different magnetic interactions in the Fe chains.

5.4.6. Outlook II: Information transport through the chains

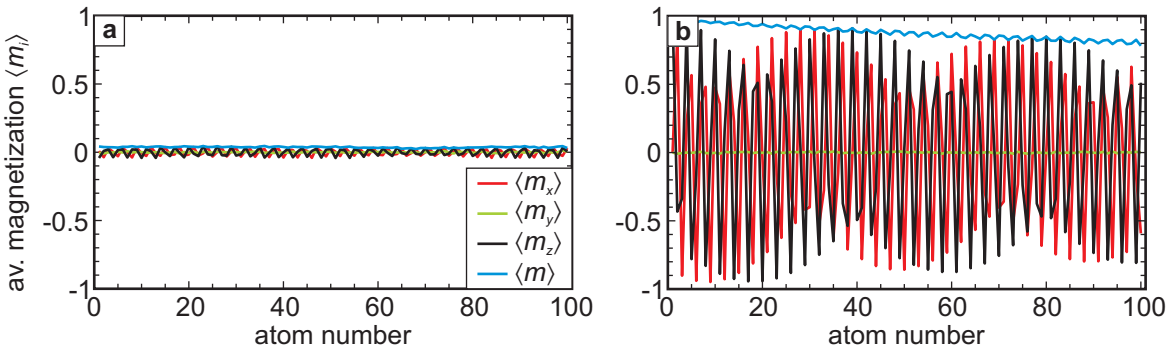

Figure 5.14: Simulation of a chain with one fixed end compared to the same chain with two open ends at $B = 0\,\mathrm{T}$ and $T = 8\,\mathrm{K}$. **a** The time-averaged magnetization of each atom $\langle m \rangle$ and its spatial components for a chain consisting of 100 pairs of atoms, without a fixed end. **b** The same chain with the magnetic moment of the left chain end fixed along the z-axis.

In today's computer chips, nanowires act as the connection between an input and the output in logic devices and transport the information in form of a small electric current. Similarly, spin chains can be utilized in future spintronic devices [50]. This implies that the correlation length of the spin state has to be on the order of the distance between the input and the output. To investigate the decay of the time-averaged magnetization $\langle m \rangle$ along the chain axis due to thermal fluctuations, I simulated an Fe chain with one end fixed while the other end is open at $B = 0\,\mathrm{T}$ and $T = 8\,\mathrm{K}$.

Figure 5.14 a shows $\langle m \rangle$ and its spatial components for a chain consisting of 100 pairs of atoms. The time-averaged magnetization of each atom is (almost) zero due to thermal fluctuations[3]. In comparison to the chain with no fixed end, Fig. 5.14 b shows the same chain while the magnetic moment of the left end of the chain is fixed along the z-axis, meaning $\langle m \rangle_1 = \langle m_z \rangle_1 = 1$. The magnetization of the last atom does not drop considerably, $\langle m \rangle_{100} \approx 0.8$, meaning that thermal fluctuations only play a minor role and do not destroy the magnetic ordering over a length of $\approx 25\,\mathrm{nm}$. Furthermore, $\langle m \rangle$ seems to decay linearly into the Fe chain. By interpolating this trend, 50 % of the information is preserved in a 250 atoms long chain, i.e., an atom more than 60 nm away from the input (atom 1) has still a time-averaged magnetization of $\langle m \rangle = 0.5$. Such an input could be realized by, e.g., a spin-polarized current [114, 45] or a stable magnetic particle [50].

5.5. Summary

In this chapter I presented experimental as well as theoretical investigations of the magnetic structure of bi-atomic Fe chains on the (5×1)-reconstructed Ir(001) surface. Using SP-STM in an external magnetic field, I was able to image a periodic magnetic contrast which is caused by the Fe chains' spin spiral ground state. DFT calculations performed by Dr. Yuriy Mokrousov are in excellent agreement with the measurements and reveal the antisymmetric Dzyaloshinskii-Moriya interaction as the driving force behind the formation of the spin spiral. Due to this interaction the spin spiral rotates only clockwise while the counter-clockwise rotation is much higher in energy. Even though the magnetic contrast in the SP-STM measurements could not be obtained without an external magnetic field, MC simulations reveal the spin spiral order for $T < 30\,\mathrm{K}$ at $B = 0\,\mathrm{T}$. At the measurement temperature of $T = 8\,\mathrm{K}$ the magnetic structure fluctuates as a macrospin due to thermal excitation on a time scale well below the time resolution limit of conventional SP-STM. Simulations with OOMMF predict that this temperature induced magnetization switching should become observable at temperatures around and below 1 K. The thermal fluctuations could also be suppressed by fixing the magnetization of one chain end with, e.g., a stable magnetic particle. Interestingly, the simulations also reveal that the rotational sense is preserved at temperatures well above the order temperature leading to an anisotropic, thermal fluctuation of the Fe atoms' magnetic moments, which can be interpreted as a spin liquid phase.

[3] The simulations are very time consuming since they are performed on an ordinary desktop computer. Therefore the small residual magnetization is due to an insufficient number of time steps used in the averaging process.

6. Magnetism of the iron monolayer on iridium(111)

6.1. Skyrmions

6.1.1. What is a skyrmion?

The *soliton* is a wave packet which moves through a dispersive and nonlinear medium without changing its shape or velocity. It was first discovered in 1834 by John Scott Russell (1808-1882) while observing a boat in a narrow channel which was drawn by horses. When the boat suddenly stopped, the wave caused by the boat did not, but continued to travel at the same speed without changing its shape [119]. Solitons can be explained by the cancellation of dispersive and nonlinear effects, e.g., a light pulse consisting of many different frequencies which propagates in a glass will change its shape over time, since different frequencies move with different velocities (dispersion). The refractive index, on the other hand, changes with the amplitude for a certain frequency (nonlinear Kerr effect). For a wave package with the right shape the two effects will cancel and it will travel as a soliton with constant shape and speed [120]. Solitons can be observed, e.g., as tidal waves in rivers or cloud formation in special atmospheric conditions, but it has also been demonstrated that solitons, as wave packages of light, can be used for loss-free data transmission in fiber optics [121]. Mathematically speaking, they are the solution of a nonlinear partial differential equation (PDE), e.g. the Landau-Lifshitz equation, see p. 57.

A special class of solitons are those which cannot decay into the trivial solution due to topological protection. Those *topological solitons* or *topological defects* arise when the solutions of the PDE are not homotopic, meaning that the soliton cannot be continuously deformed into the trivial solution [120]. Examples for topological solitons include screw dislocations in crystals, domain walls in ferromagnets or magnetic monopoles. About fifty years ago, Skyrme used the concept of topological solitons to describe particles (baryons) as defects of the boson field based on nonlinear field theory [122, 123]. He showed that these topological defects, now called *skyrmions*, are localized in space, are subject to attractive or repulsive interactions, assemble in ordered phases, undergo phase transitions and have quantized topological charges. The

charge, also known as *skyrmion number* or *winding number*, can be written as

$$S = \frac{1}{4\pi} \int \mathbf{n} \cdot \left(\frac{\partial \mathbf{n}}{\partial x} \times \frac{\partial \mathbf{n}}{\partial y} \right) \mathrm{d}x \, \mathrm{d}y, \tag{6.1}$$

where $\mathbf{n}$ is the vector field. Since Skyrme's seminal work, skyrmions have developed into a general concept in physics of all possible length scales ranging from elementary particles [123, 124] to Bose-Einstein condensates [125], liquid crystals [126] and the formation of cosmic structures [127]. They have been observed in quantum Hall magnets [128, 129] and show similarities to the vortex lattice in type-II superconductors [130].

6.1.2. Skyrmions in magnetism

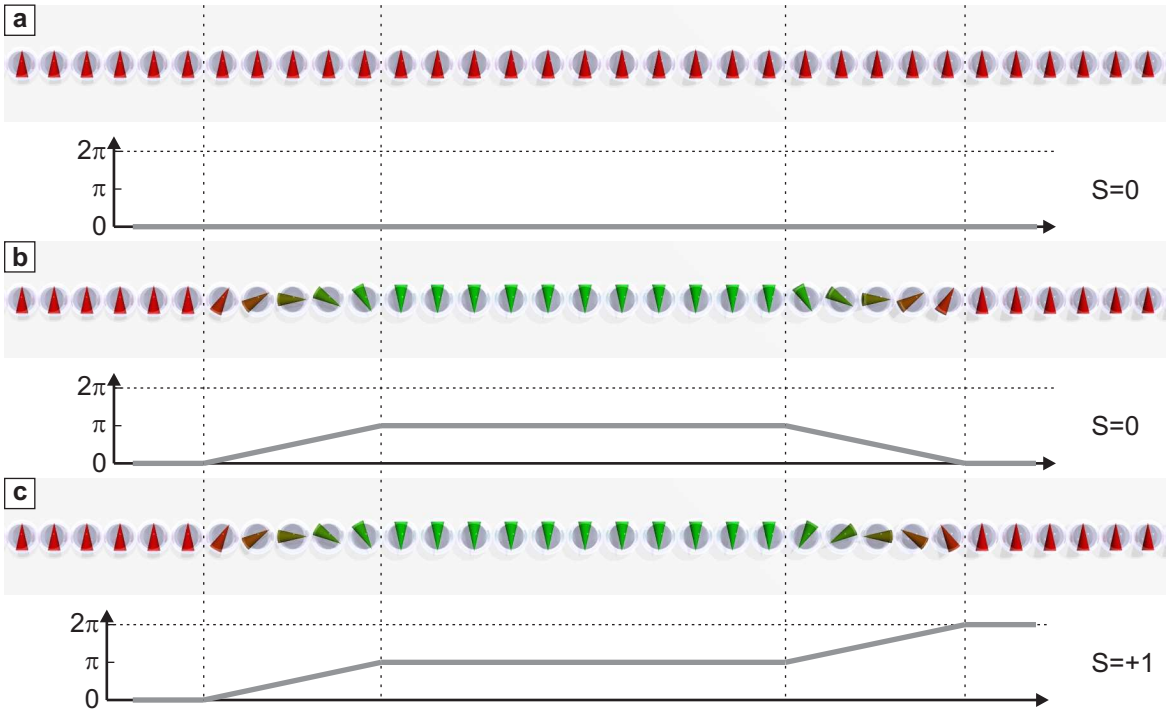

Figure 6.1: Schematic drawings of a one-dimensional crystal in different magnetic states. **a**, FM state with the corresponding skyrmion number $S = 0$. **b**, Two domain walls with opposite rotational sense ($S = 0$) and **c**, two domain walls with the same rotational sense resulting in $S = +1$.

Skyrmions have been predicted to exist as stable defects in magnetically ordered systems including but not restricted to ferromagnets [131]. The concept of skyrmions

in magnetic systems can be best illustrated for a one-dimensional crystal in which the direction of the spins is restricted to a plane. In this case Eq. 6.1 simplifies to

$$S = \frac{1}{2\pi} \int \frac{\partial \theta}{\partial x} \mathrm{d}x, \tag{6.2}$$

where θ is the angle between the magnetic moments of neighboring atoms. Figure 6.1 shows a one-dimensional crystal in three different magnetic states with the cones representing the direction of the magnetic moments at each lattice site. For the trivial FM ordering, shown in Fig. 6.1 a, Eq. 6.2 has the solution $S = 0$ since $\theta = 0$ for all neighboring moments. In Fig. 6.1 b the crystal has two domain walls which separate three magnetic domains. In this case the two domain walls have opposite rotational sense which leads to the same solution $S = 0$. If a magnetic field is applied parallel to the two outer domains, these two domains will grow while the domain in between the walls will shrink. Due to the opposite rotation of the walls, they can cancel each other easily and the inner domain is destroyed by the magnetic field. In contrast, the two domain walls shown in Fig. 6.1 c have the same rotational sense resulting in a non-vanishing skyrmion number ($S = +1$). The inner domain would also be shrunken by an upwards pointing magnetic field but it cannot be annihilated since it is topologically protected. Therefore, this magnetic configuration resembles a spin spiral which can be interpreted as the analogon to a skyrmion in a one-dimensional magnetic crystal.

For a two-dimensional crystal the skyrmion number is given by Eq. 6.1. To illustrate

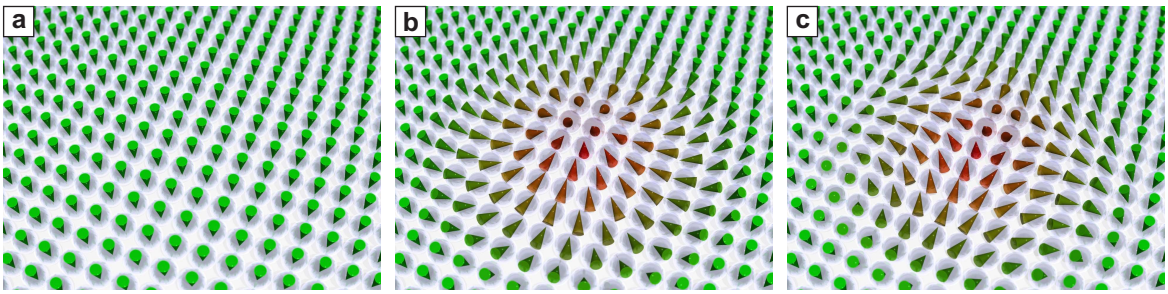

Figure 6.2: Schematic drawings of a thin magnetic film in different topological configurations. **a**, Ferromagnetic film with $S = 0$, **b**, Single skyrmion in the film ($S = +1$) and **c**, the corresponding antiskyrmion ($S = -1$).

skyrmions in two-dimensional magnetic systems, Fig. 6.2 shows a schematic representation of a thin ferromagnetic film in three different topological configurations with the cones indicating the magnetization direction. The trivial ferromagnetic solution is shown in Fig. 6.2 a. For this state the differentials in Eq. 6.1 are zero, which leads to a skyrmion number $S = 0$. Figure 6.2 b shows a single magnetic skyrmion in the ferromagnetic film, whose center has a magnetization antiparallel to the film. Along the radius of the skyrmion, the magnetization rotates continuously from the center to

the edge, and according to Eq. 6.1 this magnetic configuration has a skyrmion number of $S = +1$. The corresponding antiparticle with the opposite topological charge ($S = -1$), the *antiskyrmion*, is shown in Fig. 6.2 c.

One key ingredient for the formation of skyrmions is a broken space-inversion symmetry which is needed for a non-vanishing DM interaction, see Sec. 2.2.2. For non-centrosymmetric magnetic crystals, skyrmion lattices were predicted to be the energetically most favorable state for a certain range of external magnetic field values [131]. Recently, such lattices were observed experimentally in the bulk magnets MnSi [16], FeCoSi [132], and FeGe [133] with a chiral crystal structure using neutron scattering and Lorentz transmission electron microscopy, respectively. In both systems skyrmions with diameters of about 20 and 90 nm, respectively, were induced by an external magnetic field out of a helical magnetic ground state. A spontaneous skyrmion-like phase was reported in MnSi in the vicinity of the helical transition temperature [134], however, the existence of a skyrmion lattice as the spontaneous *ground state* of a magnetic system has so far only been proposed theoretically [135].

6.2. Skyrmion lattice in the Fe ML on Ir(111)

6.2.1. Previous investigations of Fe/Ir(111)

Thin films of iron on the (111) surface of an iridium crystal have been studied already in the early 90's of the last century [136, 137]. These investigations concentrated on the structural as well as on the magnetic properties of the films. LEED measurements reveal that Fe films grow in the face centered tetragonal (fct) configuration for a thickness up to 5 AL, while for thicker films a phase transition towards a bcc structure occurs. Investigations of the magnetic properties show that the structural phase transition coincides with a change of the magnetic ordering. Using X-ray magnetic circular dichroism (XMCD) [138], a FM ordering was found for the bcc phase, while no dichroic signal was detected for thinner films indicating the absence of FM order [137]. However, the adsorption of circularly polarized light cannot distinguish between non-magnetic structures and magnetic structures which have no net magnetization, e.g. antiferromagnets or most non-collinear spin structures. Thus, SP-STM measurements were performed on this sample system to identify the magnetic structure of the Fe ML on Ir(111) [8, 9].

Fe deposited at room temperature on the clean Ir(111) surface (see Sec. 4.4.1) grows mostly on the terraces starting at the step edges of the next higher terrace (step-flow growth) but forms triangular islands as well, see Fig. 6.3 a. The islands appear flat in STM images reflecting the pseudomorphic growth of the first Fe layer which can either continue the fcc stacking of the Ir substrate or grow with a stacking fault in the hcp phase. The different stackings can easily be distinguished using STS [9]. In Fig. 6.3 b

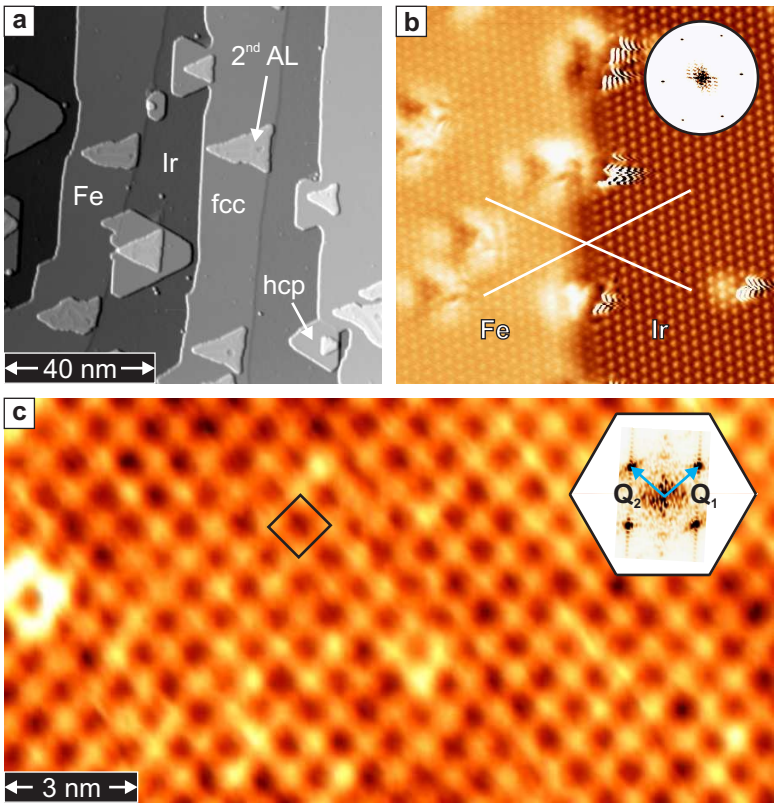

Figure 6.3: Growth of Fe on Ir(111) and first SP-STM measurements. **a**, Overview constant current STM image of ≈ 0.6 AL Fe on Ir(111) taken from Ref. [8]. Fe islands grow in the fcc as well as in the hcp stacking indicated by arrow ($U = +50\,\mathrm{mV}$, $I = 0.2\,\mathrm{nA}$, $T = 13\,\mathrm{K}$). **b**, Atomically resolved constant current image of the Fe ML grown from the step edge of the Ir substrate ($U = +5\,\mathrm{mV}$, $I = 30\,\mathrm{nA}$, $T = 8\,\mathrm{K}$). The white lines are on top of Ir atoms as well as Fe atoms, showing that the Fe ML continues the fcc stacking of the Ir surface. The inset shows the FT of the image which clearly shows the 6 spots corresponding to the hexagonal arrangement of the Ir and the Fe atoms. **c**, Constant current image SP-STM of the Fe ML with a tip sensitive to the out-of-plane component of the sample's magnetization ($U = +50\,\mathrm{mV}$, $I = 0.5\,\mathrm{nA}$, $T = 13\,\mathrm{K}$, $B = +2\,\mathrm{T}$). The image shows an almost square magnetic contrast which can also be seen by the two pairs of spots in the FT (inset).

an atomically resolved STM image of the Fe grown from the step edge of the Ir(111) substrate is shown. The Fe atoms continue the stacking of the Ir layer (marked by the lines) meaning that the Fe ML at the step edge grows in the fcc phase[1].

[1]For my thesis I concentrated on the magnetic properties of the fcc phase of the ML Fe. More information on the hcp phase of the ML as well as the second atomic layer can be found in Ref. [9].

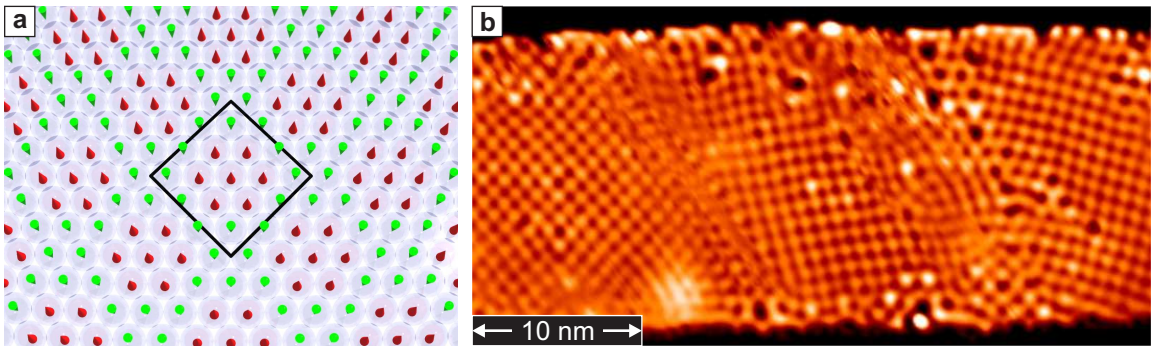

Figure 6.4: Proposed magnetic structure of the Fe ML on Ir(111). **a**, Top view of the mosaic structure proposed as the magnetic ground state in Ref. [8, 9]. Each atom and its magnetic moment is symbolized by a cone and the black lines indicate the magnetic unit cell. **b**, Constant current SP-STM image recorded with a tip sensitive to the out-of-plane component of the sample magnetization showing the three rotational domains of the magnetic structure of the Fe ML (taken from Ref. [8], $U = +50\,\mathrm{mV}$, $I = 0.25\,\mathrm{nA}$, $T = 13\,\mathrm{K}$, $B = +2\,\mathrm{T}$).

The fcc Fe ML, investigated by SP-STM with a tip sensitive to the out-of-plane direction, exhibits an almost square superstructure with $a \approx b \approx 1\,\mathrm{nm}$, see Fig. 6.3 c. Since the ML grows pseudomorphically and appears flat in STM images taken with a non-magnetic tip, this superstructure must be due to the magnetic structure of the Fe layer with bright and dark spots indicating opposite out-of-plane components of the sample magnetization. In addition to the measurements with an out-of-plane sensitive tip, measurements with an in-plane sensitive tip were reported in Ref. [8], which reveal no magnetic contrast. Therefore the magnetic ground state was proposed to be collinear – in first approximation – and by assuming a commensurate magnetic superstructure with respect to the underlying atomic lattice, its magnetic unit cell consists of 15 atoms. This so-called *mosaic* state is shown schematically in Fig. 6.4 a, with the magnetic moments of 7 atoms pointing up (↑) and the moments of the other 8 atoms pointing down (↓). This magnetic state would have an almost compensated magnetization which is consistent with XMCD measurements [137]. Due to the hexagonal arrangement of the Fe atoms and the (almost) square magnetic unit cell, the proposed mosaic state has three rotational domains, which can also be observed in the experiment, see Fig. 6.4 b.

Can the mosaic state be the magnetic ground state of the Fe ML on Ir(111)? Since each Fe atoms of the mosaic state has a different environment, e.g. one ↑-atom is surrounded by six ↑-neighbors while the other ↑-atoms have only three ↑-neighbors and three ↓-neighbors, the state is highly frustrated. This question was already discussed at the end of Ref. [8] and it was suggested by the authors that the mosaic state might

just be the collinear approximation of a more complex non-collinear state. However, the lack of magnetic contrast with an in-plane sensitive tip in Ref. [8] does not support a non-collinear magnetic ground state, which encouraged us to revisit the Fe ML on Ir(111).

6.2.2. Reexamination of the Fe ML on Ir(111) using SP-STM

Measurements with in-plane magnetized tips

Around the same time the first SP-STM investigations of the Fe ML on Ir(111) were published, it became apparent that the Dzyaloshinskii-Moriya interaction can play a crucial role in thin films on surfaces and drive these systems into a non-collinear magnetic ground state [15, 22]. Since the DM interaction is also crucial for the formation of magnetic skyrmions, see Sec. 6.1, it was speculated if the Fe ML on Ir(111) could be a candidate for a skyrmion lattice as the magnetic ground state [139]. Due to the lack of magnetic contrast with an in-plane magnetized tip, such a skyrmion lattice is not supported by the SP-STM measurements in Refs. [8, 9]. Therefore we performed new SP-STM measurements to check if the in-plane contrast is really absent or was just overlooked. We searched for a sample area showing all three rotational domains and investigated this area with an Fe-coated W tip. As described in Sec. 4.3 these tips are usually sensitive to the in-plane components of the sample magnetization, while the absolute direction of the tip magnetization is unknown.

Figure 6.5 a shows a quasi-3D constant current image of the Fe ML on Ir(111) measured with an in-plane sensitive magnetic tip. The Fe ML shows all three rotational domains which clearly exhibit a periodic magnetic contrast. By looking more closely on each of the three domains, Fig. 6.5 b - d, it becomes apparent that each of the domains shows a different contrast. While the domains shown in Fig. 6.5 c and d (domains II and III) exhibit a rather square structure with slight differences in the shape of the bright and dark areas, the domain in Fig. 6.5 b (domain I) shows a pattern with dark and bright stripes. The different contrasts on the three domains stem from the projections of the sample's in-plane magnetization components onto the tip magnetization, see Sec. 3.5. Since the tip magnetization is the same for all three domains we image different in-plane components of the magnetic structure of the Fe ML. In other words, the experiment shown in Fig. 6.5 is equivalent to an SP-STM measurement of *one* rotational domain with three different tips, whose magnetizations are rotated by 120° with respect to each other. The square structure of domains II and III has the same periodicity as the magnetic contrast observed with an out-of-plane magnetized tip, cf. Fig. 6.3 c. The stripes observed in domain I run along the sides of the square magnetic unit cell.

From these measurements we can definitely rule out the mosaic state as the magnetic ground state of the Fe ML on Ir(111), since we observe a magnetic contrast with an

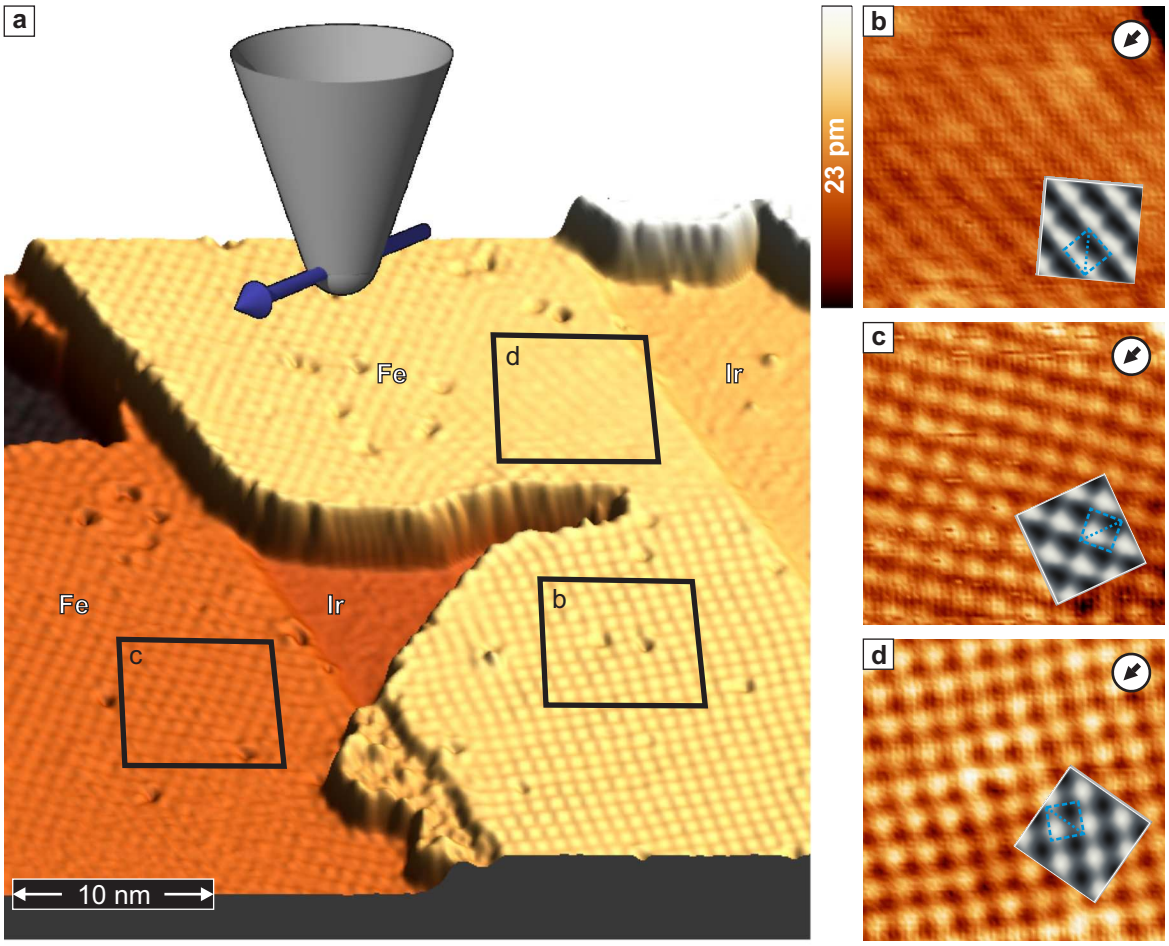

Figure 6.5: SP-STM measurements with a tip sensitive to the in-plane component of the sample magnetization. **a**, Quasi-3D plot of a constant current image of ≈ 0.8 ML of Fe on Ir(111) ($U = +5\,\mathrm{mV}$, $I = 0.2\,\mathrm{nA}$, $T = 8\,\mathrm{K}$, $B = 0\,\mathrm{T}$). The sample area exhibits all three rotational domains of the magnetic structure. **b** - **d**, Closer view of all three domains indicated by the insets in **a**. The insets show simulated SP-STM images (see pp. 80) with the magnetic unit cell marked by the blue lines.

in-plane magnetized tip[2]. More interesting than the exclusion of the mosaic state as the ground state of the Fe ML is the question: Can the different magnetic contrasts be explained by a lattice of skyrmions?

In the SP-STM experiments presented in Fig. 6.3 c and Fig. 6.5 b - d, we have measured the magnetization density of the Fe ML on Ir(111) projected onto four different

[2]On pp. 82 I will give a possible explanation why the in-plane contrast was not observed in the previous SP-STM studies.

directions with respect to the magnetic unit cell: the out-of-plane axis and three in-plane directions rotated by 120° with respect to each other. From this information we can construct the three-dimensional vector magnetization density using a procedure similar to C. L. Gao *et al.* [140, 141]. We know the magnetization component along one direction, defined by the tip magnetization, for each of the four measured sublattices, but we do not know their phase relation, since we could not measure them within the same sample area. Assuming a continuous vector magnetization density (in the vacuum) we can still narrow down the possible magnetic structures as shown in the following.

The SP-STM measurements on the three rotational domains with an in-plane magnetized tip are again displayed in the three panels of Fig. 6.6 a - c. Before constructing the three-dimensional vector magnetization we performed a unit cell averaging procedure as shown by insets in the lower right corner of each image. As stated above, the measurements with *one* tip on *three* rotational domains is equivalent to measurements with *three* tips on *one* domain. Therefore, we can rotate the unit cell averaged images to change from the tip magnetization reference frame (Fig. 6.6 a - c) to the magnetic unit cell reference frame in Fig. 6.6 d. In the top left, top right and bottom left corner of Fig. 6.6 d the three domains are displayed with one of the closed packed rows (one diagonal of the square magnetic unit cell) being horizontal. We indicate the in-plane magnetization direction by a color code as sketched by the chromatic circle, where the three in-plane magnetization directions probed in the experiment are given by the projection onto the tip magnetization, which is given by the black arrows. Domain I or sublattice I, displayed in the top left corner of Fig. 6.6 d shows stripes along the side of the square unit cell, with yellow and blue color for opposite sample magnetization components. The other two in-plane sublattices (II and III, bottom left and top right corner of Fig. 6.6 d) are square and measured with a tip magnetization that is rotated by ±120° with respect to that of sublattice I. The only way to create a continuous magnetization density from these three sublattices is to place the green of sublattice II and the red of sublattice III onto the position which was measured as yellow in sublattice I, since they all have parallel magnetization components (cf. the gradual mixing of I and II (III) at the left (top) of Fig. 6.6 d). This immediately locks the purple of sublattice II and the cyan of sublattice III onto the blue of sublattice I. In this way we have linked the three in-plane sublattices to form the backbone of the magnetic structure, which is shown in Fig. 6.6 d indicated by I+II+III. We still have a grid with a period of half of the magnetic unit cell vectors where the in-plane component is small, indicated by circles. These must be positions where the magnetic structure has either a large out-of-plane component or a cancellation of locally antiferromagnetically aligned in-plane components[3]. If we position our measurements of the

[3] We exclude the possibility of a vanishing magnetic moment, since we have to assume nearly constant magnetic moments for the Fe atoms due to large intra-atomic exchange.

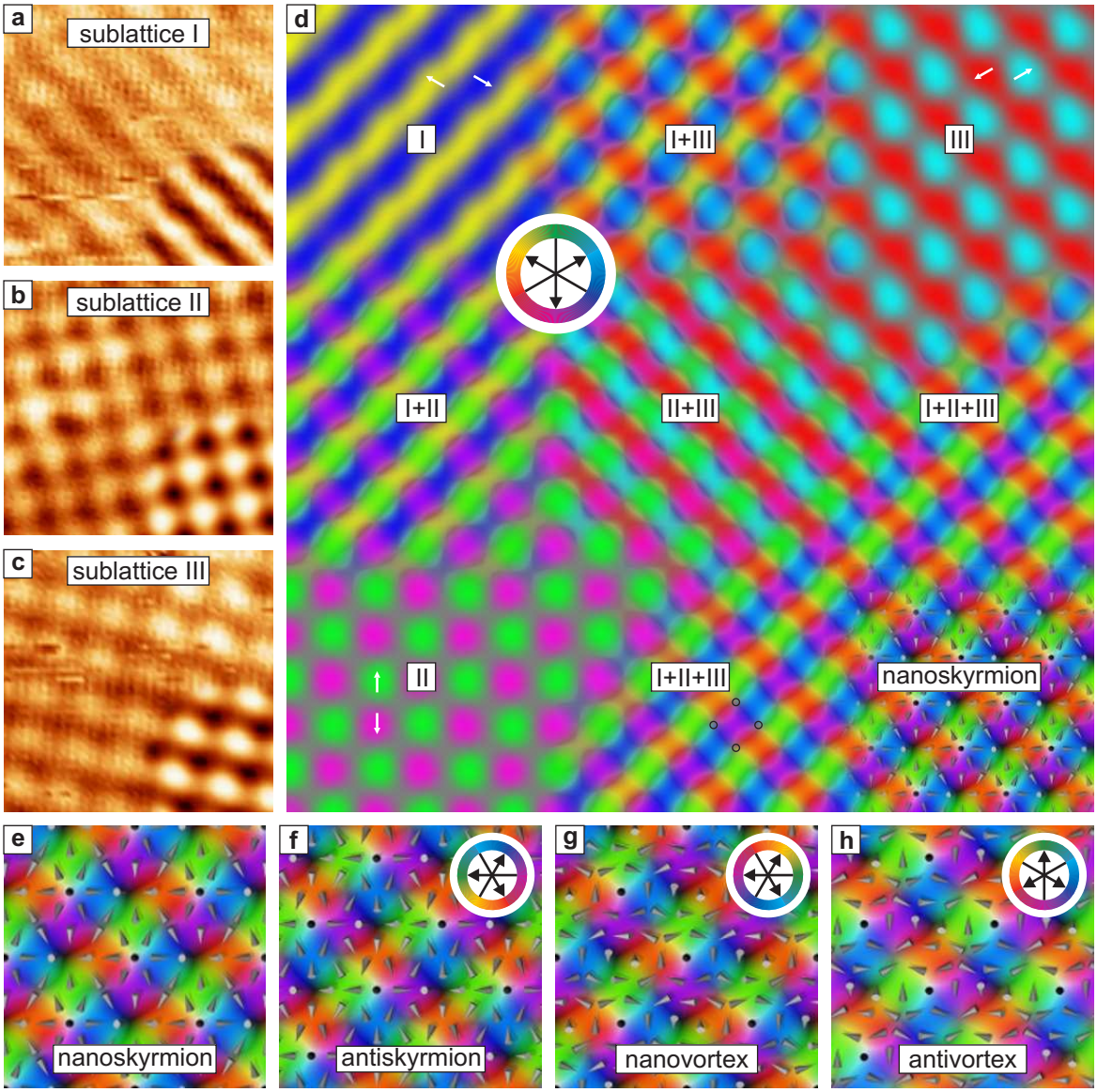

Figure 6.6: Vector magnetization density derived from the SP-STM measurements. **a**-**c**, SP-STM images of the three rotational domains (denoted sublattice I to III) obtained with an in-plane magnetized tip (data the same as in Fig. 6.5 b-d). Insets in the lower right corner show the images after unit cell averaging. **d**, Color-coded images and superposition of the three measured sublattices to derive the vector magnetization density of the sample (close to the Fermi energy). The color indicates the in-plane magnetization direction (see chromatic circle). In the lower right corner the determined vector magnetization density (including the out-of-plane component) is given in comparison with the spin structure of the skyrmion lattice. **e**-**h**, Comparison of the possible magnetic structures which could explain the vector magnetization derived from the SP-STM measurements.

out-of-plane magnetization (white and black for up and down, respectively) exactly onto one of these points we obtain the vector magnetization density shown in the bottom right of Fig. 6.6 d. Starting from the magnetic unit cell of the mosaic state (see Fig. 6.4), we can rotate each Fe atom's magnetic moment until its direction fits to this vector magnetization density. The spin structure we derive by this procedure is shown in the bottom right of Fig. 6.6 d, which resembles strongly a lattice of skyrmions, cf. Fig. 6.2 b, and it is called *nanoskyrmion* in the following (a zoom into the structure is shown in Fig. 6.6 e)[4].

With that construction of the vector magnetization density from the experimental data it is possible to show that an atomic-scale skyrmion lattice could be the magnetic ground state of the Fe ML on Ir(111). However, since we neither know the phase relation of the three in-plane components and the out-of-plane component nor the direction of the tip magnetization we still have some uncertainties in the evaluation of the data.

1. If the out-of-plane contrast is shifted by one half of the magnetic lattice constant along the side of the magnetic unit cell, the resulting structure looks like a lattice of antiskyrmions, see Fig 6.6 f. The skyrmion number of the magnetic unit cell of the antiskyrmion lattice is $S = -1$ (see Eq. 6.1), while the unit cell of the skyrmion lattice has the skyrmion number $S = +1$.

2. By rotating the in-plane components of the sample magnetization by 90° the magnetic structure shown in Fig. 6.6 g can be constructed. It is called nanovortex since the arrangement of the spins resembles the vortex in the center of a Landau pattern.

3. Combining the two points mentioned above, the structure would be a lattice of antivortices (Fig. 6.6 h). Similar to the (anti)skyrmion lattice the unit cell of the vortex and antivortex lattice have a skyrmion number of $S = +1$ and $S = -1$, respectively.

In conclusion, we cannot discriminate from these experiments if the magnetic ground state of the Fe ML on Ir(111) is a lattice of vortices, skyrmions or their counterparts. However, all of these proposed spin textures have in common, that they are topologically non-trivial with the magnetic unit cell having a skyrmion number of $S = \pm 1$.

[4] As I will show later, the magnetic superstructure is incommensurate to the atomic lattice. However, to keep the discussion of the magnetic structure as simple as possible, I will use the commensurate approximation with 15 atoms in the magnetic unit cell for the next sections and add the aspect of the incommensurability only at the very end.

Measurements with a defined in-plane direction of the tip magnetization

As can be seen in Fig. 6.6, it would be possible to exclude some of the proposed spin structures if the direction of the tip magnetization would be known. By applying an in-plane magnetic field, the tip magnetization can be aligned parallel to the surface, similar to the application of a magnetic field perpendicular to the surface to achieve out-of-plane contrast. This allows us to directly control the in-plane magnetization of the tip and we can therefore assign a certain magnetic contrast to a *known* in-plane component of the magnetization. An external magnetic field only influences the magnetization direction of the tip but does not alter the magnetic structure of the Fe ML, since this structure is completely compensated, i.e. the unit cell has no net magnetic moment. In our STM setup we can only apply magnetic fields perpendicular to the surface, see Sec. 4.2, and therefore we investigated the sample in a different STM setup, which allows to apply a magnetic field in a plane perpendicular to the sample, hence in one direction in the sample plane [142].

Before I will present those SP-STM measurements, I will shortly show how simulated SP-STM images, based on the spin-polarized Tersoff-Hamann model [143], help us to deduce the magnetic structure. In these simulations all surface atoms are considered to be chemically and electronically equivalent and their wave functions are approximated by s-orbitals (Tersoff-Hamann model, see Sec. 3.3). Therefore, the only contrast in the simulations is due to the relative angle between the tip and the sample magnetization[5]. The validity of the simulations can be demonstrated by comparing them to the measurements presented in the last section. The inset in Fig. 6.5 b shows a simulated SP-STM image of the nanoskyrmion lattice. By rotating the tip magnetization in the simulation we determined its direction – indicated by the arrow – for the best match between the simulated contrast and the experimental observation. After finding accordance between the simulation and the experiment we just rotated the tip magnetization in the simulation by $\pm 120°$ and compared the contrasts in the simulations to the other two rotational domains. This is shown in the insets in Fig. 6.5 c and d, and it can be seen that not only the square like contrast is reproduced but also the shape of the bright and dark spots is in excellent agreement to the experimental findings. Hence, we have additional evidence that the skyrmion lattice is the ground state of the Fe ML on Ir(111). However, these contrasts could also be explained by the other possible magnetic structures (see Fig. 6.6 f - h) only for a different tip magnetization direction.

In the additional measurements the magnetization direction of an Fe-coated W-tip is aligned along an in-plane magnetic field of $B = 1\,\mathrm{T}$ while the magnetic structure

[5]The simulation program is explained in detail in Ref. [143] and it has been shown in many publications that it can very accurately reproduce the magnetic contrasts in SP-STM measurements. The program has been extended by Prof. Dr. Stefan Heinze to simulate the contrast in conventional STM due to spin-orbit interaction as described in Sec. 6.2.3.

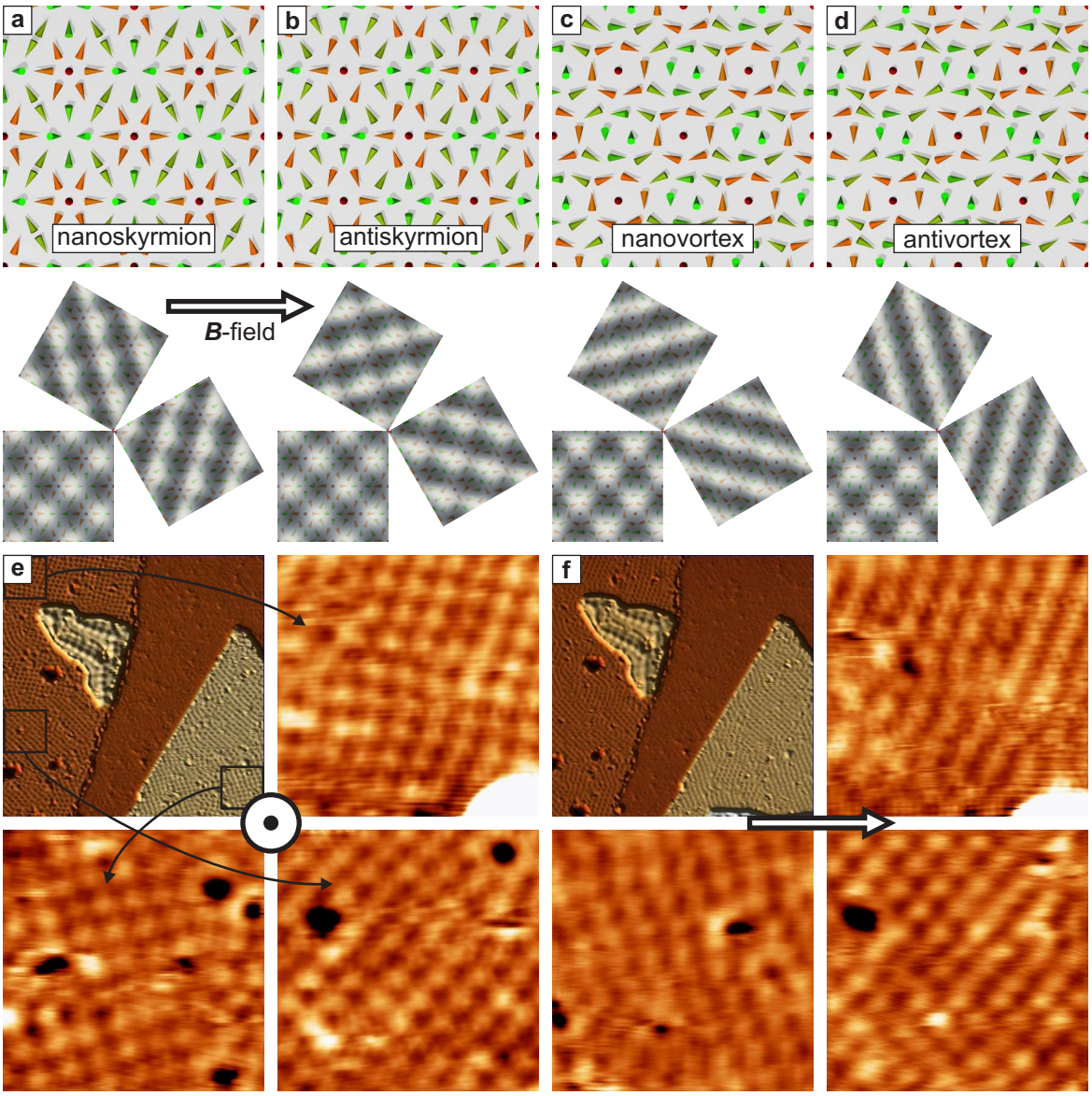

Figure 6.7: SP-STM measurements in an in-plane and out-of-plane magnetic field and comparison to simulated STM images. **a**, Schematic drawing of the spin structure of the skyrmion lattice. In the lower part the spin structure is superimposed with simulated SP-STM images showing the expected magnetic contrasts of the three rotational domains for a tip magnetization fixed along the arrow. **b** - **d**, The structure and magnetic contrasts for the antiskyrmion, vortex and antivortex lattice, respectively. **e** and **f**, SP-STM images of the three rotational domains with an out-of-plane and in-plane magnetized tip, respectively, as indicated by the arrow (tip magnetized along an external out-of-plane and in-plane magnetic field of $B = 1\,\mathrm{T}$). The top left images display a $50\,\mathrm{nm} \times 50\,\mathrm{nm}$ overview image while the other three images ($8\,\mathrm{nm} \times 8\,\mathrm{nm}$) show a closer view of the three rotational domains ($U = +50\,\mathrm{mV}$, $I = 0.5\,\mathrm{nA}$, $T = 6\,\mathrm{K}$).

of the sample remains unaffected since it does not have a net magnetic moment. For these measurements the sample was inserted into the STM with one of the closed packed rows along the in-plane magnetic field direction. Figure 6.7 a - d show schematic drawings of the four possible magnetic configurations presented in Fig. 6.6 e - h. The cones represent the direction of each Fe atom's magnetic moment while the color code indicates the z-component of the magnetization. The lower parts of each panel show the respective spin structure superimposed with the simulated magnetic contrast of the three rotational domains for the experimental configuration. The tip magnetization direction is given by the arrow, and the simulated SP-STM images demonstrate a difference between the four lattices, which makes them distinguishable by SP-STM measurements. For all spin configurations one rotational domain displays a square like contrast. While for the (anti)skyrmion lattice the two other domains show a mixture of square and stripe contrast, the (anti)vortex lattice shows a pure stripe contrast for the two domains. Most notably the stripes for the skyrmion and the antivortex lattice are almost perpendicular to the tip magnetization direction (magnetic field direction) while they are almost parallel in the case of an antiskyrmion or vortex lattice.

Figure 6.7 e and f show experimental data of a sample area exhibiting all three rotational domains imaged with an out-of-plane magnetized tip, i.e. in an external magnetic field normal to the sample surface (Fig. 6.7 e), and with an in-plane magnetized tip, i.e. in an external in-plane magnetic field (Fig. 6.7 f). For the out-of-plane magnetized tip all three rotational domains show a square like contrast which is in accordance to the previous publications [8, 9], see also Fig. 6.4. With an external in-plane magnetic field, one domain appears with a square-like contrast while the other two rotational domains show a mixed contrast of stripes and squares with the stripes almost perpendicular to the direction of the applied field. By comparing the experimental data to the simulated SP-STM images we can definitely exclude the antiskyrmion and vortex state since the direction of the stripes in the experiment do not match the direction in the simulated images. The direction of the stripes of the antivortex lattice match the experimental data, however, the internal structure of the stripes does not fit well, see Fig. 6.7 d. Only the simulated SP-STM images of the nanoskyrmion lattice match all experimental contrasts and therefore, we can identify the skyrmion lattice as the ground state of the Fe ML on Ir(111).

Possible explanation for the missing in-plane contrast in previous measurements

While the same out-of-plane magnetic superstructure was reported in the previous publications no magnetic signal was found for measurements with an Fe-coated tip sensitive to the in-plane components [8, 9]. Therefore the measurements were interpreted as the aforementioned mosaic state as the magnetic ground state. This interpretation of the data needs to be revised in the light of the measurements and simulations presented above and I will give some evidence why the in-plane component

was not detected in the first SP-STM measurements.

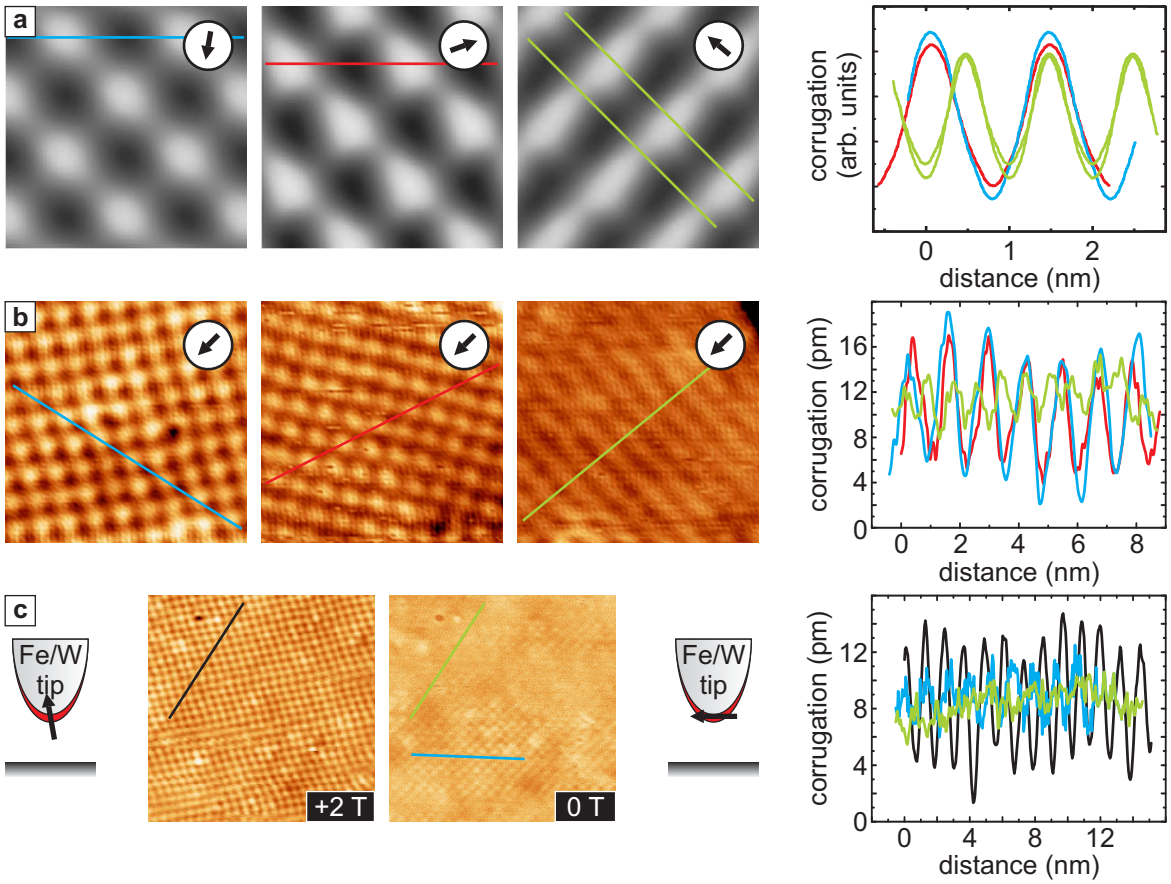

Figure 6.8: Experimentally observed corrugation variations for different tip magnetization. **a** and **b**, Simulated and experimental (raw data) SP-STM images with an in-plane magnetized tip identical to the ones in Fig. 6.5 b - d and profiles along the indicated lines. The tip magnetization direction is shown in the insets. **c**, SP-STM images from a previous measurement, cf. Ref. [8] with a tip sensitive to the out-of-plane (left, $B = +2\,\mathrm{T}$) and the in-plane (right, $B = 0\,\mathrm{T}$) component of magnetization (note that a different rotational domain has moved into the area) and corresponding line profiles ($U = +50\,\mathrm{mV}$, $I = 0.5\,\mathrm{nA}$, $T = 13\,\mathrm{K}$).

When using Fe-coated tips at $B_z = 0\,\mathrm{T}$, which are typically sensitive to the in-plane component of magnetization, many times a faint square magnetic superstructure was observed also in the earlier measurements [144]. However, the corrugation with an out-of-plane sensitive tip (Fe-coated tip at $B_z \geq 2\,\mathrm{T}$) is typically much larger. Previously, the authors came to the conclusion, that at $B_z = 0\,\mathrm{T}$ the tip magnetization is not completely in the sample surface plane but slightly canted, thereby catching some of the out-of-plane magnetization components. As we know now, this is not

necessarily the case, since also with an in-plane sensitive tip the observation of a square magnetic unit cell is likely (see Figs. 6.5, 6.6 and 6.7); in fact, the simulation of SP-STM images for the skyrmion lattice shows that nearly 80 % of all possible in-plane tip magnetizations yield a square magnetic superstructure, while only 20 % show clear indications of stripes. Figure 6.8 a shows again the simulated SP-STM images of Fig. 6.5 b - d, not rotated and with identical gray-scales to allow a direct comparison. The right panel shows the profiles along the indicated line sections. It can be seen that the square magnetic superstructures have a slightly but distinctively larger corrugation compared to the stripe pattern. Figure 6.8 b shows SP-STM images of the three different rotational domains of Fig. 6.5 a which is the same data as in Fig. 6.8 b - d. Again to the right the corresponding line sections are shown. Qualitatively, the line sections of the simulated and measured SP-STM images display the same trend of a smaller corrugation amplitude for the stripe pattern as compared to that of the square lattice. A quantitative analysis of the data shows that the corrugation of the stripe pattern ($\approx 4\,\mathrm{pm}$) is almost a factor of 3 smaller than the corrugation of the square pattern ($\approx 10 \ldots 12\,\mathrm{pm}$), making the stripe pattern much more difficult to resolve. This quantitative deviation from the simulated images may be contained in the simplicity of the model neglecting e.g. the bias voltage and possible inelastic effects.

In Fig. 6.8 c data from the old measurements is revisited, showing a sample area measured with an out-of-plane and an in-plane sensitive tip. While with the tip sensitive to the out-of-plane component of magnetization (left, $B_z > 0\,\mathrm{T}$) the single domain square magnetic superstructure is dominant in the whole area, the measurement with the tip magnetization in the plane (right, $B = 0\,\mathrm{T}$) shows some areas with very weak and other areas with no magnetic superstructure. This is due to the fact that a second rotational domain has moved into the bottom of the scan area, which can be seen by the rotation of the faint square pattern with respect to the out-of-plane measurement. The corrugation of the square pattern in the in-plane measurement is only $\approx 4\,\mathrm{pm}$ (blue line), meaning that the spin-polarization of the tip is considerably smaller than the polarization of the tip used in the new measurements (Fig. 6.8 b). Using the quantitative analysis from Fig. 6.8 b the stripe pattern would have a corrugation of only 1 to 1.5 pm, which is at the resolution limit of the instrument and can explain the areas of the scan region showing no magnetic contrast (green line).

6.2.3. Proof of incommensurability employing TAMR

The Fourier transformation (FT) of the SP-STM image in Fig. 6.4 b shows two pairs of spots which we can directly assign to the square magnetic unit cell of the skyrmion lattice. The spots are given by two vectors $\mathbf{Q}_1$ and $\mathbf{Q}_2$ which span the reciprocal magnetic unit cell in the k-space. In the commensurate approximation these vectors have a length of $|\mathbf{Q}_1| = |\mathbf{Q}_2| = 0.277 \times 2\pi/a$ and include an angle of $\theta = 92.2°$ where $a =$

2.72 Å is the next nearest neighbor distance given by the Ir surface. When the skyrmion lattice is measured at bias voltages close to the Fermi energy, we observe spots in the FT of the SP-STM images in addition to the 4 spots corresponding to the magnetic unit cell ($\mathbf{Q}_1$ and $\mathbf{Q}_2$). Figure 6.9 a - c and d - f show SP-STM measurements of the

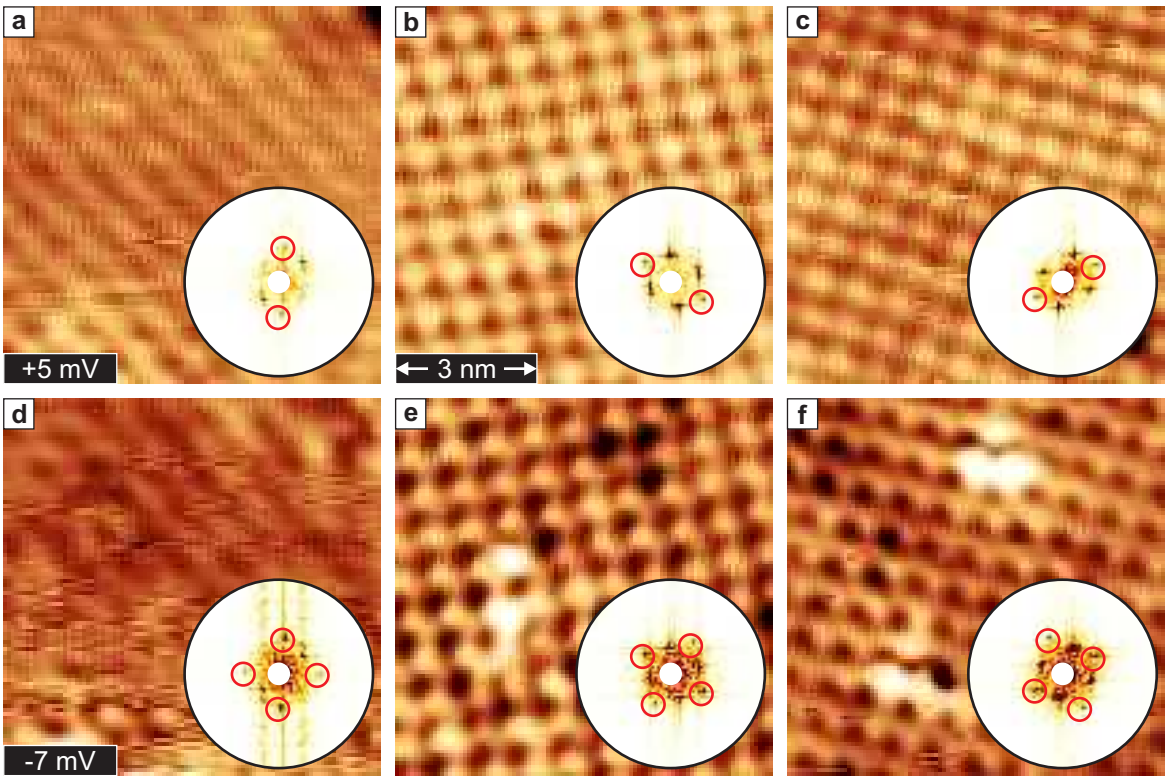

Figure 6.9: SP-STM measurements of the same sample area as in Fig. 6.5 at low bias voltages. **a - c**, Constant current images of the three rotational domains with the respective FT for $U = +5\,\mathrm{mV}$. **d - f**, Same domains imaged at $U = -7\,\mathrm{mV}$. The insets show the respective FT of the SP-STM image with the red circles marking additional spots, which are not due to the magnetic unit cell ($I = 0.2\,\mathrm{nA}$, $T = 8\,\mathrm{K}$).

same three domains as in Fig. 6.5 at bias voltages of $U = +5\,\mathrm{mV}$ and $U = -7\,\mathrm{mV}$, respectively. The insets show the corresponding FTs, which exhibit an additional pair of spots for $U = +5\,\mathrm{mV}$ and two additional pairs of spots for $U = -7\,\mathrm{mV}$. Since the number of spots varies for different voltages and the spots rotate accordingly to the rotation of the magnetic domain, we exclude the possibility of a measurement or tip-related artifact. The additional spots are linear combinations ($\mathbf{Q}_1 \pm \mathbf{Q}_2$) of those related to the magnetic unit cell and correspond in real space to a unit cell half the size of the magnetic unit cell. This suggests they might be caused by spin-orbit interaction, which leads to the tunneling anisotropic magnetoresistance (TAMR).

Due to its electronic nature the TAMR is also observable in STM experiments with non-magnetic tips. The simulated spin-averaged STM images of the skyrmion lattice in Fig. 6.10 a and b assume a different dependence of the Fe atoms' local density of states (LDOS) on the two perpendicular in-plane directions of the local magnetic moment and by this mimic the effect of spin-orbit coupling on the electronic structure[6]. The FT in Fig. 6.10 a clearly shows the hexagonal spots corresponding to the atomic lattice and in addition the four spots that were observed for the experimental data in Fig. 6.9 d - f. For the simulated STM image in Fig. 6.10 b, in which an LDOS modulation proportional to the perpendicular magnetization component is assumed, only two spots show up. To experimentally disentangle the contributions from the spin-polarized current and the effect of spin-orbit coupling in the measurements we imaged the skyrmion lattice with a W tip at low bias voltages. Figure 6.10 c and d show STM images of the same sample area at two different bias voltages, which display not only the atomic lattice but also a superstructure due to the TAMR[7]. One can clearly see a square-shaped and a uniaxial superstructure in agreement with the simulations of Fig. 6.10 a and b. The FTs of the STM images (insets) contain the spots corresponding to the atomic lattice as well as the additional spots, showing that the assumption of the spin-orbit coupling effect is in excellent agreement with the experiment.

Figure 6.10 e displays the (rotated) FT of the experimental STM image of Fig. 6.10 c overlaid with the FT of the simulated image of Fig. 6.10 a. A comparison reveals that the spots originating from the spin-orbit coupling effect – and thus the magnetic period – do not exactly coincide between experimental data and simulation. This demonstrates that the magnetic unit cell is not strictly commensurate with the atomic lattice, but rather 10 % compressed compared to Fig. 6.6 e leading to an incommensurate magnetic skyrmion lattice, shown in Fig. 6.10 f. The simulated STM images (insets of Fig. 6.10 f obtained in a similar way as for Fig. 6.10 a and b) are in good agreement with the experimental images confirming the proposed incommensurate skyrmion lattice.

[6] In the simulations the LDOS of the surface atoms ρ^{S}, see Sec. 3.3 and Eq. 3.9, is substituted by $\rho^{\mathrm{S}} + \Delta\rho_\alpha$, where $\Delta\rho_\alpha$ represents the modulation of the LDOS of atom α. The angle dependence of the modulation Δn_α arises from the angular dependent part of the matrix element $M_{\mu\nu}$ (Eq. 3.7) due to SOC. Depending on the applied bias voltage, U, different contributions to the LDOS may dominate the tunnel current and therefore the modulation of the LDOS may also stem from different d-orbitals that result in a bias-voltage dependent change of the angle dependence of $\Delta n_\alpha(U)$. In contrast to spin-polarized STM where the magnetic signal depends on the cosine of the angle between the magnetization direction of the tip and the Fe atom at site $\mathbf{R}_\alpha$, the spin-orbit caused TAMR contrast is proportional to the square of the cosine of the angle between the magnetization direction of the Fe atoms and the lattice vectors of the substrate.

[7] These additional modulations due to the effects of spin-orbit interaction should not be confused with a structural reconfiguration of the Fe atoms. As it has been shown in Fig. 6.3 b, the Fe ML grows perfectly pseudomorphic on the Ir(111) surface forming a flat and homogeneous overlayer.

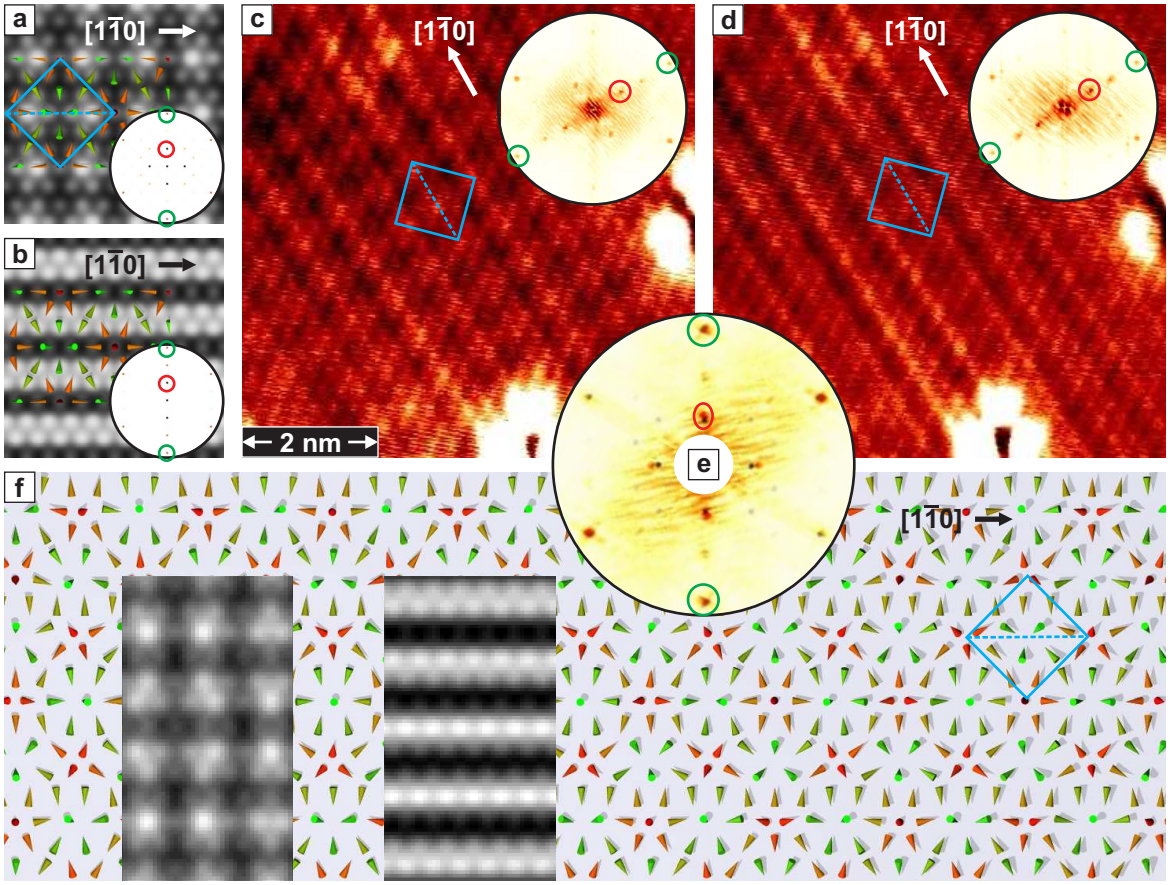

Figure 6.10: Additional contrast in STM images due to the spin-orbit interaction. **a** and **b**, Simulated STM images of the skyrmion lattice assuming a different dependence of the LDOS on the direction of the magnetic moments. In **a** the modulation is proportional to the square of the x-component of the local magnetization (horizontal) and in **b** it is proportional to the absolute square of the y-component. The simulations are superimposed by the spin structure of the skyrmion lattice. **c** and **d**, STM measurements with a non-magnetic tip showing different periodic variations in height due to the TAMR ($U = +5\,\mathrm{mV}$ and $U = -5\,\mathrm{mV}$, respectively, $I = 2\,\mathrm{nA}$, $T = 8\,\mathrm{K}$). The insets of **a** - **d** show the FT corresponding to the respective image with the spots corresponding to the atomic lattice marked by green circles and the spots caused by SOI indicated with red circles. The magnetic unit cell is marked by blue lines. **e**, Comparison of the FTs of the experimental (**c**) and the simulated STM image (**a**) revealing that the skyrmion lattice is incommensurate with the atomic lattice (red ellipse). **f**, Schematic drawing of the incommensurate magnetic skyrmion lattice. The insets show simulated STM images similar to **a** and **b**.

6.2.4. Physical origin of the skyrmion lattice

Extended Heisenberg model

To understand the microscopic origin of the skyrmion lattice as the magnetic ground state of the Fe ML on Ir(111) we investigate the magnetic phase space employing an extended two-dimensional Heisenberg model

$$E_{\text{tot}} = E_{\text{exch}} + E_{\text{4spin}} + E_{\text{DM}} + E_{\text{bi}} + E_{\text{ani}}. \tag{6.3}$$

In this Hamiltonian the first term represents the Heisenberg exchange (see Sec. 2.1) between the Fe atoms' magnetic moments $\mathbf{M}_i$ with the coupling strength J_{ij}. The second term describes the four-spin interaction, which occurs due to electron hopping between four lattice sites (see Sec. 2.3). For the model Hamiltonian we only consider nearest neighbor four-spin interaction, whose strength is given by the coupling constant K_4. The third term is the Dzyaloshinskii-Moriya interaction, which is characterized by the DM vector $\mathbf{D}_{ij}$, see Sec. 2.2.2. The direction of $\mathbf{D}_{ij}$ can be determined from symmetry considerations [17, 22], and at surfaces it lies predominantly in the surface plane, see also Sec. 5.3.1. The last two terms represent the biquadratic exchange energy and the magnetocrystalline anisotropy energy, see Sec. 2.3 and Sec. 2.2.1. As I will show later, these two energy contributions are rather small, hence they are neglected in the following to simplify the discussion.

To study the influence of the different magnetic interactions on the observed nanoskyrmion lattice we construct an analytic solution to the model in Eq. 6.3. From the experiment, we observe that the magnetic structure is characterized by four spots in the reciprocal space, see Fig. 6.3 c. Each pair of reciprocal lattice vectors, $\pm\mathbf{Q}_i$, corresponds to a single spin spiral, which is the general solution of the Heisenberg model on a periodic lattice, see Sec. 2.1. Since the Heisenberg model is isotropic in space, the energy of a single spin spiral is degenerate with any superposition of spin spirals or multi-$\mathbf{Q}$ state. Hence, the occurrence of a two-dimensional magnetic lattice as observed for the Fe ML cannot be explained only by the Heisenberg exchange.

This is where the four-spin interaction comes into play. It can couple spin spirals and thereby lift the energy degeneracy of the resulting superposition state with respect to a single spin spiral. In order to prevent a large loss of intra-atomic exchange energy constant magnetic moments are required at all sites. With the vectors $\mathbf{Q}_1$ and $\mathbf{Q}_2$ from the FT of the experimentally observed magnetic structure, see Fig. 6.3 c we can construct such a multi-$\mathbf{Q}$ state in which the magnetic moment $\mathbf{M}_i$ at the position $\mathbf{R}_i$ is given by

$$\mathbf{M}_i = M \begin{pmatrix} \sin(\varphi_i) \\ \cos(\varphi_i)\sin(\vartheta_i) \\ \cos(\varphi_i)\cos(\vartheta_i) \end{pmatrix} \tag{6.4}$$

with $\varphi_i = (\mathbf{Q}_1 + \mathbf{Q}_2) \cdot \mathbf{R}_i/2$ and $\vartheta_i = (\mathbf{Q}_1 - \mathbf{Q}_2) \cdot \mathbf{R}_i/2$. This multi-$\mathbf{Q}$ state is characterized by the length $Q = |\mathbf{Q}_1| = |\mathbf{Q}_2|$ and the opening angle θ between the two symmetry equivalent vectors $\mathbf{Q}_1$ and $\mathbf{Q}_2$, and it consists of an equal number of skyrmions ($S = +1$) and antiskyrmions ($S = -1$). This multi-$\mathbf{Q}$ state can be transformed into the skyrmion lattice shown in Fig. 6.6 e by replacing all antiskyrmions with skyrmions, which leads to an energetically more favorable state as shown later. This transformation can be included in the analytical form of the magnetic structure, Eq. 6.4, by multiplying the x-component of $\mathbf{M}_i$ with the factor:

$$\cos((\mathbf{Q}_1 - \mathbf{Q}_2) \cdot \mathbf{R}_i)/|\cos((\mathbf{Q}_1 - \mathbf{Q}_2) \cdot \mathbf{R}_i)|.$$

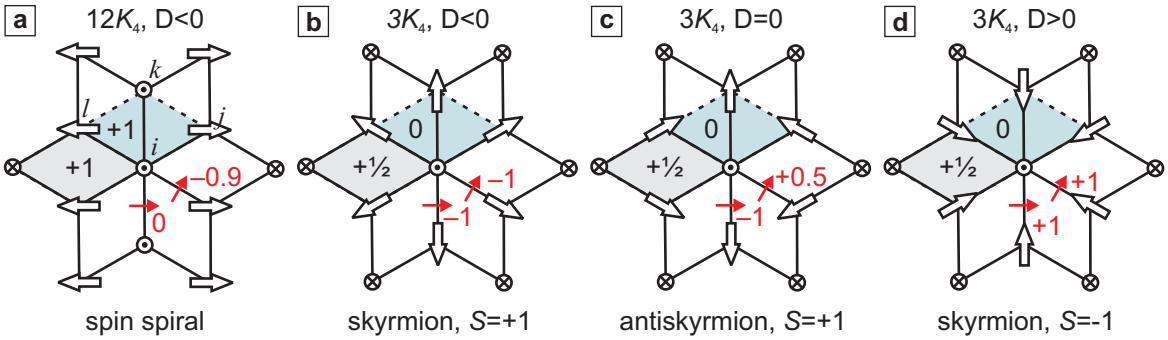

Figure 6.11: Schematic drawings of a spin spiral and skyrmions of different rotational sense and topological index S. **a**, 90° spin spiral ($S = 0$), **b**, clockwise skyrmion ($S = +1$), **c**, antiskyrmion ($S = -1$) and **d**, counterclockwise skyrmion ($S = +1$). The size and sign of the four-spin term is indicated by black numbers for different diamonds (shaded areas) consisting of four adjacent lattice sites ($ijkl$). The in-plane projection of the DM vector which couples spins on adjacent sites is also given by red arrows for pairs of nearest neighbors. The value of the DM term is indicated by red numbers.

The origin of the energy gain due to the four-spin interaction of a skyrmion or antiskyrmion with respect to a single spin spiral can be understood from the sketches in Fig. 6.11. In each sketch there are 12 diamonds consisting of four adjacent lattice sites ($ijkl$) which contribute to the four-spin interaction. As indicated in Fig. 6.11 a, there are two different types of diamonds for a 90° spin spiral which both contribute with a value of $-K_4$, i.e. from the twelve diamonds we obtain in total $E_{\text{spiral}} = -12\,K_4$, which holds for all planar spin spirals. For a skyrmion or antiskyrmion, shown in Fig. 6.11 b - d, the two different types of diamonds contribute with $1/2\,K_4$ and 0, and the total energy due to four-spin interaction is $E_{\text{sky/anti}} = -3\,K_4$. For the Fe ML on Ir(111), we find $K_4 < 0$ from the first-principles calculations, see p. 90, and therefore both, a skyrmion or an antiskyrmion, gain an energy of $E_{\text{sky/anti}} - E_{\text{spiral}} = 9\,K_4$ with respect to the spin spiral.

While the four-spin interaction does not distinguish between skyrmions and antiskyrmions, the DM interaction favors skyrmions with a unique rotational sense over antiskyrmions. For a skyrmion, the vector product $(\mathbf{M}_i \times \mathbf{M}_j)$ is parallel to the in-plane projection of $\mathbf{D}$ for all neighbors of the central moment (Fig. 6.11 b and d) leading to a large E_{DM} compared to the antiskyrmion (Fig. 6.11 c). The sign of $\mathbf{D}$ selects skyrmions with a unique rotational sense, i.e. whether an up-pointing moment with outward rotating neighbors (Fig. 6.11 b) or with inward rotating neighbors (Fig. 6.11 d) has the lower energy.

DFT calculations

For a quantitative application of this extended Heisenberg model (see eq. 6.3) to the Fe ML on Ir(111), all parameters such as the exchange constants J_{ij}, the four-spin interaction K_4, the biquadratic term B, the anisotropy constant K and the DM vector $\mathbf{D}$ were obtained from first-principles calculations using the `FLEUR` code [108]. For the density functional theory (DFT) calculations, performed by Dr. Gustav Bihlmayer from the Forschungszentrum Jülich and Prof. Dr. Stefan Heinze from the University of Kiel, the 15 Fe atoms of the magnetic unit cell supported by 4 layers of the Ir(111) surface were considered, resulting in a huge unit cell consisting of 75 atoms. While the structural relaxations of the system have been performed in the generalized-gradient approximation (GGA) of the exchange correlation potential [145], the energy differences between magnetic configurations have been calculated in the local-density approximation (LDA) [146]. The effects of the spin-orbit interaction are included in second-order perturbation theory.

The exchange constants J_{ij} have been calculated up to 8 nearest neighbors by fitting the energy dispersion of spin spirals along the high-symmetry direction $\overline{\Gamma} - \overline{\mathrm{K}} - \overline{\mathrm{M}}$ of the 2D Brillouin zone. The values are given in Table 6.1. The exchange energy still favors a FM ground state and it is dominated by J_1, however, the other exchange constants lead to a slow rise of $E(\mathbf{Q})$ in the vicinity of the FM state ($\mathbf{Q} = 0$). This means, that interactions, which are usually neglected since they are much smaller than the Heisenberg exchange, will play crucial roles for the magnetic ground state of the Fe ML on Ir(111).

We assume the direction of $\mathbf{D}$ for two nearest-neighbor Fe atoms according to the Fert-Lévy mechanism of the DM interaction [21]. The strength of the DM interaction has been calculated directly from the energy difference of the nanoskyrmion lattice and the corresponding antiskyrmion lattice ($\Delta E = 2.8\, D$), i.e. from non-collinear magnetic calculations with 75 atoms including spin-orbit coupling. The nanoskyrmion lattice, which has the lowest total energy among all states we calculated within DFT, is by 6.7 meV/Fe atom lower in total energy than the ferromagnetic state (see Table 6.2). The antiskyrmion lattice (obtained from the multi-$\mathbf{Q}$ state by using the scissor operation to cut out the patches with $S = -1$) is only by 1.7 meV/Fe atom

constant	J_1	J_2	J_3	J_4	J_5	J_6	J_7	J_8
value (meV)	+5.7	-0.84	-1.45	-0.06	+0.2	+0.2	-0.2	+0.5
constant	D	K_4	B	K				
value (meV)	-1.8	-1.05	-0.2	-0.8				

Table 6.1: Parameters for the extended Heisenberg model extracted from the DFT calculations. All energy values are given per Fe atom.

lower than the ferromagnetic state. From these energies we obtain an absolute value of the nearest-neighbor DM interaction of $D = -1.8\,\text{meV}$. The negative sign implies that a clockwise magnetic rotation (Fig. 6.11 b) has a lower energy than a counterclockwise one (Fig. 6.11 c). The magneto-crystalline anisotropy constant has been calculated from comparison between the in-plane and out-of-plane ferromagnetic solution and a value of $K = -0.8\,\text{meV}$ has been obtained, with a minus sign denoting an easy out-of-plane magnetization direction.

To determine the strength of the four-spin and the biquadratic interaction for nearest neighbors we have varied them to optimally reproduce the total energy differences of all magnetic states of Table 6.2 (four different collinear magnetic structures, and two non-collinear states). The extraction of the four-spin and the biquadratic interaction is possible due to the fact that energy differences beyond Heisenberg exchange interaction, DM interaction, and magneto-crystalline anisotropy can be accounted for only by higher-order terms (for the collinear states there are additional smaller terms due to spin-polarization induced in the Ir substrate). The values we find are $K_4 = -1.05\,\text{meV}$ and $B = -0.2\,\text{meV}$.

To check how well this set of parameters reproduces the total energy DFT results obtained by means of the FLEUR code, we compare the total energy differences with those obtained from the Hamiltonian of the extended Heisenberg model. Both values are shown in Table 6.2 and the energies are given in meV/Fe atom with respect to the ferromagnetic (FM) reference state. We attribute the remaining energy differences to our approximation of the real system by an effective two-dimensional Heisenberg model.

Investigation of the magnetic phase space

To analyze the role of the exchange, four-spin, and DM interaction in the phase space of skyrmion lattices we study the energy landscape by varying Q and θ. While the exchange energy shows a very shallow minimum for $Q < 0.2 \times 2\pi/a$ and is nearly independent of θ, see Fig. 6.12 b, the four-spin interaction depends strongly on both

State	DFT (meV/atom)	model (meV/atom)
FM	0.0	0.0
mosaic	+1.9	+1.7
(4:11)	-3.7	-2.7
↑↑↓↓	-5.9	-4.1
antiskyrmion	-1.7	-2.0
nanoskyrmion	**-6.7**	**-7.0**

Table 6.2: Comparison between energies for different states derived from DFT calculations and from the extended Heisenberg model. The (4:11) state is similar to the mosaic state only with four ↑-atoms and 11 ↓-atoms in the magnetic unit cell. The ↑↑↓↓ state is similar to a row-wise AFM state with two rows of ↑-atoms and two rows of ↓-atoms.

Q and θ of the nanoskyrmion as apparent from the polar plot in Fig. 6.12 c. The four-spin energy is minimized for an angle of $\theta = 90°$ and a value of $Q \approx 0.4 \times 2\pi/a$. The energy contributions due to exchange and four-spin interaction are of the same order and their sum also displays a minimum for an angle of $\theta = 90°$ between $\mathbf{Q}_1$ and $\mathbf{Q}_2$. Therefore, the four-spin interaction is the microscopic origin of the square symmetry of the observed magnetic structure. Fig. 6.12 d shows the relevant energy contributions for the nanoskyrmion lattices with $\theta = 90°$ (along the dashed lines in Fig. 6.12 b and c) as a function of Q. The competition between rising exchange energy and decreasing four-spin energy with Q determines the energetic minimum E_{min} to a value of $Q_{\mathrm{min}} \approx 0.27 \times 2\pi/a$, very close to the experimental finding.

In Fig. 6.12 e and f plots of the energy contributions of the different interactions are shown in dependence of Q for a single- and the multi-$\mathbf{Q}$ state. By comparing Fig. 6.12 d - f, the gain in DM energy is largest and also the rise of exchange towards the AFM state is slowest for a single spin spiral. On the other hand, the four-spin interaction shows no dispersion in dependence of Q for a single spin spiral, while the gain in energy for the multi-$\mathbf{Q}$ state is comparable to the skyrmion lattice. For each kind of non-collinear state we can extract a Q which corresponds to the lowest energy (see also dashed lines in Fig. 6.12 d - f). These lowest energy states are compared in Figure 6.12 g. From this plot it becomes apparent that the four-spin interaction plays the crucial role to couple different spin spirals into a two-dimensional magnetic structure, but the DM interaction makes the difference between an (anti)skyrmion and an (anti)vortex lattice or a multi-$\mathbf{Q}$ state. Although the four-spin term is small compared to pair-wise exchange interactions in typical magnets, here, it can compete with the exchange energy as the nearest-neighbor ferromagnetic exchange coupling is unusually small for Fe on an Ir surface due to the strong Fe-Ir hybridization.

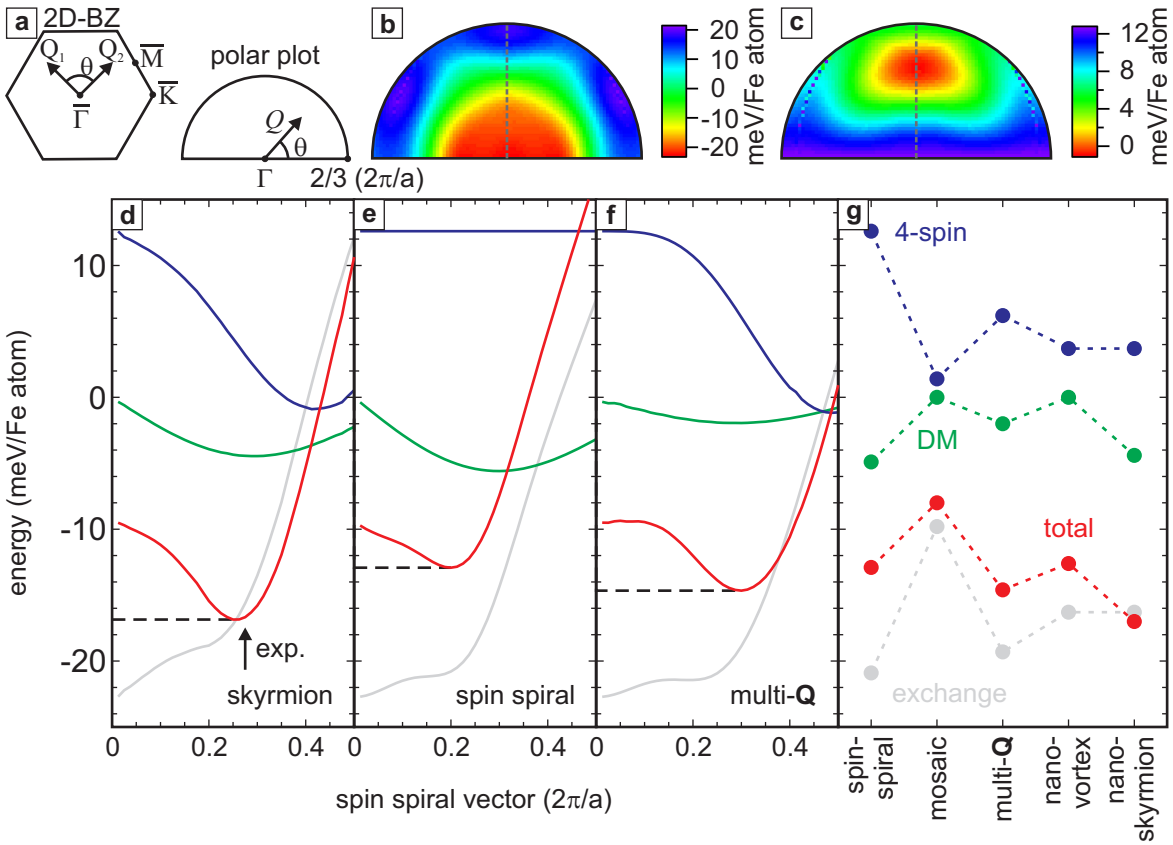

Figure 6.12: Contributions to the energy due to the different interactions. **a**, Scheme of the two-dimensional Brillouin zone and explanation of the polar plots in **b** and **c**. **b**, Plot of the Heisenberg exchange energy in dependence of Q and θ (color scale indicates the energy in meV/Fe atom). **c**, Plot of the 4-spin interaction, similar to **b**. **d** - **f**, Energy contributions for $\theta = 90°$ in dependence of Q for the skyrmion lattice, a single- and multi-**Q** state, respectively. **g**, Comparison of the respective lowest energy state of the spin spiral, mosaic, multi-**Q**, vortex and skyrmion state.

6.3. Summary

The Fe ML on the Ir(111) surface exhibits an almost quadratic magnetic superstructure which has three rotational domains. Measurements of all three domains with the same tip magnetization direction allow the construction of the Fe layer's magnetization density, which can only be explained by a complex, topologically non-trivial magnetic structure. Comparison of the measurements to simulated SP-STM images reveal a lattice of magnetic skyrmions as the ground state of the Fe layer. Due to its non-collinearity, the skyrmion lattice gives rise to a periodic modulation of the electronic density when imaged with non-magnetic tips. STM measurements with simultaneous

atomic resolution reveal that the skyrmion lattice is incommensurate to the hexagonal surface, meaning that the magnetic structure is almost completely decoupled from the atomic lattice. The formation of the skyrmion lattice in the Fe ML on the Ir(111) surface is explained by weak Heisenberg exchange in combination with the four-spin and the DM interaction.

7. Summary and outlook

In the framework of this thesis I conducted SP-STM and -STS measurements on Fe nanostructures grown on two different surfaces of an Ir single crystal. In combination with first principles calculations and simulations the complex, non-collinear magnetic ground states of both sample systems could be unambiguously identified. The Fe chains on the (5×1)-reconstructed (001) surface have a spin spiral ground state with a unique rotational sense, and the first atomic layer of Fe on the (111) surface, whose atoms are arranged hexagonally, incorporates an almost square lattice of magnetic skyrmions. For both sample systems not only the qualitative but also the quantitative agreement of the SP-STM measurements and the DFT calculations is excellent, since the observed periodicities of both magnetic structures could be reproduced. Both ground states are enabled by extremely weak Heisenberg exchange which opens the door for other, usually neglected interactions to become important. In the case of the Fe ML, the four-spin interaction in combination with the DM interaction are the driving forces behind the formation of the skyrmion lattice, while beyond-nearest neighbor DM interaction has to be considered to describe the spin spiral in the Fe chains.

The skyrmion lattice represents a new class of magnetic structure in ultrathin films and it is – up to my knowledge – the first skyrmion lattice as the magnetic *ground state* of a system. In the process of the data evaluation it was fascinating to see, how it is possible to construct the complete magnetization density of the sample by superposition of SP-STM measurements with different tip magnetizations. Simultaneous measurements of the atomic lattice and the contrast due to the spin-orbit interaction, TAMR, identified the incommensurability of the magnetic and atomic structure.

Even though the square skyrmion lattice as the ground state of the Fe ML is fascinating enough and its beauty alone justifies all the measurements, this discovery gives rise to further interesting questions. Since skyrmions are topologically protected it is interesting to study the robustness of the skyrmion lattice. Could lateral confinement or a large external magnetic field distort or even destroy the lattice? What is the minimal island size needed to observe the lattice or a single skyrmion? Is it possible to excite the skyrmion lattice and how would the excitations look like? Furthermore, the Fe ML does not solely grow in the fcc but also in the hcp stacking, see Fig. 6.3, whose magnetic ground state has not been investigated so far. Some of those questions could be answered with the help of SP-STM measurements at lower temperatures and larger

magnetic fields.

SP-STM measurements at lower temperatures could also lead to further understanding of the spin spiral state in the Fe chains and could verify some of the theoretical predictions. At temperatures below the calculated blocking temperature, it might be possible to observe the spin spiral without an applied magnetic field. In addition, the OOMMF simulations predict a very slow, linear decay of the magnetization in the chain when one of the ends is fixed, which makes the chains ideal for the transport of spin information. By fixing the magnetic moment of one end of the chain (input), the magnetization at the other end (output), only depends on the length of the chain. For some chain length a change in the spin spiral angle with an applied magnetic field is predicted, meaning that the angle between the first and the last magnetic moment in the chain could be tuned by an external magnetic field.

Besides the inner hollow site chains presented in Ch. 5, chains can also be grown in the outer hollow sites or zigzag configuration, see Figs. 4.5 and 5.3. DFT calculations for the outer hollow site chains predict a similarly small Heisenberg exchange as for the inner hollow site chains [77]. Furthermore, the unreconstructed Ir(001) substrate allows to grow Fe-Ir-Fe sandwich chains [147] and also a ML film. While the sandwich chains are predicted to show a transition from AFM to FM order with increasing hydrogen coverage [85] the Fe ML might be a candidate for another non-collinear magnetic ground state [148].

In summary, due to their exotic magnetic properties the Fe nanostructures on Ir surfaces I presented in this thesis are model systems to study and understand the interplay of competing magnetic interactions on the atomic scale. They might stimulate research for novel magnetic materials and might also trigger theoretical investigations of barely understood magnetization dynamics in non-collinear spin systems.

Bibliography

[1] S. Stringari and R. Wilson. *Romagnosi and the discovery of electromagnetism*. Rendiconti Lincei **11**, 115 (2000). 1

[2] S. C. Abrahams, L. Guttman, and J. S. Kasper. *Neutron Diffraction Determination of Antiferromagnetism in Face-Centered Cubic (γ) Iron*. Physical Review **127**, 2052 (1962). 2

[3] Y. Endoh and Y. Ishikawa. *Antiferromagnetism of γ Iron Manganes Alloys*. Journal of the Physical Society of Japan **30**, 1614 (1971). 2

[4] R. Wiesendanger. *Scanning Probe Microscopy and Spectroscopy*. Cambridge University Press (1994). 2

[5] S. Meckler, N. Mikuszeit, A. Pressler, E. Y. Vedmedenko, O. Pietzsch, and R. Wiesendanger. *Real-Space Observation of a Right-Rotating Inhomogeneous Cycloidal Spin Spiral by Spin-Polarized Scanning Tunneling Microscopy in a Triple Axes Vector Magnet*. Physical Review Letters **103**, 157201 (2009). 2, 29

[6] A. Kubetzka, P. Ferriani, M. Bode, S. Heinze, G. Bihlmayer, K. von Bergmann, O. Pietzsch, S. Blügel, and R. Wiesendanger. *Revealing Antiferromagnetic Order of the Fe Monolayer on W(001): Spin-Polarized Scanning Tunneling Microscopy and First-Principles Calculations*. Physical Review Letters **94**, 087204 (2005). 2, 29, 43

[7] J. Chen and J. L. Erskine. *Surface-step-induced magnetic anisotropy in thin epitaxial Fe films on W(001)*. Physical Review Letters **68**, 1212 (1992). 2

[8] K. von Bergmann, S. Heinze, M. Bode, E. Y. Vedmedenko, G. Bihlmayer, S. Blügel, and R. Wiesendanger. *Observation of a Complex Nanoscale Magnetic Structure in a Hexagonal Fe Monolayer*. Physical Review Letters **96**, 167203 (2006). 2, 72, 73, 74, 75, 82, 83

[9] K. von Bergmann, S. Heinze, M. Bode, G. Bihlmayer, S. Blügel, and R. Wiesendanger. *Complex magnetism of the Fe monolayer on Ir(111)*. New Journal of Physics **9**, 396 (2007). 2, 72, 73, 74, 75, 82

[10] W. Heisenberg. *Mehrkörperproblem und Resonanz in der Quantenmechanik*. Zeitschrift für Physik A Hadrons and Nuclei **38**, 411 (1926). 3

[11] P. A. M. Dirac. *On the Theory of Quantum Mechanics*. Proceedings of the Royal Society of London. Series A, Containing Papers of a Mathematical and Physical Character **112**, 661 (1926). 3

[12] S. Blundell. *Magnetism in Condensed Matter*. Oxford University Press (2001). 3

[13] C. Davisson and L. H. Germer. *Diffraction of Electrons by a Crystal of Nickel*. Physical Review **30**, 705 (1927). 3, 26

[14] W. Pauli. *Zur Quantenmechanik des magnetischen Elektrons*. Zeitschrift für Physik A Hadrons and Nuclei **43**, 601 (1927). 4

[15] M. Bode, M. Heide, K. von Bergmann, P. Ferriani, S. Heinze, A. Bihlmayer, G.and Kubetzka, O. Pietzsch, S. Blügel, and R. Wiesendanger. *Chiral magnetic order at surfaces driven by inversion asymmetry*. Nature **447**, 190 (2007). 8, 9, 20, 29, 39, 45, 58, 75

[16] S. Mühlbauer, B. Binz, F. Jonietz, C. Pfleiderer, A. Rosch, A. Neubauer, R. Georgii, and P. Boni. *Skyrmion Lattice in a Chiral Magnet*. Science **323**, 915 (2009). 8, 72

[17] I. Dzyaloshinskii. *A thermodynamic theory of "weak" ferromagnetism of antiferromagnetics*. Journal of Physics and Chemistry of Solids **4**, 241 (1958). 8, 52, 88

[18] T. Moriya. *Anisotropic Superexchange Interaction and Weak Ferromagnetism*. Physical Review **120**, 91 (1960). 8, 52

[19] P. Ferriani, K. von Bergmann, E. Y. Vedmedenko, S. Heinze, M. Bode, M. Heide, G. Bihlmayer, S. Blügel, and R. Wiesendanger. *Atomic-Scale Spin Spiral with a Unique Rotational Sense: Mn Monolayer on W(001)*. Physical Review Letters **101**, 027201 (2008). 9, 20

[20] E. Y. Vedmedenko, L. Udvardi, P. Weinberger, and R. Wiesendanger. *Chiral magnetic ordering in two-dimensional ferromagnets with competing Dzyaloshinsky-Moriya interactions*. Physical Review B **75**, 104431 (2007). 9

[21] A. Fert and P. M. Levy. *Role of Anisotropic Exchange Interactions in Determining the Properties of Spin-Glasses*. Physical Review Letters **44**, 1538 (1980). 9, 90

[22] M. Heide, G. Bihlmayer, P. Mavropoulos, A. Bringer, and S. Blügel. *Spin Orbit Driven Physics at Surfaces*. Psi-k Newsletter **78**, 1 (2006). 9, 52, 75, 88

[23] A. H. MacDonald, S. M. Girvin, and D. Yoshioka. *t/U expansion for the Hubbard model*. Physical Review B **37**, 9753 (1988). 9

[24] R. Wieser, E. Y. Vedmedenko, and R. Wiesendanger. *Entropy driven phase transition in itinerant antiferromagnetic monolayers*. Physical Review B **77**, 064410 (2008). 9, 10, 53

[25] G. Binnig and H. Rohrer. *Scanning Tunneling Microscopy*. Helvetica Physica Acta **55**, 726 (1982). 13

[26] G. Binnig, H. Rohrer, C. Gerber, and E. Weibel. *7×7 Reconstruction on Si(111) Resolved in Real Space*. Physical Review Letters **50**, 120 (1983). 13

[27] J. Bardeen. *Tunnelling from a Many-Particle Point of View*. Physical Review Letters **6**, 57 (1961). 15

[28] J. Tersoff and D. R. Hamann. *Theory and Application for the Scanning Tunneling Microscope*. Physical Review Letters **50**, 1998 (1983). 16

[29] J. Tersoff and D. R. Hamann. *Theory of the scanning tunneling microscope*. Physical Review B **31**, 805 (1985). 16

[30] C. J. Chen. *Theory of scanning tunneling microscopy*. Journal of Vacuum Science and Technology A **6**, 319 (1988). 18

[31] C. J. Chen. *Tunneling matrix elements in three-dimensional space: The derivative rule and the sum rule*. Physical Review B **42**, 8841 (1990). 18

[32] C. J. Chen. *Origin of atomic resolution on metal surfaces in scanning tunneling microscopy*. Physical Review Letters **65**, 448 (1990). 18

[33] C. J. Chen. *Introduction to Scanning Tunneling Microscopy*. Oxford University Press (1993). 18

[34] L. Vitali, S. D. Borisova, G. G. Rusina, E. V. Chulkov, and K. Kern. *Inelastic electron tunneling spectroscopy: A route to the identification of the tip-apex structure*. Physical Review B **81**, 153409 (2010). 18

[35] L. Bartels, G. Meyer, and K.-H. Rieder. *Controlled vertical manipulation of single CO molecules with the scanning tunneling microscope: A route to chemical contrast*. Applied Physics Letters **71**, 213 (1997). 20

[36] K. von Bergmann, M. Bode, A. Kubetzka, M. Heide, S. Blügel, and R. Wiesendanger. *Spin-Polarized Electron Scattering at Single Oxygen Adsorbates on a Magnetic Surface*. Physical Review Letters **92**, 046801 (2004). 20

[37] N. D. Lang. *Theory of Single-Atom Imaging in the Scanning Tunneling Microscope*. Physical Review Letters **56**, 1164 (1986). 20

[38] M. Bode, S. Heinze, A. Kubetzka, O. Pietzsch, X. Nie, G. Bihlmayer, S. Blügel, and R. Wiesendanger. *Magnetization-Direction-Dependent Local Electronic Structure Probed by Scanning Tunneling Spectroscopy*. Physical Review Letters **89**, 237205 (2002). 20

[39] M. Julliere. *Tunneling between ferromagnetic films*. Physics Letters A **54**, 225 (1975). 22

[40] J. C. Slonczewski. *Conductance and exchange coupling of two ferromagnets separated by a tunneling barrier*. Physical Review B **39**, 6995 (1989). 22

[41] T. Miyazaki and N. Tezuka. *Giant magnetic tunneling effect in $Fe/Al_2O_3/Fe$ junction*. Journal of Magnetism and Magnetic Materials **139**, L231 (1995). 23

[42] R. Wiesendanger, H.-J. Güntherodt, G. Güntherodt, R. J. Gambino, and R. Ruf. *Observation of vacuum tunneling of spin-polarized electrons with the scanning tunneling microscope*. Physical Review Letters **65**, 247 (1990). 23

[43] M. Bode. *Spin-polarized scanning tunneling microscopy*. Reports on Progress in Physics **66**, 523 (2003). 23, 28

[44] R. Wiesendanger. *Spin mapping at the nanoscale and atomic scale*. Review of Modern Physics **81**, 1495 (2009). 23

[45] S. Loth, K. von Bergmann, M. Ternes, A. F. Otte, C. P. Lutz, and A. J. Heinrich. *Controlling the state of quantum spins with electric currents*. Nature Physics **6**, 340 (2010). 23, 29, 67

[46] A. A. Khajetoorians, S. Lounis, B. Chilian, A. T. Costa, L. Zhou, D. L. Mills, J. Wiebe, and R. Wiesendanger. *Itinerant Nature of Atom-Magnetization Excitation by Tunneling Electrons*. Physical Review Letters **106**, 037205 (2011). 23

[47] T. Balashov, A. F. Takács, W. Wulfhekel, and J. Kirschner. *Magnon Excitation with Spin-Polarized Scanning Tunneling Microscopy*. Physical Review Letters **97**, 187201 (2006). 23

[48] C. L. Gao, A. Ernst, G. Fischer, W. Hergert, P. Bruno, W. Wulfhekel, and J. Kirschner. *Spin Wave Dispersion on the Nanometer Scale*. Physical Review Letters **101**, 167201 (2008). 23

[49] D. Serrate, P. Ferriani, Y. Yoshida, S.-W. Hla, M. Menzel, K. von Bergmann, S. Heinze, A. Kubetzka, and R. Wiesendanger. *Imaging and manipulating the spin direction of individual atoms*. Nature Nanotechnology **5**, 350 (2010). 23

[50] A. A. Khajetoorians, J. Wiebe, B. Chilian, and R. Wiesendanger. *Realizing All-Spin-Based Logic Operations Atom by Atom*. Science **332**, 1062 (2011). 23, 66, 67

[51] S. Loth, M. Etzkorn, C. P. Lutz, D. M. Eigler, and A. J. Heinrich. *Measurement of Fast Electron Spin Relaxation Times with Atomic Resolution*. Science **329**, 1628 (2010). 23

[52] J. A. Venables. *Introduction to Surface and Thin Film Processes*. Cambridge University Press (2000). 25

[53] `www.omicron.de`. 25, 26

[54] K. Heinz. *LEED and DLEED as modern tools for quantitative surface structure determination*. Reports on Progress in Physics **58**, 637 (1995). 26

[55] L. Meitner. *Über die β-Strahl-Spektra und ihren Zusammenhang mit der γ-Strahlung*. Zeitschrift für Physik A Hadrons and Nuclei **11**, 35 (1922). 26

[56] P. Weightman. *X-ray-excited Auger and photoelectron spectroscopy*. Reports on Progress in Physics **45**, 753 (1982). 26

[57] C. Witt, U. Mick, M. Bode, and R. Wiesendanger. *An ultrahigh vacuum scanning tunneling microscope for in situ studies of thin-film growth*. Review of Scientific Instruments **68**, 1455 (1997). 26

[58] D. Haude. *Ultrahochvakuum-Rastertunnelmikroskopie: Instrumentierung und Anwendung*. Master's thesis, University of Hamburg (1997). 27

[59] O. Pietzsch, A. Kubetzka, D. Haude, M. Bode, and R. Wiesendanger. *A low-temperature ultrahigh vacuum scanning tunneling microscope with a split-coil magnet and a rotary motion stepper motor for high spatial resolution studies of surface magnetism*. Review of Scientific Instruments **71**, 424 (2000). 27

[60] O. Pietzsch. *Aufbau eines Rastertunnelmikroskops für den Einsatz im Ultrahochvakuum, bei tiefen Temperaturen und in hohen Magnetfeldern*. Master's thesis, Uinversity of Hamburg (1997). 27

[61] A. Kubetzka. *Optimierung eines Rastertunnelmikroskops für die Durchführung spinpolarisierter Rastertunnelmikroskopie*. Master's thesis, University of Hamburg (1999). 27

[62] O. Pietzsch, A. Kubetzka, M. Bode, and R. Wiesendanger. *Spin-Polarized Scanning Tunneling Spectroscopy of Nanoscale Cobalt Islands on Cu(111)*. Physical Review Letters **92**, 057202 (2004). 29

[63] F. Meier, L. Zhou, J. Wiebe, and R. Wiesendanger. *Revealing Magnetic Interactions from Single-Atom Magnetization Curves*. Science **320**, 82 (2008). 29

[64] L. Zhou, J. Wiebe, S. Lounis, E. Vedmedenko, F. Meier, S. Blügel, P. H. Dederichs, and R. Wiesendanger. *Strength and directionality of surface Ruderman-Kittel-Kasuya-Yosida interaction mapped on the atomic scale*. Nature Physics **6**, 187 (2010). 29

[65] L. Berbil-Bautista, S. Krause, M. Bode, and R. Wiesendanger. *Spin-polarized scanning tunneling microscopy and spectroscopy of ferromagnetic Dy(0001)/W(110) films*. Physical Review B **76**, 064411 (2007). 29

[66] A. Li Bassi, C. S. Casari, D. Cattaneo, F. Donati, S. Foglio, S. Passoni, C. E. Bottani, P. Biagioni, A. Brambilla, M. Finazzi, F. Ciccacci, and L. Duo. *Bulk Cr tips for scanning tunneling microscopy and spin-polarized scanning tunneling microscopy*. Applied Physics Letters **91**, 173120 (2007). 29

[67] A. Schlenhoff, S. Krause, G. Herzog, and R. Wiesendanger. *Bulk Cr tips with full spatial magnetic sensitivity for spin-polarized scanning tunneling microscopy*. Applied Physics Letters **97**, 083104 (2010). 29

[68] C. Hanneken. *Development and Characterization of Cr Bulk Tips for SP-STM*. Master's thesis, University of Hamburg (2011). 29

[69] A. Schmidt, W. Meier, L. Hammer, and K. Heinz. *Deep-going reconstruction of Ir(100)-5 × 1*. Journal of Physics: Condensed Matter **14**, 12353 (2002). 31, 32

[70] `www.omicron.de/en/products/efm-3-/instrument-concept`. 31

[71] A. Ignatiev, A. Jones, and T. Rhodin. *Leed investigations of xenon single crystal films and their use in studying the Ir(100) surface*. Surface Science **30**, 573 (1972). 31

[72] E. Lang, K. Müller, K. Heinz, M. V. Hove, R. Koestner, and G. Somorjai. *LEED intensity analysis of the (1×5) reconstruction of Ir(100)*. Surface Science **127**, 347 (1983). 31

[73] Q. Ge, D. A. King, N. Marzari, and M. C. Payne. *First principles calculation of the energy and structure of two solid surface phases on Ir100*. Surface Science **418**, 529 (1998). 31

[74] G. Gilarowski, J. Mendez, and H. Niehus. *Initial growth of Cu on Ir(100)-(5×1)*. Surface Science **448**, 290 (2000). 32

[75] L. Hammer, W. Meier, A. Schmidt, and K. Heinz. *Submonolayer iron film growth on reconstructed Ir(100)-(5×1)*. Physical Review B **67**, 125422 (2003). 32, 33, 34

[76] D. Spišák and J. Hafner. *Reconstruction and de-reconstruction of the Ir(1 0 0) surface and ultrathin Fe/Ir(1 0 0) films*. Surface Science **546**, 27 (2003). 32, 33, 35

[77] Y. Mokrousov, A. Thiess, and S. Heinze. *Structurally driven magnetic state transition of biatomic Fe chains on Ir(001)*. Physical Review B **80**, 195420 (2009). 32, 33, 34, 35, 51, 96

[78] M. Menzel. *Wachstum und elektronische Eigenschaften von atomaren Eisen-Ketten auf Iridium(001)*. Master's thesis, University of Hamburg (2006). 33, 35

[79] K. Heinz and L. Hammer. *Nanostructure formation on Ir(100)*. Progress in Surface Science **84**, 2 (2009). 33

[80] A. Klein. *Nickel-Nanostrukturen auf Iridium(100)*. Ph.D. thesis, University of Erlangen-Nürnberg (2007). 33

[81] R. Mazzarello and E. Tosatti. *Connection between magnetism and structure in Fe double chains on the Ir(100) surface*. Physical Review B **79**, 134402 (2009). 33, 34, 35, 52

[82] J. N. Crain and D. T. Pierce. *End States in One-Dimensional Atom Chaims*. Science **307**, 703 (2005). 36, 44

[83] S. Fölsch, P. Hyldgaard, R. Koch, and K. H. Ploog. *Quantum Confinement in Monatomic Cu Chains on Cu(111)*. Physical Review Letters **92**, 056803 (2004). 39, 45

[84] K. Sagisaka and D. Fujita. *Quasi-one-dimensional quantum well on Si(100) surface crafted by using scanning tunneling microscopy tip*. Applied Physics Letters **88**, 203118 (2006). 39

[85] F. R. Vukajlović, Z. S. Popović, A. Baldereschi, and i. c. v. Šljivančanin. *Effect of adsorbed H atoms on magnetism in monoatomic Fe wires at Ir(100)*. Physical Review B **81**, 085425 (2010). 42, 96

[86] N. D. Mermin and H. Wagner. *Absence of Ferromagnetism or Antiferromagnetism in One- or Two-Dimensional Isotropic Heisenberg Models*. Physical Review Letters **17**, 1133 (1966). 43

[87] O. Pietzsch, A. Kubetzka, M. Bode, and R. Wiesendanger. *Observation of Magnetic Hysteresis at the Nanometer Scale by Spin-Polarized Scanning Tunneling Spectroscopy*. Science **292**, 2053 (2001). 43

[88] J. des Cloizeaux and J. J. Pearson. *Spin-Wave Spectrum of the Antiferromagnetic Linear Chain*. Physical Review **128**, 2131 (1962). 44

[89] D. A. Tennant, T. G. Perring, R. A. Cowley, and S. E. Nagler. *Unbound spinons in the S=1/2 antiferromagnetic chain KCuF3*. Physical Review Letters **70**, 4003 (1993). 44

[90] J. W. Bray, H. R. Hart, L. V. Interrante, I. S. Jacobs, J. S. Kasper, G. D. Watkins, S. H. Wee, and J. C. Bonner. *Observation of a Spin-Peierls Transition in a Heisenberg Antiferromagnetic Linear-Chain System*. Physical Review Letters **35**, 744 (1975). 44

[91] K. Uchinokura. *Spin-Peierls transition in $CuGeO_3$ and impurity-induced ordered phases in low-dimensional spin-gap systems*. Journal of Physics: Condensed Matter **14**, R195 (2002). 44

[92] P. Anderson, P. Lee, and M. Saitoh. *Remarks on giant conductivity in TTF-TCNQ*. Solid State Communications **13**, 595 (1973). 44

[93] `http://galileo.phys.virginia.edu/classes/752.mf1i.spring03/PeierlsTrans.htm`. 44

[94] F. D. M. Haldane. *Nonlinear Field Theory of Large-Spin Heisenberg Antiferromagnets: Semiclassically Quantized Solitons of the One-Dimensional Easy-Axis Néel State*. Physical Review Letters **50**, 1153 (1983). 44

[95] M. P. Nightingale and H. W. J. Blöte. *Gap of the linear spin-1 Heisenberg antiferromagnet: A Monte Carlo calculation*. Physical Review B **33**, 659 (1986). 44

[96] S. R. White and D. A. Huse. *Numerical renormalization-group study of low-lying eigenstates of the antiferromagnetic S=1 Heisenberg chain*. Physical Review B **48**, 3844 (1993). 44

[97] H.-J. Mikeska and A. K. Kolezhuk. *One-Dimensional Magnetism*. In *Quantum Magnetism*, vol. 645 of *Lecture Notes in Physics*, pp. 1–83. Springer Berlin / Heidelberg (2004). 44

[98] W. J. L. Buyers, R. M. Morra, R. L. Armstrong, M. J. Hogan, P. Gerlach, and K. Hirakawa. *Experimental evidence for the Haldane gap in a spin-1 nearly isotropic, antiferromagnetic chain*. Physical Review Letters **56**, 371 (1986). 44

[99] Y. Yoshida, N. Tateiwa, M. Mito, T. Kawae, K. Takeda, Y. Hosokoshi, and K. Inoue. *Specific Heat Study of an $S = 1/2$ Alternating Heisenberg Chain System: F_5PNN in a Magnetic Field*. Physical Review Letters **94**, 037203 (2005). 44

[100] T. Matsui, C. Meyer, L. Sacharow, J. Wiebe, and R. Wiesendanger. *Electronic states of Fe atoms and chains on InAs(110) from scanning tunneling spectroscopy*. Physical Review B **75**, 165405 (2007). 44

[101] J. Schäfer, C. Blumenstein, S. Meyer, M. Wisniewski, and R. Claessen. *New Model System for a One-Dimensional Electron Liquid: Self-Organized Atomic Gold Chains on Ge(001)*. Physical Review Letters **101**, 236802 (2008). 44

[102] H. Röder, E. Hahn, H. Brune, J.-P. Bucher, and K. Kern. *Building one- and two-dimensional nanostructures by diffusion-controlled aggregation at surfaces*. Nature **366**, 141 (1993). 44

[103] P. Gambardella, M. Blanc, K. Kuhnke, K. Kern, F. Picaud, C. Ramseyer, C. Girardet, C. Barreteau, D. Spanjaard, and M. C. Desjonquères. *Growth of composition-modulated Ag/Co wires on Pt(997)*. Physical Review B **64**, 045404 (2001). 44

[104] N. Nilius, T. M. Wallis, and W. Ho. *Development of One-Dimensional Band Structure in Artificial Gold Chains*. Science **297**, 1853 (2002). 45

[105] C. F. Hirjibehedin, C. P. Lutz, and A. J. Heinrich. *Spin Coupling in Engineered Atomic Structures*. Science **312**, 1021 (2006). 45

[106] P. Gambardella, A. Dallmeyer, K. Maiti, M. C. Malagoli, W. Eberhardt, K. Kern, and C. Carbone. *Ferromagnetism in one-dimensional monatomic metal chains*. Nature **416**, 301 (2002). 45

[107] D. Wortmann, S. Heinze, P. Kurz, G. Bihlmayer, and S. Blügel. *Resolving Complex Atomic-Scale Spin Structures by Spin-Polarized Scanning Tunneling Microscopy*. Physical Review Letters **86**, 4132 (2001). 47

[108] www.flapw.de. 51, 90

[109] F. Cinti, A. Rettori, M. G. Pini, M. Mariani, E. Micotti, A. Lascialfari, N. Papinutto, A. Amato, A. Caneschi, D. Gatteschi, and M. Affronte. *Two-Step Magnetic Ordering in Quasi-One-Dimensional Helimagnets: Possible Experimental Validation of Villain's Conjecture about a Chiral Spin Liquid Phase*. Physical Review Letters **100**, 057203 (2008). 55, 56

[110] http://math.nist.gov/oommf/. 57

[111] L. D. Landau and E. M. Lifshitz. *On the Theory of the Dispersion of magnetic Permeability in ferromagnetic bodies*. Physikalische Zeitschrift der Sowjetunion **8**, 153 (1935). 57

[112] O. Lemcke. *Simulation von Temperatureffekten in magnetischen Nanostrukturen*. Master's thesis, University of Hamburg (2004). 58

[113] www.nanoscience.de/group_r/stm-spstm/projects/temperature/theory.shtml. 58

[114] S. Krause, L. Berbil-Bautista, G. Herzog, M. Bode, and R. Wiesendanger. *Current-Induced Magnetization Switching with a Spin-Polarized Scanning Tunneling Microscope*. Science **317**, 1537 (2007). 61, 67

[115] S. Krause, G. Herzog, T. Stapelfeldt, L. Berbil-Bautista, M. Bode, E. Y. Vedmedenko, and R. Wiesendanger. *Magnetization Reversal of Nanoscale Islands: How Size and Shape Affect the Arrhenius Prefactor*. Physical Review Letters **103**, 127202 (2009). 61, 62

[116] W. F. Brown. *Thermal Fluctuations of a Single-Domain Particle*. Physical Review **130**, 1677 (1963). 62

[117] P. Gambardella, S. Rusponi, M. Veronese, S. S. Dhesi, C. Grazioli, A. Dallmeyer, I. Cabria, R. Zeller, P. H. Dederichs, K. Kern, C. Carbone, and H. Brune. *Giant Magnetic Anisotropy of Single Cobalt Atoms and Nanoparticles*. Science **300**, 1130 (2003). 62

[118] S. Rusponi, T. Cren, N. Weiss, M. Epple, P. Buluschek, L. Claude, and H. Brune. *The remarkable difference between surface and step atoms in the magnetic anisotropy of two-dimensional nanostructures*. Nature Materials **2**, 546 (2003). 62

[119] http://www.ma.hw.ac.uk/~chris/scott_russell.html. 69

[120] http://en.wikipedia.org/wiki/Soliton. 69

[121] L. F. Mollenauer and K. Smith. *Demonstration of soliton transmission over more than 4000 kmin fiber with loss periodically compensated by Raman gain*. Optics Letters **13**, 675 (1988). 69

[122] T. H. R. Skyrme. *A Non-Linear Theory of Strong Interactions*. Proceedings of the Royal Society of London. Series A. Mathematical and Physical Sciences **247**, 260 (1958). 69

[123] T. H. R. Skyrme. *A unified field theory of mesons and baryons*. Nuclear Physics **31**, 556 (1962). 69, 70

[124] S. M. H. Wong. *What exactly is a Skyrmion?* ArXiv High Energy Physics - Phenomenology e-prints (2002). 70

[125] U. Al Khawaja and H. Stoof. *Skyrmions in a ferromagnetic Bose-Einstein condensate*. Nature **411**, 918 (2001). 70

[126] D. C. Wright and N. D. Mermin. *Crystalline liquids: the blue phases*. Review of Modern Physics **61**, 385 (1989). 70

[127] R. Durrer, M. Kunz, and A. Melchiorri. *Cosmic structure formation with topological defects*. Physics Reports **364**, 1 (2002). 70

[128] S. L. Sondhi, A. Karlhede, S. A. Kivelson, and E. H. Rezayi. *Skyrmions and the crossover from the integer to fractional quantum Hall effect at small Zeeman energies*. Physical Review B **47**, 16419 (1993). 70

[129] L. Brey, H. A. Fertig, R. Côté, and A. H. MacDonald. *Skyrme Crystal in a Two-Dimensional Electron Gas*. Physical Review Letters **75**, 2562 (1995). 70

[130] A. A. Abrikosov. *Nobel Lecture: Type-II superconductors and the vortex lattice*. Review of Modern Physics **76**, 975 (2004). 70

[131] A. N. Bogdanov and D. A. Yablonskii. *Thermodynamically stable "vortices" in magnetically ordered crystals. The mixed state of magnets*. Soviet Physics Journal of Experimental and Theoretical Physics **95**, 178 (1989). 70, 72

[132] X. Z. Yu, Y. Onose, N. Kanazawa, J. H. Park, J. H. Han, Y. Matsui, N. Nagaosa, and Y. Tokura. *Real-space observation of a two-dimensional skyrmion crystal*. Nature **465**, 901 (2010). 72

[133] X. Z. Yu, N. Kanazawa, Y. Onose, K. Kimoto, W. Z. Zhang, S. Ishiwata, Y. Matsui, and Y. Tokura. *Near room-temperature formation of a skyrmion crystal in thin-films of the helimagnet FeGe*. Nature Materials **10**, 106 (2011). 72

[134] C. Pappas, E. Lelièvre-Berna, P. Falus, P. M. Bentley, E. Moskvin, S. Grigoriev, P. Fouquet, and B. Farago. *Chiral Paramagnetic Skyrmion-like Phase in MnSi*. Physical Review Letters **102**, 197202 (2009). 72

[135] U. K. Rössler, A. N. Bogdanov, and C. Pfleiderer. *Spontaneous skyrmion ground states in magnetic metals*. Nature **442**, 797 (2006). 72

[136] S. Andrieu, M. Piecuch, and J. F. Bobo. *Fe growth on (0001) hcp Ru and (111) fcc Ir: Consequences for structural and magnetic properties*. Physical Review B **46**, 4909 (1992). 72

[137] W. L. O'Brien and B. P. Tonner. *Magnetic and structural properties of ultrathin Mn and Fe films on Ir(111)*. Journal of Vacuum Science & Technology A: Vacuum, Surfaces, and Films **13**, 1544 (1995). 72, 74

[138] G. Schütz, W. Wagner, W. Wilhelm, P. Kienle, R. Zeller, R. Frahm, and G. Materlik. *Absorption of circularly polarized x rays in iron*. Physical Review Letters **58**, 737 (1987). 72

[139] C. Pfleiderer and U. K. Rössler. *Condensed-matter physics: Let's twist again*. Nature **447**, 157 (2007). 75

[140] C. L. Gao, U. Schlickum, W. Wulfhekel, and J. Kirschner. *Mapping the Surface Spin Structure of Large Unit Cells: Reconstructed Mn Films on Fe(001)*. Physical Review Letters **98**, 107203 (2007). 77

[141] C. L. Gao, A. Ernst, A. Winkelmann, J. Henk, W. Wulfhekel, P. Bruno, and J. Kirschner. *Noncollinear Surface Spin Density by Surface*

Reconstruction in the Alloy NiMn. Physical Review Letters **100**, 237203 (2008). 77

[142] C. Wittneven, R. Dombrowski, S. H. Pan, and R. Wiesendanger. *A low-temperature ultrahigh-vacuum scanning tunneling microscope with rotatable magnetic field*. Review of Scientific Instruments **68**, 3806 (1997). 80

[143] S. Heinze. *Simulation of spin-polarized scanning tunneling microscopy images of nanoscale non-collinear magnetic structures*. Applied Physics A: Materials Science & Processing **85**, 407 (2006). 80

[144] K. von Bergmann. *private communication*. 83

[145] J. P. Perdew, K. Burke, and M. Ernzerhof. *Generalized Gradient Approximation Made Simple*. Physical Review Letters **77**, 3865 (1996). 90

[146] J. P. Perdew and A. Zunger. *Self-interaction correction to density-functional approximations for many-electron systems*. Physical Review B **23**, 5048 (1981). 90

[147] L. Hammer, W. Meier, A. Klein, P. Landfried, A. Schmidt, and K. Heinz. *Hydrogen-Induced Self-Organized Nanostructuring of the Ir(100) Surface*. Physical Review Letters **91**, 156101 (2003). 96

[148] J. Kudrnovský, F. c. v. Máca, I. Turek, and J. Redinger. *Substrate-induced antiferromagnetism of a Fe monolayer on the Ir(001) surface*. Physical Review B **80**, 064405 (2009). 96

Publications

Research articles

- D. Serrate, P. Ferriani, Y. Yoshida, S.-W. Hla, M. Menzel, K. von Bergmann, S. Heinze, A. Kubetzka, and R. Wiesendanger, *Imaging and manipulating the spin direction of individual atoms*, Nature Nanotechnology **5**, 350 (2010)

- S. Heinze, K. von Bergmann, M. Menzel, J. Brede, A. Kubetzka, R. Wiesendanger, G. Bihlmayer, and S. Blügel, *Spontaneous atomic-scale magnetic skyrmion lattice in two dimensions*, Nature Physics **7**, 713 (2011)

- M. Menzel, Y. Mokrousov, R. Wieser, J. E. Bickel, K. von Bergmann, E. Y. Vedmedenko, S. Blügel, S. Heinze, A. Kubetzka, and R. Wiesendanger, *Information transfer by vector spin chirality in finite magnetic chains*, submitted

Awards

- 01.09.2011:
  ECOSS Prize 2011, European Conference on Surface Science 28, Wrocław (Poland)

Invited talks

- 14.07.2010:
  M. Menzel, *Complex magnetism in bi-atomic Fe chains on* (5×1)*-reconstructed Ir(001)*, Theorie I Seminar, Institut für Festkörperforschung, Forschungszentrum Jülich, Jülich (Germany)

Contributed talks

- 26.03.2007:
  M. Menzel, A. Kubetzka, K. von Bergmann, M. Bode, and R. Wiesendanger, *Electronic properties of self-organized bi-atomic Fe chains on Ir(001)*, 71st Spring Conference, Deutsche Physikalische Gesellschaft, Regensburg (Germany)

- 04.07.2007:
  M. Menzel, A. Kubetzka, K. von Bergmann, M. Bode, and R. Wiesendanger, *Growth and electronic properties of atomic Fe chains on Ir(001)*, International Conference on Nanoscience and Technology, Stockholm (Sweden)

- 23.03.2009:
  M. Menzel, K. von Bergmann, A. Kubetzka, and R. Wiesendanger, *Periodic LDOS modulations in self-organized bi-atomic chains*, 73rd Spring Conference, Deutsche Physikalische Gesellschaft, Dresden (Germany)

- 25.03.2010:
  M. Menzel, S. Heinze, K. von Bergmann, G. Bihlmayer, A. Kubetzka, S. Blügel, and R. Wiesendanger, *Two-dimensional non-collinear magnetic ground state in the Fe monolayer on Ir(111)*, 74rd Spring Conference, Deutsche Physikalische Gesellschaft, Regensburg (Germany)

- 19.08.2010:
  M. Menzel, S. Heinze, K. von Bergmann, G. Bihlmayer, A. Kubetzka, S. Blügel, and R. Wiesendanger, *Atomic-scale magnetic skyrmion lattice observed in real space*, International Conference on Spin-Polarized Scanning Tunneling Microscopy 3, Seoul (Korea)

- 26.08.2010:
  M. Menzel, S. Heinze, K. von Bergmann, G. Bihlmayer, A. Kubetzka, S. Blügel, and R. Wiesendanger, *Atomic-scale magnetic skyrmion lattice observed in real space*, International Conference on Nanoscience and Technology, Beijing (China)

- 31.08.2011:
  M. Menzel, Y. Mokrousov, R. Wieser, K. von Bergmann, E. Vedmedenko, S. Blügel, S. Heinze, A. Kubetzka, and R. Wiesendanger, *Atomic-scale spin spiral observed in individual metallic chains*, European Conference on Surface Science 28, Wrocław (Poland)

Posters

- 26.02.2008:
  M. Menzel, D. Haude, K. von Bergmann, M. Bode, and R. Wiesendanger, *Design of a UHV-STM for applications at low temperatures and high magnetic fields*, 72nd Spring Conference, Deutsche Physikalische Gesellschaft, Berlin (Germany)

- 11.09.2008:
  M. Menzel, K. von Bergmann, A. Kubetzka, M. Bode, and R. Wiesendanger, *Scanning tunneling microscopy and spectroscopy of self-organized bi-atomic Fe chains on Ir(001)*, Summer School "Nanomagnetism and Spintronics", Prague (Czech Republic)

- 23.07.2009:
  M. Menzel, K. von Bergmann, A. Kubetzka, and R. Wiesendanger, *Periodic LDOS modulations in bi-atomic Fe chains*, 20th International Colloquium on Magnetic Films and Surfaces (ICMFS), Berlin (Germany)

A. Source code for interactions in OOMMF

```
1  /* FILE: my_1dexchange.h                -*-Mode: c++-*-*/
2
3  #ifndef _MM_1DEXCHANGE
4  #define _MM_1DEXCHANGE
5
6  #include "oc.h"
7  #include "director.h"
8  #include "energy.h"
9  #include "meshvalue.h"
10 #include "simstate.h"
11 #include "threevector.h"
12
13 /* End includes */
14
15 class MM_1DExchange:public Oxs_Energy{
16 private:
17   REAL8m A1;
18   REAL8m A2;
19   REAL8m A3;
20   REAL8m A4;
21   REAL8m A5;
22   REAL8m A6;
23   REAL8m A7;
24   REAL8m A8;
25   REAL8m A9;
26   REAL8m A10;
27
28   enum ExchangeKernel { UNKNOWN, NGBR_6} kernel;
29   /// Exchange formulation to use.  "unknown" is invalid; it
30   /// is defined for error detection.
31
32   // Calculation routines for each of the
33   // aforementioned energy formulations.
34   void CalcEnergy8ngbrs
35   (const Oxs_MeshValue<ThreeVector>& spin,
36    const Oxs_MeshValue<REAL8m>& Ms_inverse,
37    const Oxs_RectangularMesh* mesh,
38    Oxs_MeshValue<REAL8m>& energy,
```

```
39     Oxs_MeshValue<ThreeVector>& field) const;
40 /*  void CalcEnergy2ndngbr
41    (const Oxs_MeshValue<ThreeVector>& spin,
42     const Oxs_MeshValue<REAL8m>& Ms_inverse,
43     const Oxs_RectangularMesh* mesh,
44     Oxs_MeshValue<REAL8m>& energy,
45     Oxs_MeshValue<ThreeVector>& field) const;*/
46
47 protected:
48    virtual void GetEnergy(const Oxs_SimState& state,
49          Oxs_EnergyData& oed) const;
50
51 public:
52    virtual const char* ClassName() const; // ClassName() is
53    /// automatically generated by the OXS_EXT_REGISTER macro.
54    //Oxs_UniformExchange(const char* name,     // Child instance id
55    MM_1DExchange(const char* name,
56          Oxs_Director* newdtr, // App director
57          const char* argstr);  // MIF input block parameters
58    //virtual ~Oxs_UniformExchange();
59    virtual ~MM_1DExchange();
60
61    virtual BOOL Init();
62 };
63
64
65 #endif // _MM_UNIFORMEXCHANGE
```

```
1  /* FILE: my_1dexchange.cc                -*-Mode: c++-*-*/
2
3  #include "nb.h"
4  #include "director.h"
5  #include "mesh.h"
6  #include "meshvalue.h"
7  #include "simstate.h"
8  #include "threevector.h"
9  #include "rectangularmesh.h"
10 //#include "uniformexchange.h"
11 #include "my_1dexchange.h"
12 #include "energy.h"               // Needed to make MSVC++ 5 happy
13
14 // Oxs_Ext registration support
15 OXS_EXT_REGISTER(MM_1DExchange);
16
17 /* End includes */
18
19
20 // Constructor
21 MM_1DExchange::MM_1DExchange(
```

```
22    const char* name,       // Child instance id
23    Oxs_Director* newdtr, // App director
24    const char* argstr)    // MIF input block parameters
25    : Oxs_Energy(name,newdtr,argstr),
26      A1(0.), kernel(UNKNOWN)
27  {
28    // Process arguments
29    A1 = GetRealInitValue("A1");
30    A2 = GetRealInitValue("A2");
31    A3 = GetRealInitValue("A3");
32    A4 = GetRealInitValue("A4");
33    A5 = GetRealInitValue("A5");
34    A6 = GetRealInitValue("A6");
35    A7 = GetRealInitValue("A7");
36    A8 = GetRealInitValue("A8");
37    A9 = GetRealInitValue("A9");
38    A10 = GetRealInitValue("A10");
39    string kernel_request = GetStringInitValue("kernel","6ngbr");
40    if(kernel_request.compare("6ngbr")==0) {
41      kernel = NGBR_6;
42    } else {
43      string msg=string("Invalid kernel request: ")
44        + kernel_request
45        + string("\n Should be one of 6ngbr, 12ngbr, 12ngbrmirror, or 26
              ngbr.");
46      throw Oxs_Ext::Error(this,msg.c_str());
47    }
48    VerifyAllInitArgsUsed();
49  }
50
51  MM_1DExchange::~MM_1DExchange()
52  {}
53
54  BOOL MM_1DExchange::Init()
55  {
56    return Oxs_Energy::Init();
57  }
58
59  void
60  MM_1DExchange::CalcEnergy8ngbrs(
61    const Oxs_MeshValue<ThreeVector>& spin,
62    const Oxs_MeshValue<REAL8m>& Ms_inverse,
63    const Oxs_RectangularMesh* mesh,
64    Oxs_MeshValue<REAL8m>& energy,
65    Oxs_MeshValue<ThreeVector>& field
66  )
67  const{
68    UINT4m xdim = mesh->DimX();
69    UINT4m ydim = mesh->DimY();
```

```
70    UINT4m zdim = mesh->DimZ();
71    UINT4m xydim = xdim*ydim;
72
73    const REAL8m hcoef=-2/MU0;
74    REAL8m prefx1 = -A1/(mesh->EdgeLengthX()*mesh->EdgeLengthX()); //
          defines prefactor: A1=J1/a
75    REAL8m prefy1 = -1e-10/(mesh->EdgeLengthY()*mesh->EdgeLengthY()); //set
           to fix, strong fm exchange -> biatomic
76    REAL8m prefz1 = -A1/(mesh->EdgeLengthZ()*mesh->EdgeLengthZ());
77    REAL8m prefx2 = -A2/(mesh->EdgeLengthX()*mesh->EdgeLengthX());
78    REAL8m prefy2 = -0/(mesh->EdgeLengthY()*mesh->EdgeLengthY());
79    REAL8m prefz2 = -0/(mesh->EdgeLengthZ()*mesh->EdgeLengthZ());
80    REAL8m prefx3 = -A3/(mesh->EdgeLengthX()*mesh->EdgeLengthX());
81    REAL8m prefy3 = -0/(mesh->EdgeLengthY()*mesh->EdgeLengthY());
82    REAL8m prefz3 = -0/(mesh->EdgeLengthZ()*mesh->EdgeLengthZ());
83    REAL8m prefx4 = -A4/(mesh->EdgeLengthX()*mesh->EdgeLengthX());
84    REAL8m prefy4 = -0/(mesh->EdgeLengthY()*mesh->EdgeLengthY());
85    REAL8m prefz4 = -0/(mesh->EdgeLengthZ()*mesh->EdgeLengthZ());
86    REAL8m prefx5 = -A5/(mesh->EdgeLengthX()*mesh->EdgeLengthX());
87    REAL8m prefy5 = -0/(mesh->EdgeLengthY()*mesh->EdgeLengthY());
88    REAL8m prefz5 = -0/(mesh->EdgeLengthZ()*mesh->EdgeLengthZ());
89    REAL8m prefx6 = -A6/(mesh->EdgeLengthX()*mesh->EdgeLengthX());
90    REAL8m prefy6 = -0/(mesh->EdgeLengthY()*mesh->EdgeLengthY());
91    REAL8m prefz6 = -0/(mesh->EdgeLengthZ()*mesh->EdgeLengthZ());
92    REAL8m prefx7 = -A7/(mesh->EdgeLengthX()*mesh->EdgeLengthX());
93    REAL8m prefy7 = -0/(mesh->EdgeLengthY()*mesh->EdgeLengthY());
94    REAL8m prefz7 = -0/(mesh->EdgeLengthZ()*mesh->EdgeLengthZ());
95    REAL8m prefx8 = -A8/(mesh->EdgeLengthX()*mesh->EdgeLengthX());
96    REAL8m prefy8 = -0/(mesh->EdgeLengthY()*mesh->EdgeLengthY());
97    REAL8m prefz8 = -0/(mesh->EdgeLengthZ()*mesh->EdgeLengthZ());
98    REAL8m prefx9 = -A9/(mesh->EdgeLengthX()*mesh->EdgeLengthX());
99    REAL8m prefy9 = -0/(mesh->EdgeLengthY()*mesh->EdgeLengthY());
100   REAL8m prefz9 = -0/(mesh->EdgeLengthZ()*mesh->EdgeLengthZ());
101   REAL8m prefx10 = -A10/(mesh->EdgeLengthX()*mesh->EdgeLengthX());
102   REAL8m prefy10 = -0/(mesh->EdgeLengthY()*mesh->EdgeLengthY());
103   REAL8m prefz10 = -0/(mesh->EdgeLengthZ()*mesh->EdgeLengthZ());
104
105   for(UINT4m z=0;z<zdim;z++) {
106     for(UINT4m y=0;y<ydim;y++) {
107       for(UINT4m x=0;x<xdim;x++) {
108         UINT4m i = mesh->Index(x,y,z); //i defines lattice position
109
110         REAL8m Msii = Ms_inverse[i]; //inverse of magnetic moment of Si
111         if (Msii == 0.0) {
112           energy[i]=0.0;
113           field[i].Set(0.,0.,0.);
114           continue;
115         }
116
```

```
117         ThreeVector base = spin[i]; //defines Si
118
119         ThreeVector sum1(0.,0.,0.);
120         if(x>0) {
121           UINT4m j = i-1;
122           if(Ms_inverse[j]!=0.0) {
123             sum1 = (spin[j] - base); //exchange to left atom if there is
                    one
124           }
125         }
126         if(x<xdim-1) {
127           UINT4m j = i+1;
128           if(Ms_inverse[j]!=0.0) {
129             sum1 += (spin[j] - base); //exchange to right atom if there
                    is one
130           }
131         }
132         sum1 *= prefx1; //sum of atoms in x
133
134         ThreeVector temp1(0.,0.,0.);
135         if(y>0) {
136           UINT4m j = i-xdim;
137           if(Ms_inverse[j]!=0.0) {
138             temp1 = (spin[j] - base); //exchange to lower atom if there
                    is one
139           }
140         }
141         if(y<ydim-1) {
142           UINT4m j = i+xdim;
143           if(Ms_inverse[j]!=0.0) {
144             temp1 += (spin[j] - base); //exchange to upper atom if there
                    is one
145           }
146         }
147         sum1 += prefy1*temp1; //sum of atoms in x and y
148
149         temp1.Set(0.,0.,0.);
150         if(z>0) {
151           UINT4m j = i-xydim;
152           if(Ms_inverse[j]!=0.0) {
153             temp1 = (spin[j] - base); //exchange to layer below if there
                    is one
154           }
155         }
156         if(z<zdim-1) {
157           UINT4m j = i+xydim;
158           if(Ms_inverse[j]!=0.0) {
159             temp1 += (spin[j] - base); //exchange to layer above if there
                     is one
```

```
160           }
161         }
162         sum1 += prefz1*temp1; //sum of all atoms (x,y and z)
163
164         ThreeVector sum2(0.,0.,0.);
165         if(x>1) {
166           UINT4m j = i-2;
167           if(Ms_inverse[j]!=0.0) {
168             sum2 = (spin[j] - base); //exchange to left atom if there is
                    one
169           }
170         }
171         if(x<xdim-2) {
172           UINT4m j = i+2;
173           if(Ms_inverse[j]!=0.0) {
174             sum2 += (spin[j] - base); //exchange to right atom if there
                    is one
175           }
176         }
177         sum2 *= prefx2; //sum of atoms in x
178
179         ThreeVector temp2(0.,0.,0.);
180         if(y>1) {
181           UINT4m j = i-xdim-1;
182           if(Ms_inverse[j]!=0.0) {
183             temp2 = (spin[j] - base); //exchange to lower atom if there
                    is one
184           }
185         }
186         if(y<ydim-2) {
187           UINT4m j = i+xdim+1;
188           if(Ms_inverse[j]!=0.0) {
189             temp2 += (spin[j] - base); //exchange to upper atom if there
                    is one
190           }
191         }
192         sum2 += prefy2*temp2; //sum of atoms in x and y
193
194         temp2.Set(0.,0.,0.);
195         if(z>1) {
196           UINT4m j = i-xydim-1;
197           if(Ms_inverse[j]!=0.0) {
198             temp2 = (spin[j] - base); //exchange to layer below if there
                    is one
199           }
200         }
201         if(z<zdim-2) {
202           UINT4m j = i+xydim+1;
203           if(Ms_inverse[j]!=0.0) {
```

```
204             temp2 += (spin[j] - base); //exchange to layer above if there
                    is one
205           }
206         }
207         sum2 += prefz2*temp2; //sum of all atoms (x,y and z)
208
209
210         ThreeVector sum3(0.,0.,0.);
211         if(x>2) {
212           UINT4m j = i-3;
213           if(Ms_inverse[j]!=0.0) {
214             sum3 = (spin[j] - base); //exchange to left atom if there is
                    one
215           }
216         }
217         if(x<xdim-3) {
218           UINT4m j = i+3;
219           if(Ms_inverse[j]!=0.0) {
220             sum3 += (spin[j] - base); //exchange to right atom if there
                    is one
221           }
222         }
223         sum3 *= prefx3; //sum of atoms in x
224
225         ThreeVector temp3(0.,0.,0.);
226         if(y>2) {
227           UINT4m j = i-xdim-2;
228           if(Ms_inverse[j]!=0.0) {
229             temp3 = (spin[j] - base); //exchange to lower atom if there
                    is one
230           }
231         }
232         if(y<ydim-3) {
233           UINT4m j = i+xdim+2;
234           if(Ms_inverse[j]!=0.0) {
235             temp3 += (spin[j] - base); //exchange to upper atom if there
                    is one
236           }
237         }
238         sum3 += prefy3*temp3; //sum of atoms in x and y
239
240         temp3.Set(0.,0.,0.);
241         if(z>0) {
242           UINT4m j = i-xydim-2;
243           if(Ms_inverse[j]!=0.0) {
244             temp3 = (spin[j] - base); //exchange to layer below if there
                    is one
245           }
246         }
```

```
247         if(z<zdim-3) {
248           UINT4m j = i+xydim+2;
249           if(Ms_inverse[j]!=0.0) {
250             temp3 += (spin[j] - base); //exchange to layer above if there
                    is one
251           }
252         }
253         sum3 += prefz3*temp3; //sum of all atoms (x,y and z)
254
255
256         ThreeVector sum4(0.,0.,0.);
257         if(x>3) {
258           UINT4m j = i-4;
259           if(Ms_inverse[j]!=0.0) {
260             sum4 = (spin[j] - base); //exchange to left atom if there is
                    one
261           }
262         }
263         if(x<xdim-4) {
264           UINT4m j = i+4;
265           if(Ms_inverse[j]!=0.0) {
266             sum4 += (spin[j] - base); //exchange to right atom if there
                    is one
267           }
268         }
269         sum4 *= prefx4; //sum of atoms in x
270
271         ThreeVector temp4(0.,0.,0.);
272         if(y>3) {
273           UINT4m j = i-xdim-3;
274           if(Ms_inverse[j]!=0.0) {
275             temp4 = (spin[j] - base); //exchange to lower atom if there
                    is one
276           }
277         }
278         if(y<ydim-4) {
279           UINT4m j = i+xdim+3;
280           if(Ms_inverse[j]!=0.0) {
281             temp4 += (spin[j] - base); //exchange to upper atom if there
                    is one
282           }
283         }
284         sum4 += prefy4*temp4; //sum of atoms in x and y
285
286         temp4.Set(0.,0.,0.);
287         if(z>0) {
288           UINT4m j = i-xydim-3;
289           if(Ms_inverse[j]!=0.0) {
290             temp4 = (spin[j] - base); //exchange to layer below if there
```

```
                is one
291           }
292         }
293         if(z<zdim-4) {
294           UINT4m j = i+xydim+3;
295           if(Ms_inverse[j]!=0.0) {
296             temp4 += (spin[j] - base); //exchange to layer above if there
                    is one
297           }
298         }
299         sum4 += prefz4*temp4; //sum of all atoms (x,y and z)
300
301
302         ThreeVector sum5(0.,0.,0.);
303         if(x>4) {
304           UINT4m j = i-5;
305           if(Ms_inverse[j]!=0.0) {
306             sum5 = (spin[j] - base); //exchange to left atom if there is
                  one
307           }
308         }
309         if(x<xdim-5) {
310           UINT4m j = i+5;
311           if(Ms_inverse[j]!=0.0) {
312             sum5 += (spin[j] - base); //exchange to right atom if there
                  is one
313           }
314         }
315         sum5 *= prefx5; //sum of atoms in x
316
317         ThreeVector temp5(0.,0.,0.);
318         if(y>4) {
319           UINT4m j = i-xdim-4;
320           if(Ms_inverse[j]!=0.0) {
321             temp5 = (spin[j] - base); //exchange to lower atom if there
                  is one
322           }
323         }
324         if(y<ydim-5) {
325           UINT4m j = i+xdim+4;
326           if(Ms_inverse[j]!=0.0) {
327             temp5 += (spin[j] - base); //exchange to upper atom if there
                  is one
328           }
329         }
330         sum5 += prefy5*temp5; //sum of atoms in x and y
331
332         temp5.Set(0.,0.,0.);
333         if(z>0) {
```

```
334           UINT4m j = i-xydim-4;
335           if(Ms_inverse[j]!=0.0) {
336             temp5 = (spin[j] - base); //exchange to layer below if there
                  is one
337           }
338         }
339         if(z<zdim-5) {
340           UINT4m j = i+xydim+4;
341           if(Ms_inverse[j]!=0.0) {
342             temp5 += (spin[j] - base); //exchange to layer above if there
                   is one
343           }
344         }
345         sum5 += prefz5*temp5; //sum of all atoms (x,y and z)
346
347
348         ThreeVector sum6(0.,0.,0.);
349         if(x>5) {
350           UINT4m j = i-6;
351           if(Ms_inverse[j]!=0.0) {
352             sum6 = (spin[j] - base); //exchange to left atom if there is
                  one
353           }
354         }
355         if(x<xdim-6) {
356           UINT4m j = i+6;
357           if(Ms_inverse[j]!=0.0) {
358             sum6 += (spin[j] - base); //exchange to right atom if there
                  is one
359           }
360         }
361         sum6 *= prefx6; //sum of atoms in x
362
363         ThreeVector temp6(0.,0.,0.);
364         if(y>5) {
365           UINT4m j = i-xdim-5;
366           if(Ms_inverse[j]!=0.0) {
367             temp6 = (spin[j] - base); //exchange to lower atom if there
                  is one
368           }
369         }
370         if(y<ydim-6) {
371           UINT4m j = i+xdim+5;
372           if(Ms_inverse[j]!=0.0) {
373             temp6 += (spin[j] - base); //exchange to upper atom if there
                  is one
374           }
375         }
376         sum6 += prefy6*temp6; //sum of atoms in x and y
```

```
377
378         temp6.Set(0.,0.,0.);
379         if(z>0) {
380           UINT4m j = i-xydim-5;
381           if(Ms_inverse[j]!=0.0) {
382             temp6 = (spin[j] - base); //exchange to layer below if there
                    is one
383           }
384         }
385         if(z<zdim-6) {
386           UINT4m j = i+xydim+5;
387           if(Ms_inverse[j]!=0.0) {
388             temp6 += (spin[j] - base); //exchange to layer above if there
                     is one
389           }
390         }
391         sum6 += prefz6*temp6; //sum of all atoms (x,y and z)
392
393
394         ThreeVector sum7(0.,0.,0.);
395         if(x>6) {
396           UINT4m j = i-7;
397           if(Ms_inverse[j]!=0.0) {
398             sum7 = (spin[j] - base); //exchange to left atom if there is
                    one
399           }
400         }
401         if(x<xdim-7) {
402           UINT4m j = i+7;
403           if(Ms_inverse[j]!=0.0) {
404             sum7 += (spin[j] - base); //exchange to right atom if there
                    is one
405           }
406         }
407         sum7 *= prefx7; //sum of atoms in x
408
409         ThreeVector temp7(0.,0.,0.);
410         if(y>6) {
411           UINT4m j = i-xdim-6;
412           if(Ms_inverse[j]!=0.0) {
413             temp7 = (spin[j] - base); //exchange to lower atom if there
                    is one
414           }
415         }
416         if(y<ydim-7) {
417           UINT4m j = i+xdim+6;
418           if(Ms_inverse[j]!=0.0) {
419             temp7 += (spin[j] - base); //exchange to upper atom if there
                    is one
```

```
420           }
421         }
422         sum7 += prefy7*temp7; //sum of atoms in x and y
423
424         temp7.Set(0.,0.,0.);
425         if(z>6) {
426           UINT4m j = i-xydim-6;
427           if(Ms_inverse[j]!=0.0) {
428             temp7 = (spin[j] - base); //exchange to layer below if there
                    is one
429           }
430         }
431         if(z<zdim-7) {
432           UINT4m j = i+xydim+6;
433           if(Ms_inverse[j]!=0.0) {
434             temp7 += (spin[j] - base); //exchange to layer above if there
                     is one
435           }
436         }
437
438         sum7 += prefz7*temp7; //sum of all atoms (x,y and z)
439
440
441         ThreeVector sum8(0.,0.,0.);
442         if(x>7) {
443           UINT4m j = i-8;
444           if(Ms_inverse[j]!=0.0) {
445             sum8 = (spin[j] - base); //exchange to left atom if there is
                    one
446           }
447         }
448         if(x<xdim-8) {
449           UINT4m j = i+8;
450           if(Ms_inverse[j]!=0.0) {
451             sum8 += (spin[j] - base); //exchange to right atom if there
                    is one
452           }
453         }
454         sum8 *= prefx8; //sum of atoms in x
455
456         ThreeVector temp8(0.,0.,0.);
457         if(y>7) {
458           UINT4m j = i-xdim-7;
459           if(Ms_inverse[j]!=0.0) {
460             temp8 = (spin[j] - base); //exchange to lower atom if there
                    is one
461           }
462         }
463         if(y<ydim-8) {
```

```
464           UINT4m j = i+xdim+7;
465           if(Ms_inverse[j]!=0.0) {
466             temp8 += (spin[j] - base); //exchange to upper atom if there
                  is one
467           }
468         }
469         sum8 += prefy8*temp8; //sum of atoms in x and y
470
471         temp8.Set(0.,0.,0.);
472         if(z>7) {
473           UINT4m j = i-xydim-7;
474           if(Ms_inverse[j]!=0.0) {
475             temp8 = (spin[j] - base); //exchange to layer below if there
                  is one
476           }
477         }
478         if(z<zdim-8) {
479           UINT4m j = i+xydim+7;
480           if(Ms_inverse[j]!=0.0) {
481             temp8 += (spin[j] - base); //exchange to layer above if there
                   is one
482           }
483         }
484         sum8 += prefz8*temp8; //sum of all atoms (x,y and z)
485
486
487         ThreeVector sum9(0.,0.,0.);
488         if(x>8) {
489           UINT4m j = i-9;
490           if(Ms_inverse[j]!=0.0) {
491             sum9 = (spin[j] - base); //exchange to left atom if there is
                  one
492           }
493         }
494         if(x<xdim-9) {
495           UINT4m j = i+9;
496           if(Ms_inverse[j]!=0.0) {
497             sum9 += (spin[j] - base); //exchange to right atom if there
                  is one
498           }
499         }
500         sum9 *= prefx9; //sum of atoms in x
501
502         ThreeVector temp9(0.,0.,0.);
503         if(y>8) {
504           UINT4m j = i-xdim-8;
505           if(Ms_inverse[j]!=0.0) {
506             temp9 = (spin[j] - base); //exchange to lower atom if there
                  is one
```

```
507             }
508           }
509           if(y<ydim-9) {
510             UINT4m j = i+xdim+8;
511             if(Ms_inverse[j]!=0.0) {
512               temp9 += (spin[j] - base); //exchange to upper atom if there
                      is one
513             }
514           }
515           sum9 += prefy9*temp9; //sum of atoms in x and y
516
517           temp9.Set(0.,0.,0.);
518           if(z>8) {
519             UINT4m j = i-xydim-8;
520             if(Ms_inverse[j]!=0.0) {
521               temp9 = (spin[j] - base); //exchange to layer below if there
                      is one
522             }
523           }
524           if(z<zdim-9) {
525             UINT4m j = i+xydim+8;
526             if(Ms_inverse[j]!=0.0) {
527               temp9 += (spin[j] - base); //exchange to layer above if there
                       is one
528             }
529           }
530           sum9 += prefz9*temp9; //sum of all atoms (x,y and z)
531
532
533           ThreeVector sum10(0.,0.,0.);
534           if(x>9) {
535             UINT4m j = i-10;
536             if(Ms_inverse[j]!=0.0) {
537               sum10 = (spin[j] - base); //exchange to left atom if there is
                       one
538             }
539           }
540           if(x<xdim-10) {
541             UINT4m j = i+10;
542             if(Ms_inverse[j]!=0.0) {
543               sum10 += (spin[j] - base); //exchange to right atom if there
                      is one
544             }
545           }
546           sum10 *= prefx10; //sum of atoms in x
547
548           ThreeVector temp10(0.,0.,0.);
549           if(y>9) {
550             UINT4m j = i-xdim-9;
```

```
551             if(Ms_inverse[j]!=0.0) {
552               temp10 = (spin[j] - base); //exchange to lower atom if there
                      is one
553             }
554           }
555           if(y<ydim-10) {
556             UINT4m j = i+xdim+9;
557             if(Ms_inverse[j]!=0.0) {
558               temp10 += (spin[j] - base); //exchange to upper atom if there
                      is one
559             }
560           }
561           sum10 += prefy10*temp10; //sum of atoms in x and y
562
563           temp10.Set(0.,0.,0.);
564           if(z>9) {
565             UINT4m j = i-xydim-9;
566             if(Ms_inverse[j]!=0.0) {
567               temp10 = (spin[j] - base); //exchange to layer below if there
                      is one
568             }
569           }
570           if(z<zdim-10) {
571             UINT4m j = i+xydim+9;
572             if(Ms_inverse[j]!=0.0) {
573               temp10 += (spin[j] - base); //exchange to layer above if
                      there is one
574             }
575           }
576           sum10 += prefz10*temp10; //sum of all atoms (x,y and z)
577
578
579           ThreeVector sum(0.,0.,0.);
580
581           sum = (sum1 + sum2 + sum3 + sum4 + sum5 + sum6 + sum7 + sum8 +
                  sum9 + sum10);
582
583           field[i] = ((hcoef*Msii) * sum); //im not sure, force acting on
                  atom j due to exchange??
584           energy[i] = (sum * base); //exchange energy for atom i
585         }
586       }
587     }
588 }
589
590 void MM_1DExchange::GetEnergy
591 (const Oxs_SimState& state,
592  Oxs_EnergyData& oed
593  ) const
```

```
594 {
595   const Oxs_MeshValue<ThreeVector>& spin = state.spin;
596   const Oxs_MeshValue<REAL8m>& Ms_inverse = *(state.Ms_inverse);
597
598   // Use supplied buffer space, and reflect that use in oed.
599   oed.energy = oed.energy_buffer;
600   oed.field = oed.field_buffer;
601   Oxs_MeshValue<REAL8m>& energy = *oed.energy_buffer;
602   Oxs_MeshValue<ThreeVector>& field = *oed.field_buffer;
603
604   const Oxs_RectangularMesh* mesh
605     = dynamic_cast<const Oxs_RectangularMesh*>(state.mesh);
606   if(mesh==NULL) {
607     throw Oxs_Ext::Error(this,"Import mesh to"
608                          " Oxs_UniformExchange::GetEnergy()"
609                          " is not an Oxs_RectangularMesh object.");
610   }
611
612   // Note: Might want to consider subclassing exchange energies,
613   //  to replace this if-block with virtual function pointers.
614   if(kernel == NGBR_6) {
615     CalcEnergy8ngbrs(spin,Ms_inverse,mesh,energy,field);
616   } else {
617     throw Oxs_Ext::Error(this,"Invalid kernel type detected."
618                          "  (Programming error)");
619   }
620
621 }
```

```
 1 /* FILE: my_dzyamoexchange.h                -*-Mode: c++-*-*/
 2
 3 #ifndef _MM_DZYAMOEXCHANGE
 4 #define _MM_DZYAMOEXCHANGE
 5
 6 #include "oc.h"
 7 #include "director.h"
 8 #include "energy.h"
 9 #include "meshvalue.h"
10 #include "simstate.h"
11 #include "threevector.h"
12
13 /* End includes */
14
15 class MM_DzyaMoExchange:public Oxs_Energy{
16 private:
17   REAL8m D1;
18   REAL8m D2;
19   REAL8m D3;
20   REAL8m D4;
```

```
21    REAL8m D5;
22    REAL8m D6;
23    REAL8m D7;
24    REAL8m D8;
25    REAL8m D9;
26    REAL8m D10;
27
28    enum ExchangeKernel { UNKNOWN, NGBR_6} kernel;
29    /// Exchange formulation to use.  "unknown" is invalid; it
30    /// is defined for error detection.
31
32    // Calculation routines for each of the
33    // aforementioned energy formulations.
34    void CalcEnergyDzyaMo
35    (const Oxs_MeshValue<ThreeVector>& spin,
36     const Oxs_MeshValue<REAL8m>& Ms_inverse,
37     const Oxs_RectangularMesh* mesh,
38     Oxs_MeshValue<REAL8m>& energy,
39     Oxs_MeshValue<ThreeVector>& field) const;
40
41 protected:
42    virtual void GetEnergy(const Oxs_SimState& state,
43         Oxs_EnergyData& oed) const;
44
45 public:
46    virtual const char* ClassName() const; // ClassName() is
47    /// automatically generated by the OXS_EXT_REGISTER macro.
48    //Oxs_UniformExchange(const char* name,     // Child instance id
49    MM_DzyaMoExchange(const char* name,
50          Oxs_Director* newdtr, // App director
51          const char* argstr);  // MIF input block parameters
52    //virtual ~Oxs_UniformExchange();
53    virtual ~MM_DzyaMoExchange();
54
55    virtual BOOL Init();
56 };
57
58
59 #endif // _MM_DZYAMOEXCHANGE
```

```
1  /* FILE: my_dzyamoexchange.cc                -*-Mode: c++-*-*/
2
3  #include "nb.h"
4  #include "director.h"
5  #include "mesh.h"
6  #include "meshvalue.h"
7  #include "simstate.h"
8  #include "threevector.h"
9  #include "rectangularmesh.h"
```

```
10 //#include "uniformexchange.h"
11 #include "my_dzyamoexchange.h"
12 #include "energy.h"                // Needed to make MSVC++ 5 happy
13
14 // Oxs_Ext registration support
15 OXS_EXT_REGISTER(MM_DzyaMoExchange);
16
17 /* End includes */
18
19
20 // Constructor
21 MM_DzyaMoExchange::MM_DzyaMoExchange(
22   const char* name,      // Child instance id
23   Oxs_Director* newdtr, // App director
24   const char* argstr)    // MIF input block parameters
25   : Oxs_Energy(name,newdtr,argstr),
26     D1(0.), kernel(UNKNOWN)
27 {
28   // Process arguments
29   D1 = GetRealInitValue("D1");
30   D2 = GetRealInitValue("D2");
31   D3 = GetRealInitValue("D3");
32   D4 = GetRealInitValue("D4");
33   D5 = GetRealInitValue("D5");
34   D6 = GetRealInitValue("D6");
35   D7 = GetRealInitValue("D7");
36   D8 = GetRealInitValue("D8");
37   D9 = GetRealInitValue("D9");
38   D10 = GetRealInitValue("D10");
39   string kernel_request = GetStringInitValue("kernel","6ngbr");
40   if(kernel_request.compare("6ngbr")==0) {
41     kernel = NGBR_6;
42   } else {
43     string msg=string("Invalid kernel request: ")
44       + kernel_request
45       + string("\n Should be one of 6ngbr, 12ngbr, 12ngbrmirror, or 26
             ngbr.");
46     throw Oxs_Ext::Error(this,msg.c_str());
47   }
48   VerifyAllInitArgsUsed();
49 }
50
51 MM_DzyaMoExchange::~MM_DzyaMoExchange()
52 {}
53
54 BOOL MM_DzyaMoExchange::Init()
55 {
56   return Oxs_Energy::Init();
57 }
```

```
58
59 void
60 MM_DzyaMoExchange::CalcEnergyDzyaMo(
61    const Oxs_MeshValue<ThreeVector>& spin,
62    const Oxs_MeshValue<REAL8m>& Ms_inverse,
63    const Oxs_RectangularMesh* mesh,
64    Oxs_MeshValue<REAL8m>& energy,
65    Oxs_MeshValue<ThreeVector>& field
66 )
67 const
68 {
69    UINT4m xdim = mesh->DimX();
70    UINT4m ydim = mesh->DimY();
71    UINT4m zdim = mesh->DimZ();
72    UINT4m xydim = xdim*ydim;
73
74    const REAL8m hcoef = -2/MU0;
75    ThreeVector DM(0.,1.,0);
76
77    REAL8m prefx1 = D1/(mesh->EdgeLengthX()*mesh->EdgeLengthX()); //perhaps
          different prefactors
78    REAL8m prefy1 = D1/(mesh->EdgeLengthY()*mesh->EdgeLengthY()); //for
          different directions?
79    REAL8m prefz1 = D1/(mesh->EdgeLengthZ()*mesh->EdgeLengthZ());
80    REAL8m prefx2 = D2/(mesh->EdgeLengthX()*mesh->EdgeLengthX());
81    REAL8m prefy2 = 0/(mesh->EdgeLengthY()*mesh->EdgeLengthY());
82    REAL8m prefz2 = 0/(mesh->EdgeLengthZ()*mesh->EdgeLengthZ());
83    REAL8m prefx3 = D3/(mesh->EdgeLengthX()*mesh->EdgeLengthX());
84    REAL8m prefy3 = 0/(mesh->EdgeLengthY()*mesh->EdgeLengthY());
85    REAL8m prefz3 = 0/(mesh->EdgeLengthZ()*mesh->EdgeLengthZ());
86    REAL8m prefx4 = D4/(mesh->EdgeLengthX()*mesh->EdgeLengthX());
87    REAL8m prefy4 = 0/(mesh->EdgeLengthY()*mesh->EdgeLengthY());
88    REAL8m prefz4 = 0/(mesh->EdgeLengthZ()*mesh->EdgeLengthZ());
89    REAL8m prefx5 = D5/(mesh->EdgeLengthX()*mesh->EdgeLengthX());
90    REAL8m prefy5 = 0/(mesh->EdgeLengthY()*mesh->EdgeLengthY());
91    REAL8m prefz5 = 0/(mesh->EdgeLengthZ()*mesh->EdgeLengthZ());
92    REAL8m prefx6 = D6/(mesh->EdgeLengthX()*mesh->EdgeLengthX());
93    REAL8m prefy6 = 0/(mesh->EdgeLengthY()*mesh->EdgeLengthY());
94    REAL8m prefz6 = 0/(mesh->EdgeLengthZ()*mesh->EdgeLengthZ());
95    REAL8m prefx7 = D7/(mesh->EdgeLengthX()*mesh->EdgeLengthX());
96    REAL8m prefy7 = 0/(mesh->EdgeLengthY()*mesh->EdgeLengthY());
97    REAL8m prefz7 = 0/(mesh->EdgeLengthZ()*mesh->EdgeLengthZ());
98    REAL8m prefx8 = D8/(mesh->EdgeLengthX()*mesh->EdgeLengthX());
99    REAL8m prefy8 = 0/(mesh->EdgeLengthY()*mesh->EdgeLengthY());
100   REAL8m prefz8 = 0/(mesh->EdgeLengthZ()*mesh->EdgeLengthZ());
101   REAL8m prefx9 = D9/(mesh->EdgeLengthX()*mesh->EdgeLengthX());
102   REAL8m prefy9 = 0/(mesh->EdgeLengthY()*mesh->EdgeLengthY());
103   REAL8m prefz9 = 0/(mesh->EdgeLengthZ()*mesh->EdgeLengthZ());
104   REAL8m prefx10 = D10/(mesh->EdgeLengthX()*mesh->EdgeLengthX());
```

```
105   REAL8m prefy10 = 0/(mesh->EdgeLengthY()*mesh->EdgeLengthY());
106   REAL8m prefz10 = 0/(mesh->EdgeLengthZ()*mesh->EdgeLengthZ());
107
108   for(UINT4m z=0;z<zdim;z++) {
109     for(UINT4m y=0;y<ydim;y++) {
110       for(UINT4m x=0;x<xdim;x++) {
111         UINT4m i = mesh->Index(x,y,z); //i defines lattice position
112
113         REAL8m Msii = Ms_inverse[i]; //inverse of magnetic moment of Si
114         if (Msii == 0.0) {
115           energy[i]=0.0;
116           field[i].Set(0.,0.,0.);
117           continue;
118         }
119
120         ThreeVector base = spin[i]; //defines Si
121
122         REAL8m sum1 = 0; //energy part
123         ThreeVector fieldpart1(0.,0.,0.); //field part
124         if(x>0) {
125           UINT4m j = i-1;
126           if(Ms_inverse[j]!=0) {
127             sum1 = ( DM * (base ^ spin[j])); //varies between 0 and 2
128             fieldpart1 = (spin[j] ^ DM); //maybe fill in +1 or -1 to
                  offset to zero??
129           }
130         }
131         if(x<xdim-1) {
132           UINT4m j = i+1;
133           if(Ms_inverse[j]!=0) {
134             sum1 += (DM * (spin[j] ^ base)); //rotated due to symmetry
                  reasons
135             fieldpart1 += (DM ^ spin[j]);
136           }
137         }
138
139         sum1 *= prefx1;
140         fieldpart1 *= prefx1;
141
142         REAL8m temp1 = 0;
143         ThreeVector fieldtemp1(0.,0.,0.);
144         if(y>0) {
145           UINT4m j = i-xdim;
146           if(Ms_inverse[j]!=0) {
147             temp1 = (DM * (base ^ spin[j]));
148             fieldtemp1 = (spin[j] ^ DM);
149           }
150         }
151         if(y<ydim-1) {
```

```
152             UINT4m j = i+xdim;
153             if(Ms_inverse[j]!=0) {
154               temp1 += (DM * (spin[j] ^ base));
155               fieldtemp1 += (DM ^ spin[j]);
156             }
157           }
158
159           sum1 += temp1 * prefy1;
160           fieldpart1 += fieldtemp1 * prefy1;
161
162           temp1 = 0;
163           fieldtemp1.Set(0.,0.,0.);
164           if(z>0) {
165             UINT4m j = i-xydim;
166             if(Ms_inverse[j]!=0) {
167               temp1 = (DM * (base ^ spin[j]));
168               fieldtemp1 = (spin[j] ^ DM);
169             }
170           }
171           if(z<zdim-1) {
172             UINT4m j = i+xydim;
173             if(Ms_inverse[j]!=0) {
174               temp1 += (DM * (spin[j] ^ base));
175               fieldtemp1 += (DM ^ spin[j]);
176             }
177           }
178
179           sum1 += temp1 * prefz1;
180           fieldpart1 += fieldtemp1 * prefz1;
181
182
183           REAL8m sum2 = 0; //energy part
184           ThreeVector fieldpart2(0.,0.,0.); //field part
185           if(x>1) {
186             UINT4m j = i-2;
187             if(Ms_inverse[j]!=0) {
188               sum2 = ( DM * (base ^ spin[j])); //varies between 0 and 2
189               fieldpart2 = (spin[j] ^ DM); //maybe fill in +1 or -1 to
                      offset to zero??
190             }
191           }
192           if(x<xdim-2) {
193             UINT4m j = i+2;
194             if(Ms_inverse[j]!=0) {
195               sum2 += (DM * (spin[j] ^ base)); //rotated due to symmetry
                      reasons
196               fieldpart2 += (DM ^ spin[j]);
197             }
198           }
```

```
199
200         sum2 *= prefx2;
201         fieldpart2 *= prefx2;
202
203         REAL8m temp2 = 0;
204         ThreeVector fieldtemp2(0.,0.,0.);
205         if(y>1) {
206           UINT4m j = i-xdim-1;
207           if(Ms_inverse[j]!=0) {
208             temp2 = (DM * (base ^ spin[j]));
209             fieldtemp2 = (spin[j] ^ DM);
210           }
211         }
212         if(y<ydim-2) {
213           UINT4m j = i+xdim+1;
214           if(Ms_inverse[j]!=0) {
215             temp2 += (DM * (spin[j] ^ base));
216             fieldtemp2 += (DM ^ spin[j]);
217           }
218         }
219
220         sum2 += temp2 * prefy2;
221         fieldpart2 += fieldtemp2 * prefy2;
222
223         temp2 = 0;
224         fieldtemp2.Set(0.,0.,0.);
225         if(z>1) {
226           UINT4m j = i-xydim-1;
227           if(Ms_inverse[j]!=0) {
228             temp2 = (DM * (base ^ spin[j]));
229             fieldtemp2 = (spin[j] ^ DM);
230           }
231         }
232         if(z<zdim-2) {
233           UINT4m j = i+xydim+1;
234           if(Ms_inverse[j]!=0) {
235             temp2 += (DM * (spin[j] ^ base));
236             fieldtemp2 += (DM ^ spin[j]);
237           }
238         }
239
240         sum2 += temp2 * prefz2;
241         fieldpart2 += fieldtemp2 * prefz2;
242
243         REAL8m sum3 = 0; //energy part
244         ThreeVector fieldpart3(0.,0.,0.); //field part
245         if(x>2) {
246           UINT4m j = i-3;
247           if(Ms_inverse[j]!=0) {
```

```
248             sum3 = ( DM * (base ^ spin[j])); //varies between 0 and 2
249             fieldpart3 = (spin[j] ^ DM); //maybe fill in +1 or -1 to
                    offset to zero??
250           }
251         }
252         if(x<xdim-3) {
253           UINT4m j = i+3;
254           if(Ms_inverse[j]!=0) {
255             sum3 += (DM * (spin[j] ^ base)); //rotated due to symmetry
                    reasons
256             fieldpart3 += (DM ^ spin[j]);
257           }
258         }
259
260         sum3 *= prefx3;
261         fieldpart3 *= prefx3;
262
263         REAL8m temp3 = 0;
264         ThreeVector fieldtemp3(0.,0.,0.);
265         if(y>2) {
266           UINT4m j = i-xdim-2;
267           if(Ms_inverse[j]!=0) {
268             temp3 = (DM * (base ^ spin[j]));
269             fieldtemp3 = (spin[j] ^ DM);
270           }
271         }
272         if(y<ydim-3) {
273           UINT4m j = i+xdim+2;
274           if(Ms_inverse[j]!=0) {
275             temp3 += (DM * (spin[j] ^ base));
276             fieldtemp3 += (DM ^ spin[j]);
277           }
278         }
279
280         sum3 += temp3 * prefy3;
281         fieldpart3 += fieldtemp3 * prefy3;
282
283         temp3 = 0;
284         fieldtemp3.Set(0.,0.,0.);
285         if(z>2) {
286           UINT4m j = i-xydim-2;
287           if(Ms_inverse[j]!=0) {
288             temp3 = (DM * (base ^ spin[j]));
289             fieldtemp3 = (spin[j] ^ DM);
290           }
291         }
292         if(z<zdim-3) {
293           UINT4m j = i+xydim+2;
294           if(Ms_inverse[j]!=0) {
```

```
295             temp3 += (DM * (spin[j] ^ base));
296             fieldtemp3 += (DM ^ spin[j]);
297           }
298         }
299
300         sum3 += temp3 * prefz3;
301         fieldpart3 += fieldtemp3 * prefz3;
302
303
304         REAL8m sum4 = 0; //energy part
305         ThreeVector fieldpart4(0.,0.,0.); //field part
306         if(x>3) {
307           UINT4m j = i-4;
308           if(Ms_inverse[j]!=0) {
309             sum4 = ( DM * (base ^ spin[j])); //varies between 0 and 2
310             fieldpart4 = (spin[j] ^ DM); //maybe fill in +1 or -1 to
                  offset to zero??
311           }
312         }
313         if(x<xdim-4) {
314           UINT4m j = i+4;
315           if(Ms_inverse[j]!=0) {
316             sum4 += (DM * (spin[j] ^ base)); //rotated due to symmetry
                  reasons
317             fieldpart4 += (DM ^ spin[j]);
318           }
319         }
320
321         sum4 *= prefx4;
322         fieldpart4 *= prefx4;
323
324         REAL8m temp4 = 0;
325         ThreeVector fieldtemp4(0.,0.,0.);
326         if(y>3) {
327           UINT4m j = i-xdim-3;
328           if(Ms_inverse[j]!=0) {
329             temp4 = (DM * (base ^ spin[j]));
330             fieldtemp4 = (spin[j] ^ DM);
331           }
332         }
333         if(y<ydim-4) {
334           UINT4m j = i+xdim+3;
335           if(Ms_inverse[j]!=0) {
336             temp4 += (DM * (spin[j] ^ base));
337             fieldtemp4 += (DM ^ spin[j]);
338           }
339         }
340
341         sum4 += temp4 * prefy4;
```

```
342         fieldpart4 += fieldtemp4 * prefy4;
343
344         temp4 = 0;
345         fieldtemp4.Set(0.,0.,0.);
346         if(z>3) {
347           UINT4m j = i-xydim-3;
348           if(Ms_inverse[j]!=0) {
349             temp4 = (DM * (base ^ spin[j]));
350             fieldtemp4 = (spin[j] ^ DM);
351           }
352         }
353         if(z<zdim-4) {
354           UINT4m j = i+xydim+3;
355           if(Ms_inverse[j]!=0) {
356             temp4 += (DM * (spin[j] ^ base));
357             fieldtemp4 += (DM ^ spin[j]);
358           }
359         }
360
361         sum4 += temp4 * prefz4;
362         fieldpart4 += fieldtemp4 * prefz4;
363
364
365         REAL8m sum5 = 0; //energy part
366         ThreeVector fieldpart5(0.,0.,0.); //field part
367         if(x>4) {
368           UINT4m j = i-5;
369           if(Ms_inverse[j]!=0) {
370             sum5 = ( DM * (base ^ spin[j])); //varies between 0 and 2
371             fieldpart5 = (spin[j] ^ DM); //maybe fill in +1 or -1 to
                  offset to zero??
372           }
373         }
374         if(x<xdim-5) {
375           UINT4m j = i+5;
376           if(Ms_inverse[j]!=0) {
377             sum5 += (DM * (spin[j] ^ base)); //rotated due to symmetry
                  reasons
378             fieldpart5 += (DM ^ spin[j]);
379           }
380         }
381
382         sum5 *= prefx5;
383         fieldpart5 *= prefx5;
384
385         REAL8m temp5 = 0;
386         ThreeVector fieldtemp5(0.,0.,0.);
387         if(y>4) {
388           UINT4m j = i-xdim-4;
```

```
389             if(Ms_inverse[j]!=0) {
390               temp5 = (DM * (base ^ spin[j]));
391               fieldtemp5 = (spin[j] ^ DM);
392             }
393           }
394           if(y<ydim-5) {
395             UINT4m j = i+xdim+4;
396             if(Ms_inverse[j]!=0) {
397               temp5 += (DM * (spin[j] ^ base));
398               fieldtemp5 += (DM ^ spin[j]);
399             }
400           }
401
402           sum5 += temp5 * prefy5;
403           fieldpart5 += fieldtemp5 * prefy5;
404
405           temp5 = 0;
406           fieldtemp5.Set(0.,0.,0.);
407           if(z>4) {
408             UINT4m j = i-xydim-4;
409             if(Ms_inverse[j]!=0) {
410               temp5 = (DM * (base ^ spin[j]));
411               fieldtemp5 = (spin[j] ^ DM);
412             }
413           }
414           if(z<zdim-5) {
415             UINT4m j = i+xydim+4;
416             if(Ms_inverse[j]!=0) {
417               temp5 += (DM * (spin[j] ^ base));
418               fieldtemp5 += (DM ^ spin[j]);
419             }
420           }
421
422           sum5 += temp5 * prefz5;
423           fieldpart5 += fieldtemp5 * prefz5;
424
425
426           REAL8m sum6 = 0; //energy part
427           ThreeVector fieldpart6(0.,0.,0.); //field part
428           if(x>5) {
429             UINT4m j = i-6;
430             if(Ms_inverse[j]!=0) {
431               sum6 = ( DM * (base ^ spin[j])); //varies between 0 and 2
432               fieldpart6 = (spin[j] ^ DM); //maybe fill in +1 or -1 to
                      offset to zero??
433             }
434           }
435           if(x<xdim-6) {
436             UINT4m j = i+6;
```

```
437             if(Ms_inverse[j]!=0) {
438               sum6 += (DM * (spin[j] ^ base)); //rotated due to symmetry
                      reasons
439               fieldpart6 += (DM ^ spin[j]);
440             }
441           }
442
443           sum6 *= prefx6;
444           fieldpart6 *= prefx6;
445
446           REAL8m temp6 = 0;
447           ThreeVector fieldtemp6(0.,0.,0.);
448           if(y>5) {
449             UINT4m j = i-xdim-5;
450             if(Ms_inverse[j]!=0) {
451               temp6 = (DM * (base ^ spin[j]));
452               fieldtemp6 = (spin[j] ^ DM);
453             }
454           }
455           if(y<ydim-6) {
456             UINT4m j = i+xdim+5;
457             if(Ms_inverse[j]!=0) {
458               temp6 += (DM * (spin[j] ^ base));
459               fieldtemp6 += (DM ^ spin[j]);
460             }
461           }
462
463           sum6 += temp6 * prefy6;
464           fieldpart6 += fieldtemp6 * prefy6;
465
466           temp6 = 0;
467           fieldtemp6.Set(0.,0.,0.);
468           if(z>5) {
469             UINT4m j = i-xydim-5;
470             if(Ms_inverse[j]!=0) {
471               temp6 = (DM * (base ^ spin[j]));
472               fieldtemp6 = (spin[j] ^ DM);
473             }
474           }
475           if(z<zdim-6) {
476             UINT4m j = i+xydim+5;
477             if(Ms_inverse[j]!=0) {
478               temp6 += (DM * (spin[j] ^ base));
479               fieldtemp6 += (DM ^ spin[j]);
480             }
481           }
482
483           sum6 += temp6 * prefz6;
484           fieldpart6 += fieldtemp6 * prefz6;
```

```
485
486
487         REAL8m sum7 = 0; //energy part
488         ThreeVector fieldpart7(0.,0.,0.); //field part
489         if(x>6) {
490           UINT4m j = i-7;
491           if(Ms_inverse[j]!=0) {
492             sum7 = ( DM * (base ^ spin[j])); //varies between 0 and 2
493             fieldpart7 = (spin[j] ^ DM); //maybe fill in +1 or -1 to
                  offset to zero??
494           }
495         }
496         if(x<xdim-7) {
497           UINT4m j = i+7;
498           if(Ms_inverse[j]!=0) {
499             sum7 += (DM * (spin[j] ^ base)); //rotated due to symmetry
                  reasons
500             fieldpart7 += (DM ^ spin[j]);
501           }
502         }
503
504         sum7 *= prefx7;
505         fieldpart7 *= prefx7;
506
507         REAL8m temp7 = 0;
508         ThreeVector fieldtemp7(0.,0.,0.);
509         if(y>6) {
510           UINT4m j = i-xdim-6;
511           if(Ms_inverse[j]!=0) {
512             temp7 = (DM * (base ^ spin[j]));
513             fieldtemp7 = (spin[j] ^ DM);
514           }
515         }
516         if(y<ydim-7) {
517           UINT4m j = i+xdim+6;
518           if(Ms_inverse[j]!=0) {
519             temp7 += (DM * (spin[j] ^ base));
520             fieldtemp7 += (DM ^ spin[j]);
521           }
522         }
523
524         sum7 += temp7 * prefy7;
525         fieldpart7 += fieldtemp7 * prefy7;
526
527         temp7 = 0;
528         fieldtemp7.Set(0.,0.,0.);
529         if(z>6) {
530           UINT4m j = i-xydim-6;
531           if(Ms_inverse[j]!=0) {
```

```
532             temp7 = (DM * (base ^ spin[j]));
533             fieldtemp7 = (spin[j] ^ DM);
534           }
535         }
536         if(z<zdim-7) {
537           UINT4m j = i+xydim+6;
538           if(Ms_inverse[j]!=0) {
539             temp7 += (DM * (spin[j] ^ base));
540             fieldtemp7 += (DM ^ spin[j]);
541           }
542         }
543
544         sum7 += temp7 * prefz7;
545         fieldpart7 += fieldtemp7 * prefz7;
546
547
548         REAL8m sum8 = 0; //energy part
549         ThreeVector fieldpart8(0.,0.,0.); //field part
550         if(x>7) {
551           UINT4m j = i-8;
552           if(Ms_inverse[j]!=0) {
553             sum8 = ( DM * (base ^ spin[j])); //varies between 0 and 2
554             fieldpart8 = (spin[j] ^ DM); //maybe fill in +1 or -1 to
                  offset to zero??
555           }
556         }
557         if(x<xdim-8) {
558           UINT4m j = i+8;
559           if(Ms_inverse[j]!=0) {
560             sum8 += (DM * (spin[j] ^ base)); //rotated due to symmetry
                  reasons
561             fieldpart8 += (DM ^ spin[j]);
562           }
563         }
564
565         sum8 *= prefx8;
566         fieldpart8 *= prefx8;
567
568         REAL8m temp8 = 0;
569         ThreeVector fieldtemp8(0.,0.,0.);
570         if(y>7) {
571           UINT4m j = i-xdim-7;
572           if(Ms_inverse[j]!=0) {
573             temp8 = (DM * (base ^ spin[j]));
574             fieldtemp8 = (spin[j] ^ DM);
575           }
576         }
577         if(y<ydim-8) {
578           UINT4m j = i+xdim+7;
```

```
579             if(Ms_inverse[j]!=0) {
580               temp8 += (DM * (spin[j] ^ base));
581               fieldtemp8 += (DM ^ spin[j]);
582             }
583           }
584
585           sum8 += temp8 * prefy8;
586           fieldpart8 += fieldtemp8 * prefy8;
587
588           temp8 = 0;
589           fieldtemp8.Set(0.,0.,0.);
590           if(z>7) {
591             UINT4m j = i-xydim-7;
592             if(Ms_inverse[j]!=0) {
593               temp8 = (DM * (base ^ spin[j]));
594               fieldtemp8 = (spin[j] ^ DM);
595             }
596           }
597           if(z<zdim-8) {
598             UINT4m j = i+xydim+7;
599             if(Ms_inverse[j]!=0) {
600               temp8 += (DM * (spin[j] ^ base));
601               fieldtemp8 += (DM ^ spin[j]);
602             }
603           }
604
605           sum8 += temp8 * prefz8;
606           fieldpart8 += fieldtemp8 * prefz8;
607
608
609           REAL8m sum9 = 0; //energy part
610           ThreeVector fieldpart9(0.,0.,0.); //field part
611           if(x>8) {
612             UINT4m j = i-9;
613             if(Ms_inverse[j]!=0) {
614               sum9 = ( DM * (base ^ spin[j])); //varies between 0 and 2
615               fieldpart9 = (spin[j] ^ DM); //maybe fill in +1 or -1 to
                      offset to zero??
616             }
617           }
618           if(x<xdim-9) {
619             UINT4m j = i+9;
620             if(Ms_inverse[j]!=0) {
621               sum9 += (DM * (spin[j] ^ base)); //rotated due to symmetry
                      reasons
622               fieldpart9 += (DM ^ spin[j]);
623             }
624           }
625
```

```
626         sum9 *= prefx9;
627         fieldpart9 *= prefx9;
628
629         REAL8m temp9 = 0;
630         ThreeVector fieldtemp9(0.,0.,0.);
631         if(y>8) {
632           UINT4m j = i-xdim-8;
633           if(Ms_inverse[j]!=0) {
634             temp9 = (DM * (base ^ spin[j]));
635             fieldtemp9 = (spin[j] ^ DM);
636           }
637         }
638         if(y<ydim-9) {
639           UINT4m j = i+xdim+8;
640           if(Ms_inverse[j]!=0) {
641             temp9 += (DM * (spin[j] ^ base));
642             fieldtemp9 += (DM ^ spin[j]);
643           }
644         }
645
646         sum9 += temp9 * prefy9;
647         fieldpart9 += fieldtemp9 * prefy9;
648
649         temp9 = 0;
650         fieldtemp9.Set(0.,0.,0.);
651         if(z>8) {
652           UINT4m j = i-xydim-8;
653           if(Ms_inverse[j]!=0) {
654             temp9 = (DM * (base ^ spin[j]));
655             fieldtemp9 = (spin[j] ^ DM);
656           }
657         }
658         if(z<zdim-9) {
659           UINT4m j = i+xydim+8;
660           if(Ms_inverse[j]!=0) {
661             temp9 += (DM * (spin[j] ^ base));
662             fieldtemp9 += (DM ^ spin[j]);
663           }
664         }
665
666         sum9 += temp9 * prefz9;
667         fieldpart9 += fieldtemp9 * prefz9;
668
669
670         REAL8m sum10 = 0; //energy part
671         ThreeVector fieldpart10(0.,0.,0.); //field part
672         if(x>9) {
673           UINT4m j = i-10;
674           if(Ms_inverse[j]!=0) {
```

```
675             sum10 = ( DM * (base ^ spin[j])); //varies between 0 and 2
676             fieldpart10 = (spin[j] ^ DM); //maybe fill in +1 or -1 to
                    offset to zero??
677           }
678         }
679         if(x<xdim-10) {
680           UINT4m j = i+10;
681           if(Ms_inverse[j]!=0) {
682             sum10 += (DM * (spin[j] ^ base)); //rotated due to symmetry
                    reasons
683             fieldpart10 += (DM ^ spin[j]);
684           }
685         }
686
687         sum10 *= prefx10;
688         fieldpart10 *= prefx10;
689
690         REAL8m temp10 = 0;
691         ThreeVector fieldtemp10(0.,0.,0.);
692         if(y>9) {
693           UINT4m j = i-xdim-9;
694           if(Ms_inverse[j]!=0) {
695             temp10 = (DM * (base ^ spin[j]));
696             fieldtemp10 = (spin[j] ^ DM);
697           }
698         }
699         if(y<ydim-10) {
700           UINT4m j = i+xdim+9;
701           if(Ms_inverse[j]!=0) {
702             temp10 += (DM * (spin[j] ^ base));
703             fieldtemp10 += (DM ^ spin[j]);
704           }
705         }
706
707         sum10 += temp10 * prefy10;
708         fieldpart10 += fieldtemp10 * prefy10;
709
710         temp10 = 0;
711         fieldtemp10.Set(0.,0.,0.);
712         if(z>9) {
713           UINT4m j = i-xydim-9;
714           if(Ms_inverse[j]!=0) {
715             temp10 = (DM * (base ^ spin[j]));
716             fieldtemp10 = (spin[j] ^ DM);
717           }
718         }
719         if(z<zdim-10) {
720           UINT4m j = i+xydim+9;
721           if(Ms_inverse[j]!=0) {
```

```
722             temp10 += (DM * (spin[j] ^ base));
723             fieldtemp10 += (DM ^ spin[j]);
724           }
725         }
726
727         sum10 += temp10 * prefz10;
728         fieldpart10 += fieldtemp10 * prefz10;
729
730
731         ThreeVector fieldpart(0.,0.,0.);
732         REAL8m sum = 0;
733
734         sum = (sum1 + sum2 + sum3 + sum4 + sum5 + sum6 + sum7 + sum8 +
                sum9 + sum10);
735         fieldpart = (fieldpart1 + fieldpart2 + fieldpart3 + fieldpart4 +
                fieldpart5 + fieldpart6 + fieldpart7 + fieldpart8 +
                fieldpart9 + fieldpart10);
736
737         field[i] = hcoef*Msii*fieldpart;
738         energy[i] = sum;
739       }
740     }
741   }
742 }
743
744 void MM_DzyaMoExchange::GetEnergy
745 (const Oxs_SimState& state,
746  Oxs_EnergyData& oed
747  ) const
748 {
749   const Oxs_MeshValue<ThreeVector>& spin = state.spin;
750   const Oxs_MeshValue<REAL8m>& Ms_inverse = *(state.Ms_inverse);
751
752   // Use supplied buffer space, and reflect that use in oed.
753   oed.energy = oed.energy_buffer;
754   oed.field = oed.field_buffer;
755   Oxs_MeshValue<REAL8m>& energy = *oed.energy_buffer;
756   Oxs_MeshValue<ThreeVector>& field = *oed.field_buffer;
757
758   const Oxs_RectangularMesh* mesh
759     = dynamic_cast<const Oxs_RectangularMesh*>(state.mesh);
760   if(mesh==NULL) {
761     throw Oxs_Ext::Error(this,"Import mesh to"
762                          " Oxs_UniformExchange::GetEnergy()"
763                          " is not an Oxs_RectangularMesh object.");
764   }
765
766   // Note: Might want to consider subclassing exchange energies,
767   //  to replace this if-block with virtual function pointers.
```

```
768   if(kernel == NGBR_6) {
769     CalcEnergyDzyaMo(spin,Ms_inverse,mesh,energy,field);
770   } else {
771     throw Oxs_Ext::Error(this,"Invalid kernel type detected."
772                          "  (Programming error)");
773   }
774
775 }
```

B. Ground state energies for different chain lengths

length	E_{tot}/atom	E_{exch}/atom	E_{DM}/atom	E_{ani}/atom	E_{B}/atom
6	−3.280	+3.054	−7.162	+0.828	+0.000
7	−3.597	+3.322	−7.794	+0.875	+0.000
8	−3.920	+3.467	−6.820	+0.766	+0.000
9	−4.185	+3.445	−8.477	+0.846	+0.000
10	−4.352	+3.495	−8.747	+0.900	+0.000
11	−4.543	+3.550	−8.986	+0.893	+0.000
12	−4.694	+3.531	−9.093	+0.868	+0.000
13	−4.774	+3.570	−9.256	+0.912	+0.000
14	−4.890	+3.614	−9.412	+0.907	+0.000
15	−4.993	+3.596	−9.470	+0.881	+0.000
16	−5.044	+3.569	−9.523	+0.909	+0.000
17	−5.118	+3.636	−9.663	+0.910	+0.000
18	−5.193	+3.637	−9.721	+0.891	+0.000
19	−5.231	+3.609	−9.746	+0.906	+0.000
20	−5.277	+3.657	−9.846	+0.912	+0.000
21	−5.335	+3.668	−9.901	+0.899	+0.000
22	−5.365	+3.640	−9.910	+0.905	+0.000
23	−5.395	+3.677	−9.986	+0.914	+0.000
24	−5.440	+3.690	−10.036	+0.905	+0.000
25	−5.467	+3.664	−10.036	+0.905	+0.000
26	−5.486	+3.693	−10.096	+0.917	+0.000
27	−5.522	+3.708	−10.140	+0.910	+0.000
28	−5.547	+3.683	−10.136	+0.907	+0.000
29	−5.558	+3.707	−10.185	+0.920	+0.000
30	−5.587	+3.722	−10.224	+0.915	+0.000
31	−5.610	+3.699	−10.218	+0.908	+0.000
32	−5.616	+3.718	−10.257	+0.922	+0.000
33	−5.641	+3.733	−10.292	+0.919	+0.000
34	−5.662	+3.713	−10.285	+0.910	+0.000

length	E_{tot}/atom	E_{exch}/atom	E_{DM}/atom	E_{ani}/atom	E_{B}/atom
35	−5.664	+3.727	−10.316	+0.925	+0.000
36	−5.685	+3.741	−10.348	+0.922	+0.000
37	−5.705	+3.725	−10.342	+0.912	+0.000
38	−5.710	+3.703	−10.332	+0.919	+0.000
39	−5.723	+3.739	−10.385	+0.923	+0.000
40	−5.741	+3.735	−10.390	+0.914	+0.000
41	−5.747	+3.713	−10.378	+0.918	+0.000
42	−5.755	+3.740	−10.419	+0.923	+0.000
43	−5.772	+3.743	−10.432	+0.916	+0.000
44	−5.779	+3.722	−10.419	+0.918	+0.000
45	−5.784	+3.745	−10.453	+0.924	+0.000
46	−5.799	+3.751	−10.468	+0.918	+0.000
47	−5.806	+3.731	−10.455	+0.918	+0.000
48	−5.809	+3.750	−10.483	+0.925	+0.000
49	−5.822	+3.758	−10.500	+0.924	+0.000
50	−5.830	+3.738	−10.487	+0.918	+0.000
100	−6.011	+3.779	−10.715	+0.926	+0.000
DFT	−6.130	+3.788	−10.918	+1.000	+0.000

Table B.1: Ground state energies extracted from OOMMF simulations for bi-atomic Fe chains of different lengths at $T = 0\,\mathrm{K}$ without an external magnetic field. The chain length is given in atoms (first column). The second column displays the total energy per Fe atom and the contributions due to Heisenberg exchange, DM interaction, MAE and magnetic field are shown in the third to sixth column. All energies are given in meV. The last row lists the energy values from the DFT calculations, i.e., an infinite chain. For longer chains, the values of the energy contributions from the OOMMF simulations approach the DFT values.

length	E_{tot}/atom	E_{exch}/atom	E_{DM}/atom	E_{ani}/atom	E_{B}/atom
6	−3.295	+3.045	−7.149	+0.825	−0.016
7	−3.620	+3.320	−7.791	+0.875	−0.023
8	−3.920	+3.467	−8.254	+0.867	−0.000
9	−4.197	+3.441	−8.469	+0.843	−0.012
10	−4.369	+3.494	−8.744	+0.898	−0.017
11	−4.543	+3.550	−8.986	+0.893	−0.000
12	−4.704	+3.528	−9.086	+0.864	−0.010
13	−4.786	+3.571	−9.254	+0.910	−0.013
14	−4.891	+3.611	−9.406	+0.905	−0.001
15	−5.003	+3.593	−9.464	+0.878	−0.009
16	−5.048	+3.614	−9.569	+0.918	−0.011
17	−5.118	+3.639	−9.664	+0.908	−0.001
18	−5.201	+3.635	−9.716	+0.888	−0.009
19	−5.232	+3.612	−9.748	+0.907	−0.002
20	−5.278	+3.660	−9.848	+0.911	−0.001
21	−5.342	+3.666	−9.896	+0.896	−0.008
22	−5.366	+3.641	−9.911	+0.906	−0.002
23	−5.396	+3.679	−9.987	+0.913	−0.001
24	−5.447	+3.689	−10.032	+0.903	−0.007
25	−5.468	+3.664	−10.037	+0.906	−0.001
26	−5.487	+3.695	−10.097	+0.916	−0.001
27	−5.529	+3.707	−10.137	+0.909	−0.007
28	−5.547	+3.683	−10.137	+0.907	−0.001
29	−5.558	+3.708	−10.185	+0.919	−0.001
30	−5.594	+3.721	−10.222	+0.913	−0.006
31	−5.611	+3.700	−10.218	+0.908	−0.001
32	−5.613	+3.676	−10.212	+0.923	−0.000
33	−5.646	+3.732	−10.290	+0.917	−0.006
34	−5.662	+3.713	−10.285	+0.910	−0.001
35	−5.667	+3.688	−10.274	+0.920	−0.001
36	−5.690	+3.741	−10.347	+0.921	−0.005
37	−5.705	+3.725	−10.342	+0.912	−0.001
38	−5.711	+3.700	−10.327	+0.918	−0.002
39	−5.727	+3.748	−10.394	+0.924	−0.005
40	−5.742	+3.735	−10.390	+0.914	−0.001
41	−5.749	+3.710	−10.374	+0.917	−0.002
42	−5.759	+3.742	−10.421	+0.924	−0.004
43	−5.772	+3.744	−10.432	+0.916	−0.000
44	−5.781	+3.720	−10.415	+0.917	−0.002

length	E_{tot}/atom	E_{exch}/atom	E_{DM}/atom	E_{ani}/atom	E_{B}/atom
45	−5.787	+3.703	−10.452	+0.924	−0.004
46	−5.799	+3.751	−10.468	+0.918	−0.000
47	−5.808	+3.728	−10.451	+0.917	−0.002
48	−5.812	+3.749	−10.483	+0.925	−0.003
49	−5.822	+3.758	−10.500	+0.920	−0.000
50	−5.833	+3.736	−10.484	+0.917	−0.002
100	−6.012	+3.778	−10.713	+0.925	−0.002

Table B.2: Magnetic energies extracted from OOMMF simulations for bi-atomic Fe chains of different lengths at $T = 0\,\mathrm{K}$ with an external magnetic field of $B = +2\,\mathrm{T}$ along the z-axis. The columns are similar to Table B.1.

Acknowledgements

Zum Schluss meiner Arbeit möchte ich mich bei all denen bedanken, die mich während der letzten Jahre unterstützt haben.

- Prof. Dr. Roland Wiesendanger danke ich für die Möglichkeit, meine Doktorarbeit in seiner Arbeitsgruppe anzufertigen und die Ergebnisse auf internationalen Konferenzen zu präsentieren. Erst durch die exzellenten Rahmenbedingungen war es möglich, die in dieser Arbeit vorgestellten Messungen durchzuführen.

- Ich danke Prof. Dr. Stefan Heinze für die Übernahme des Gutachtens der Dissertation und Prof. Dr. Kornelius Nielsch für die Übernahme des Gutachtens der Disputation.

- Dr. Kirsten von Bergmann und Dr. André Kubetzka danke ich für die exzellente Betreuung, viele hilfreiche und erhellende Diskussionen, das Korrekturlesen dieser Arbeit, sowie für viele, sehr schöne Abende außerhalb universitärer Einrichtungen.

- Dr. Yuriy Mokrousov und Prof. Dr. Stefan Heinze danke ich für die wunderbare Zusammenarbeit, die Beantwortung vieler physikalischer Fragen und die interessanten Zusammenkünfte nach getaner Arbeit.

- Ich möchte allen Mitarbeitern in Labor 013 für die herzliche Arbeitsatmosphäre danken.

- Dr. Robert Wieser danke ich für die Monte-Carlo Simulationen und hilfreiche Diskussionen theoretischer Fragen.

- Ich danke allen Mitarbeitern der Gruppe R für die schöne Zeit.

- Ich danke Wolfgang Hatje, Katrin Groth, Dieter Klatt und Jörg Völkel für die Versorgung mit flüssigem Helium, ohne die ich diese Messungen nicht hätte durchführen können.

- Zu guter Letzt möchte ich mich ganz herzlich bei meinen Freunden, meiner Familie und im Speziellen bei Nils Schaper bedanken, die mit ihrer Unterstützung zum Gelingen dieser Arbeit beigetragen haben.